Alma Mater Studiorum - Università di Bologna

DOTTORATO DI RICERCA IN

SCIENZE DELLA TERRA, DELLA VITA E DELL'AMBIENTE

Ciclo 35

**Settore Concorsuale:** 04/A3 - GEOLOGIA APPLICATA, GEOGRAFIA FISICA E GEOMORFOLOGIA

**Settore Scientifico Disciplinare:** GEO/05 - GEOLOGIA APPLICATA

# MULTI-SCALE ANALYSIS OF ACTIVE LANDSLIDES USING TWO-PASS DIFFERENTIAL INTERFEROMETRY

**Presentata da:** Pierpaolo Ciuffi

**Coordinatore Dottorato**

Maria Giovanna Belcastro

**Supervisore**

Alessandro Simoni

**Co-supervisore**

Alessandro Gargini

**Esame finale anno 2023**

# ABSTRACT

Landslides are common features of the landscape of the north-central Apennine mountain range and cause frequent damage to human facilities and infrastructure. Most of these landslides move periodically with moderate velocities and, only after particular rainfall events, some accelerate abruptly. Synthetic aperture radar interferometry (InSAR) provides a particularly convenient method for studying deforming slopes. We use standard two-pass interferometry, taking advantage of the short revisit time of the Sentinel-1 satellites.

In this paper we present the results of the InSAR analysis developed on several study areas in central and Northern Italian Apennines.

The aims of the work described within the articles contained in this paper, concern: i) the potential of the standard two-pass interferometric technique for the recognition of active landslides; ii) the exploration of the potential related to the displacement time series resulting from a two-pass multiple time-scale InSAR analysis; iii) the evaluation of the possibility of making comparisons with climate forcing for cognitive and risk assessment purposes.

Our analysis successfully identified more than 400 InSAR deformation signals (IDS) in the different study areas corresponding to active slope movements. The comparison between IDSs and thematic maps allowed us to identify the main characteristics of the slopes most prone to landslides.

The analysis of displacement time series derived from monthly interferometric stacks or single 6-day interferograms allowed the establishment of landslide activity thresholds.

This information, combined with the displacement time series, allowed the relationship between ground deformation and climate forcing to be successfully investigated.

The InSAR data also gave access to the possibility of validating geographical warning systems and comparing the activity state of landslides with triggering probability thresholds.

# Contents


**1. Introduction** ..... **1**
1.1. Motivation and focus of the current study ..... 1
1.2. General guide through the thesis ..... 2
1.3. References ..... 4
**2. Methodological notes** ..... **5**
2.1. State of the art ..... 5
2.2. Using GMTSAR for InSAR processing ..... 5
2.3. Workflow: 2-pass InSAR processing and practical examples ..... 6
2.4. Identification and mapping of InSAR deformation signals (IDS) ..... 13
2.5. Application and extraction of displacement time series derived from InSAR analysis ..... 14
2.6. Definition of IDS activity thresholds on an InSAR basis ..... 17
2.7. References ..... 20
**3. Paper 1: *Deformation Detection in Cyclic Landslides Prior to Their Reactivation Using Two-Pass Satellite Interferometry*** ..... **23**
**4. Paper 2: *Regional-scale InSAR investigation and landslide early warning thresholds in Umbria, Italy*** ..... **42**
**5. Paper 3: *Landslide deformation signals detected by InSAR at multiple temporal scales in a large basin of the Apennines*** ..... **73**
**6. Discussion and General conclusions** ..... **109**
6.1. References ..... 113

# 1. Introduction

## *1.1. Motivation and focus of the current study*

In the current document, I present the main findings of my dissertation at the University of Bologna. The work focuses on the analysis of landslides in the central and Northern Italian Apennines, although, especially during my period abroad (at the WSL Institute for Snow and Avalanche Research SLF in Davos - Switzerland), I also analysed an area of the Swiss Alps. For demonstration purposes, case studies analysed in Switzerland are included in this paper. The technique mainly used belongs to the remote sensing group and is called synthetic aperture radar interferometry (hereafter InSAR). InSAR is a well-known interferometry technique that offers the possibility of measuring small displacements on the ground surface and has been widely used to retrieve spatial and temporal deformations of slopes (e.g., Colesanti et al., 2003; Handwerger et al., 2015; Bayer et al., 2018, Dini et al. 2019, Squarzoni et al., 2020). In particular, we tested and used traditional two-pass InSAR. In addition to the recognition and mapping of deformation signals, it was used to derive spatial and temporal measurements of the gravitational slope movements. All SAR data used for the work presented within this paper were acquired by the Sentinel-1 satellites pair of the European Space Agency (ESA), and their main characteristics will be described below.

My research project consists of three main works. The study areas are located within the Italian territory, in the regions of Emilia-Romagna and Umbria.

Two different study areas were analysed within the Emilia-Romagna region and represent the works described in Chapter 3 and Chapter 5. They are located in the Northern Apennines where, due to the large areal extend of mechanically weak rocks, like tectonic and sedimentary melanges (Pini, 1999) and deposits of turbitdity currents (Ricci Lucchi, 1986), earthflows (Simoni et al, 2013) and complex landslides (Bertolini et al., 2004; Bertolini et al., 2005; Borgatti et al., 2006) are prominent features of the landscape.

As for the second study area, represented by the Umbria Region in central Italy, the morphology ranges from mountains to hills and alluvial plains. The geology is dominated by the presence of sedimentary rocks with post-orogenic marine and continental facies, flysch deposits consisting of clayey-schist and clayey-marly sediments, well-settled limestone and subordinate volcanic rocks (Cardinali et al., 2002). Landslides are widespread and recurrent and landslide deposits cover about 9% of the area. According to the national IFFI inventory (Trigila et al., 2010), more than 70% of the mapped landslides are quiescent, while the remaining ones are active, mainly based on geomorphological criteria.

All study areas are embraced by the Mediterranean climate, which is characterized by two wet seasons, one in spring and one in autumn, separated by dry summers and winters. For this reason, several landslides in the study area can suffer both seasonal acceleration and catastrophic reactivation related to rainfall events during the rainy seasons (Berti et al., 2012). Because all study areas also have a moderate density of population, infrastructure, towns and small villages, landslides often interfere with human actions.

InSAR represents a promising technique that helped answer several important questions that developed before and during this thesis work. They can be summarized as follows: What useful results and information can be derived from a two-pass site-specific InSAR analysis? Which ones from a regional or basin-scale analysis? Is there a more suitable geologic and geomorphologic context for landslides? Can an InSAR analysis be used to validate and/or refine an early warning system? Do landslides respond to seasonal precipitation and individual rain events? What are the main limitations of the technique and what drawbacks should be considered when interpreting InSAR-derived deformation?

The present work was inspired by the promising results reported by several authors such as Handwerger et al. (2015), Bayer et al. (2018), Dini et al., (2019) and Squarzoni et al. (2020). In particular, the fact that it was possible to recognize and map deformation signals over different geological and geomorphological contexts

and in areas with sparse stable reflectors. In addition, we used the information derived from InSAR to identify landslide-prone contexts and investigate the relationship between ground deformation and climate forcings.

All software packages used for InSAR processing are available in the public domain and are free for scientific purposes. The main programme for InSAR processing was GMTSAR (Sandwell et al., 2011) and specially developed codes were also used to further improve the results.

By using conventional InSAR, producing a large number of interferograms and through their selection, we were able to derive information on the spatial and temporal distribution of landslide displacements where multi-temporal InSAR techniques retrieve only sparse information pertaining to stable scatterers.

The results reported are the result of intensive collaboration with various co-authors. We have addressed technical issues related to uncertainties in the interferometric signal, or statistical analyses to determine the features of slopes most prone to host landslides , as well as scientific issues involving models for defining geographic warning thresholds and probability thresholds for triggering landslides within study areas.

### *1.2. General guide through the thesis*

The document has been organized into six chapters. The first chapter is the actual introduction. Since the mode of my doctoral course requires the submission of three papers to peer-reviewed journals, chapters three, four and five can be considered on the one hand as independent works; on the other hand, they should be seen in the framework of the overall motivation of this thesis.

Chapter two is devoted to some general methodological aspects of my work. It contains information that, because of the objective of the journals, could not be included in one of the papers, but which might be useful to other scientists or students who want to address some aspects related to InSAR processing.

The third chapter is focused on the study developed in a portion of a basin (60 $km^2$) in the Northern Italian Apennines, for a time interval of 4 years (January 2016 to December 2019). During the 4 years of analysis, the study area, was subject to the reactivation of four landslides caused by intense precipitation. We used an areal InSAR analysis to detect active slope movements during the period of interest and then, we used a site-specific analysis to investigate the relationship between precipitation and landslide acceleration events. A key goal of the work was to analyse the deformations that preceded the catastrophic failure of 3 landslides which underwent a reactivation at the end of November 2019. The results showed that this technique can retrieve spatially quasi-continuous deformation maps even in areas characterized by the absence of good-quality reflectors (mainly infrastructure and rocky outcrops). It also showed how, through careful analysis and selection of interferograms, it is possible to describe the evolution of landslide deformation over time and its relationship to climate forcings.

The fourth chapter discusses in detail an analysis carried out in collaboration with the Functional Center of the Civil Protection Department of the Umbria Region. This work presents the results of a regional InSAR survey carried out by using standard differential methodologies and Sentinel-1 SAR images. The study area is the Umbria region (8456 $km^2$), and our analysis covers the period between October 2019 and January 2021. Our goal is to detect and map active slope movements by analysing interferometric stacks. We also used the information in the single interferograms to monitor slope deformation over time and thus to characterize the activity state of selected landslides. We compared the location of the detected InSAR deformation signals with existing geological and geomorphological information, including the landslide inventory map. Finally, we investigated the relationship between the temporal evolution of 13 selected landslide signals with rainfall and soil moisture parameters. The Civil Protection of the Umbria Region uses these parameters to predict the occurrence of landslides (already mapped and/or newly triggered) on its territory and issue warning bulletins. To our knowledge, this exercise represents one of the first attempts to use remotely sensed data to support the calibration and validation of predictive methodologies used in landslide early warning systems.

Our results confirmed that differential InSAR can be used to derive spatially quasi-continuous deformation maps even where stable reflectors are scarce or absent. It proves useful for detecting actively moving landslides and, through careful selection of interferograms, can be used to qualitatively monitor landslide displacements. The selected landslide displacement time series has proven particularly useful for validating existing landslide warning thresholds, where historical data are typically sparse and often unreliable.

Chapter 5 discusses the results of an InSAR survey by using similar methodologies and the same type of data as the work presented within Chapter 4. The study area is represented by a large basin in the Emilia-Romagna region in the Northern Apennines. The area has an extension of 1136 $km^2$ and the analysis covers the period between April 2014 and December 2019. One of our main goals was to identify and map active slope movements by analysing interferometric stacks made on different time scales (total, annual, and monthly). In addition, we extracted information from single monthly stacks to monitor slope deformation over time and thus to characterize the state of activity of mapped landslides. We analysed the relationship between the location of the mapped deformation signals on an InSAR basis with a more complete dataset related to the geological and morphological features of the study area, but also with information on the dates of activation (or reactivation) of the studied landslides. Finally, we compared the temporal evolution of the mapped deformation signals with the landslide activation probability thresholds available in the literature for our study area. Again, the study confirmed that differential (or two-pass) InSAR can be used to retrieve spatially quasi-continuous deformation maps even when stable reflectors are scarce or absent. In addition, proved to be a powerful tool to derive time series of mapped landslide displacements, which represent an effective dataset for the purpose of making comparisons with climate forcings and, in particular, with landslide activation probability thresholds. This comparison allowed us to follow the evolution of active and inactive signals during rainy and dry months.

*1.3. References*


Bayer, B., Simoni, A., Mulas, M., Corsini, A., & Schmidt, D. (2018). Deformation responses of slow moving landslides to seasonal rainfall in the Northern Apennines, measured by InSAR. Geomorphology, 308, 293-306.

Berti, M., Martina, M. L. V., Franceschini, S., Pignone, S., Simoni, A. and Pizziolo, M. (2012): Probabilistic rainfall thresholds for landslide occurrence using a Bayesian approach. Journal of Geophysical Research-earth Surface, 117 (), F04006.

Bertolini, G., Casagli, N., Ermini, L. & Malaguti, C. (2004). Radiocarbon data on lateglacial and Holocene landslides in the Northern Apennines. - Natural Hazards, 31 (3), European Geophys Soc.

Bertolini, G., Guida, M. & Pizziolo, M. (2005). Landslides in Emilia-Romagna region (Italy); strategies for hazard assessment and risk management. Landslides, 2 (4), pp. 302-312; Heidelberg.

Borgatti, L., Corsini, A., Barbieri, M., Sartini, G., Truffelli, G., Caputo, G. & Puglisi, C. (2006). Large reactivated landslides in weak rock masses; a case study from the Northern Apennines (Italy). - Landslides, 3 (2), pp. 115-124; Berlin, New York etc.

Cardinali, M., Reichenbach, P., Guzzetti, F., Ardizzone, F., Antonini, G., Galli, M., Cacciano, M., Castellani, M., and Salvati, P. A geomorphological approach to the estimation of landslide hazards and risks in Umbria, Central Italy, Nat. Hazards Earth Syst. Sci., 2, 57–72, https://doi.org/10.5194/nhess-2-57-2002, 2002.

Colesanti, C., Ferretti, A., Prati, C., & Rocca, F. (2003). Monitoring landslides and tectonic motions with the Permanent Scatterers Technique. Engineering geology, 68(1-2), 3-14.

Dini, B., Manconi, A., Loew, S., 2019. Investigation of slope instabilities in NW Bhutan as derived from systematic DInSAR analyses. Engineering Geology 259, 105111.

Handwerger, A. L., Roering, J. J., Schmidt, D. A., & Rempel, A. W. (2015). Kinematics of earthflows in the Northern California Coast Ranges using satellite interferometry. Geomorphology, 246, 321- 333.

Pini, G. A. (1999). Tectonosomes and olistostromes in the argille scagliose of the Northern Apennines, Italy. Special Paper - Geological Society of America, 335 (1), pp. 1-70; Boulder.

Ricci Lucchi, F. (1986). The Oligocene to Recent foreland basins of the Northern Apennines. - In: A., P. & Homewood, P. [eds.] (1986): Special Publication of the International Association of Sedimentologists, pp. 105-139; Oxford (Black-well).

Sandwell, D., Mellors, R., Tong, X., Wei, M. & Wessel, P. (2011). GMTSAR: An InSAR Processing System Based on Generic Mapping Tools, url: http://www.escholarship.org/uc/item/8zq2c02m; - retrieved 05.06.2016.

Simoni, A., Ponza, A., Picotti, V., Berti, M. & Dinelli, E. (2013). Earthflow sediment production and Holocene sediment record in a large Apennine catchment. Geomorphology, 188 (1), pp. 42-53; Amsterdam.

Squarzoni, G.; Benedikt, B.; Franceschini, S.; Simoni, A. Pre- and post-failure dynamics of landslides in the Northern Apennines revealed by space-borne synthetic aperture radar interferometry (InSAR). Geomorphology 2020, 369, 107353.

Trigila, A., Iadanza, C., Spizzichino, D., 2010. Quality assessment of the Italian Landslide Inventory using GIS processing. Landslides 7, 455–470. https://doi.org/10.1007/s10346-010-0213-0.

## 2. Methodological notes

### *2.1. State of the art*

Spaceborne Synthetic Aperture Radar interferometry (InSAR) is a remote sensing technique that can be applied to detect small displacements of the Earth's surface. Early applications can be found in Gabriel et al. (1989), who measured deformation in an agricultural area, Massonet et al. (1995) applied the technique to volcanic deformation and Massonet and Feigl (1995) who used it to assess the displacement field of an earthquake to an area deformed by a small earthquake (for a review of the early examples of successful InSAR studies see Massonet and Feigl, 1998). The main advantage of satellite InSAR is the possibility to measure deformation events that occurred in the past, within the period of activity of the satellite used, over a large area. When it comes to landslide monitoring, some drawbacks exist: if the surface scattering characteristics change significantly, the interferometric phase decorrelates, leading to signal loss. In the study areas, this occurs frequently during late spring with vegetation growth or during winter in the presence of snow. The upper detection limit for displacements measuring requires that no large deformations occur between two consequent radar images and the reflection properties of the ground targets are coherent over time. Those limitations are related to the fact that interferometry measures displacements in order of $2\pi$ radians cycle (Massonet and Feigl, 1998; Rosen et al., 2000).

In last years, InSAR on landslide-prone areas have been increasingly applied (e.g. Colesanti et al., 2003; Hilley et al., 2004; Wasowski and Bovenga, 2014; Handwerger et al., 2015; Bayer et al., 2017, 2018; Dini et al., 2019; Squarzoni et al., 2020). The development of new processing algorithms (Ferretti et al., 2001; Berardino et al., 2002; Hooper et al., 2004; Hooper, 2008; Ferretti et al., 2011) enhanced the ability to obtain meaningful results even in difficult terrain.

However, obtaining valid data on fast-moving landslides remains a challenging task. The need to monitor landslide-prone areas inspired the attempt to apply conventional two-pass interferometry to several study areas within Italy.

### *2.2. Using GMTSAR for InSAR processing*

The InSAR processing scheme used throughout this dissertation is based on GMTSAR, which is documented in more detail in the manual (see also Sandwell et al. 2011) and only some general information is given in this paragraph.

GMTSAR (Generic Mapping Tools SAR) is an open-source-GNU (General Public License) SAR/InSAR processing tool capable of processing satellite data. It uses raw SAR images to derive geographical InSAR results.

The system uses accurate orbital information and a consistent geometric model of topography to achieve correct image focus and alignment. GMTSAR is a processing system designed with Generic Mapping Tools (GMT), which is an open source collection of tools designed for the manipulation and visualisation of geographic datasets (Wessel and Smith, 1998). It also includes programs for filtering and trend removal, making it suitable for some aspects of InSAR processing (Sanwell et al. 2011).

GMTSAR is an established system that is frequently applied to the analysis of satellite images and has been used for several applications. It has been successfully employed for the estimation of ground subsidence (Rezaei et al, 2019; Ulma et al, 2021; Senturk et al., 2016; Anjasmara et al., 2018), for investigating landslides (Aslan et al., 2020; Isya et al., 2019) and for studying earthquakes and other deformations (Suresh et al., 2020; Sreejith et al., 2018).

*2.3. Workflow: 2-pass InSAR processing and practical examples*

This paragraph presents the main points of interferometric processing, bringing more attention to aspects related to the practical functions of the operator, rather than information related to software and processing theories, which are available within the work proposed by Sandwell et al. (2011).

The section describes the main steps of the workflow and presents practical examples for explanatory purposes.

Figure 1 shows an overview of the 18 main InSAR processing steps, which will be described within the following text.

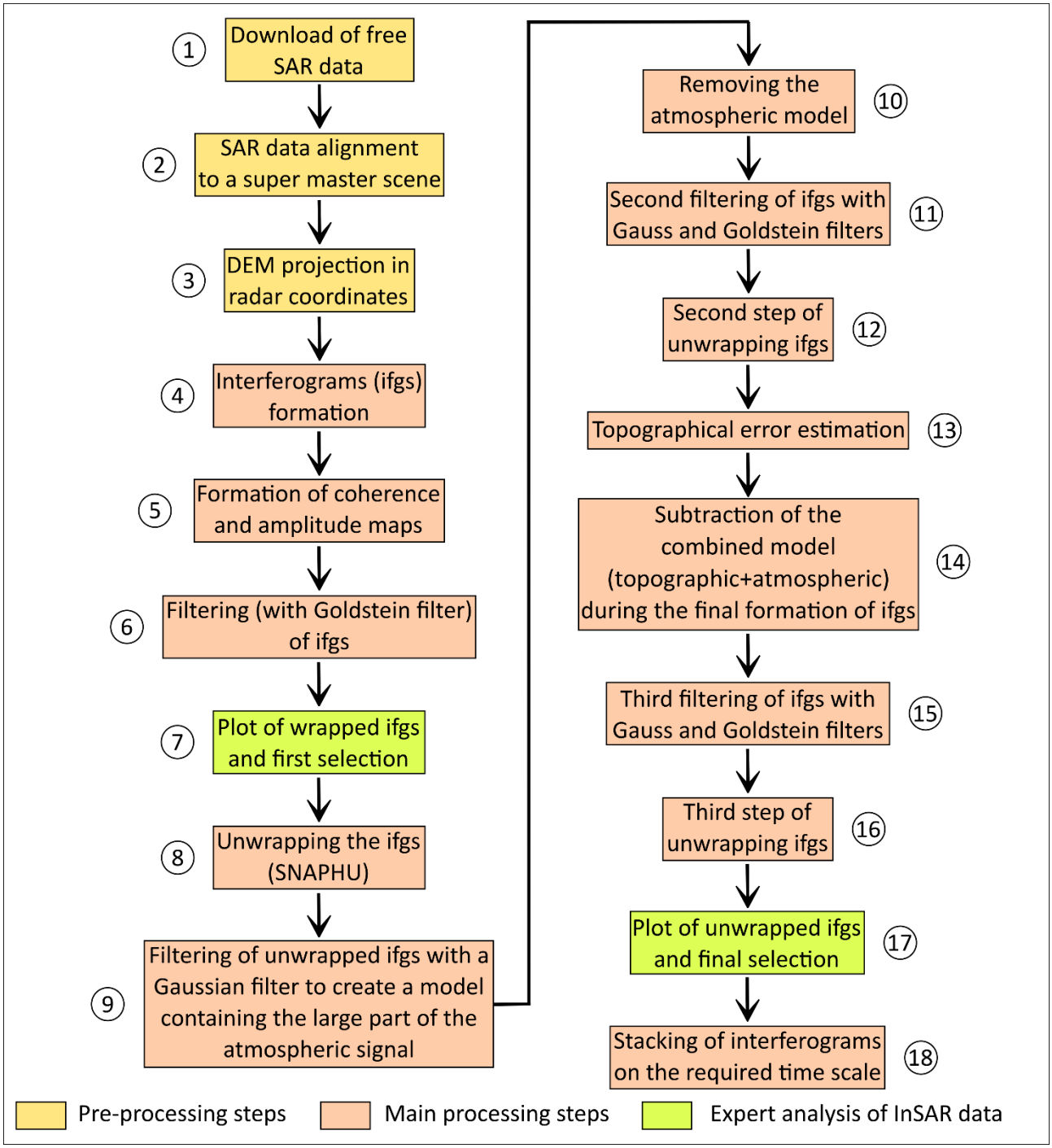


**Figure 1 -** Flow diagram of 2-pass processing beginning with raw SAR and a digital elevation grid and ending with geocoded grids of interferometric products.

Figure 2 shows the spatial distribution of the example study areas and landslides analysed, which will be shown and discussed below.

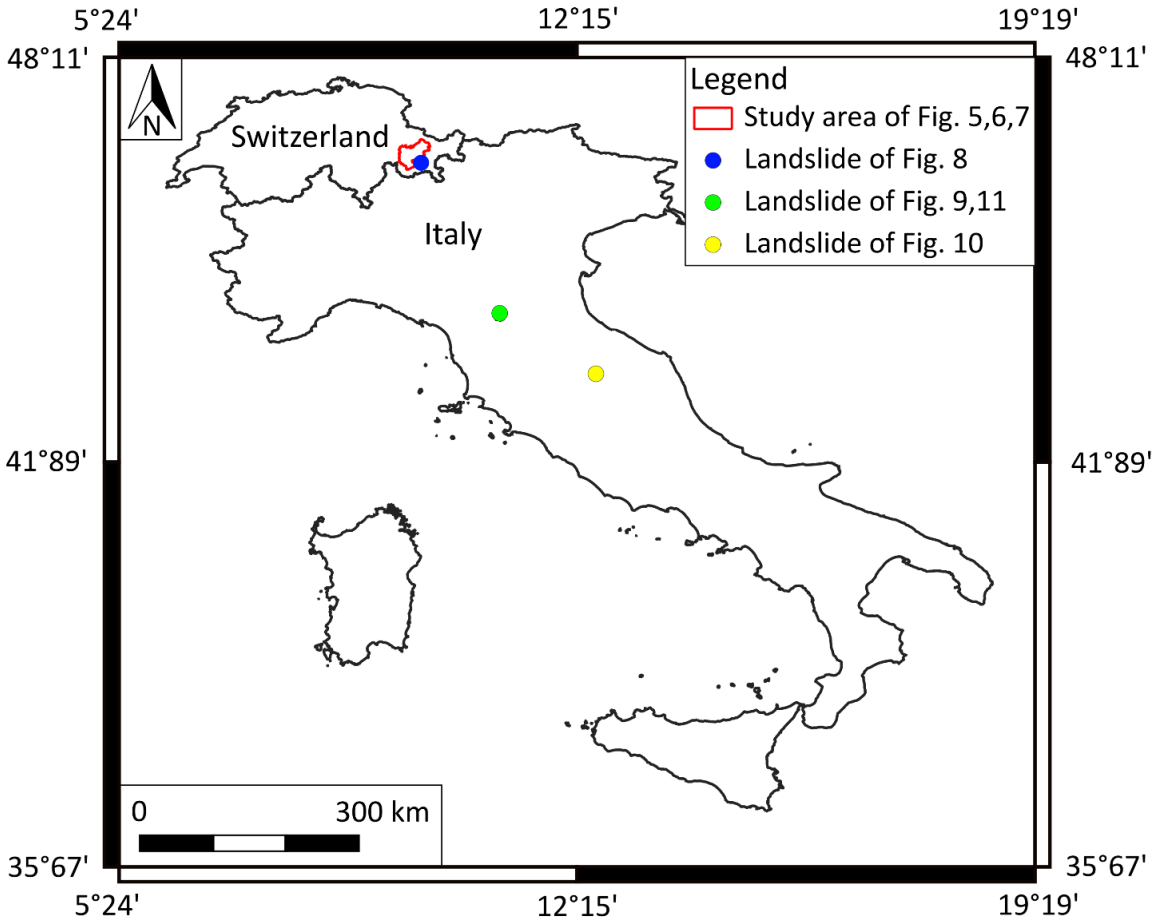


**Figure 2 -** Spatial distribution of the study areas and example landslides shown in the following figures within the chapter.

The formation and analysis of interferograms requires several steps, which will be briefly described below.

The first step is the downloading of SAR data. The SAR images used for the work described in this document are acquired by the Sentinel-1 mission. Sentinel images are C-band SAR images (5.6 cm wavelength) acquired with a minimum acquisition interval of six days (12 days for each satellite, with a six-day interval between Sentinel-1A and Sentinel-1B images).

For the present work, we use the interferometric wide swath (IW) acquisition mode and the start product class is Single Look Complex (SLC).

Figure 3a shows an artistic view of the Sentinel-1 satellite during data acquisition and some examples of InSAR applications, while figure 3b shows a schematic explanation of acquisition and processing theory: the standard 2-pass InSAR uses two SAR images of the same area acquired at different times, if the distance between the ground and the satellite changes between the two acquisitions due to surface movement, a phase shift occurs.

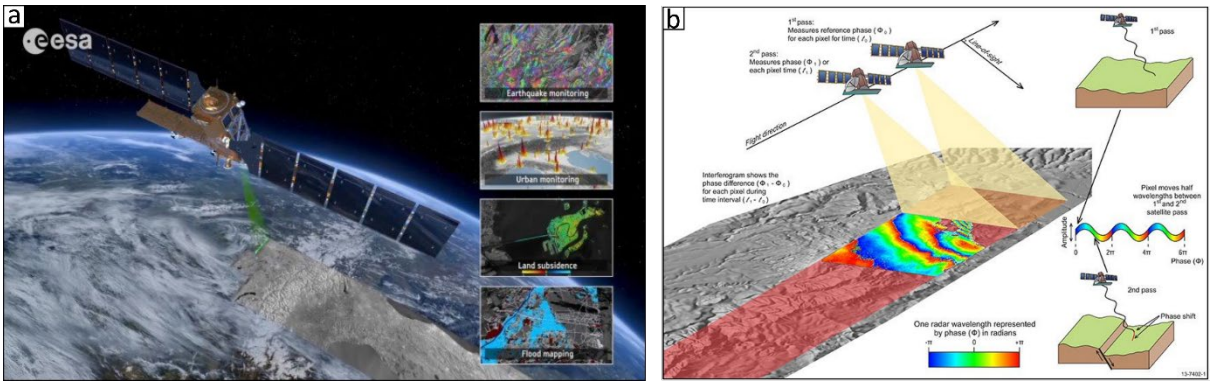


**Figure 3 -** Artistic view of the Sentinel-1 satellite and examples of land applications: Monitoring of earthquakes, urban areas, land subsidence and flooding mapping (https://www.esa.int/Applications/Observing_the_Earth/Copernicus/Sentinel-1/Changing_lands) (a), Two SAR images of the same area are acquired at different times. If the surface moves between the two acquisitions a phase shift is recorded. An interferogram maps this phase shift spatially (https://www.ga.gov.au/scientific-topics/positioning-navigation/geodesy/geodetic-techniques/interferometric-synthetic-aperture-radar) (b).

Figure 4 shows the summary information of the Sentinel-1 constellation in terms of acquired data characteristics and achievable results.

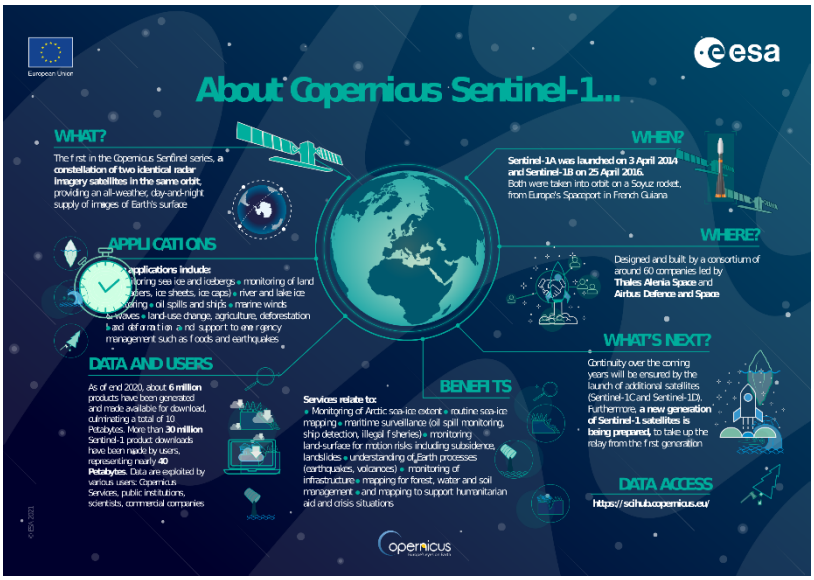


**Figure 4 -** Infographic of the Copernicus Sentinel-1 mission, it summarises the radar imaging constellation and its achievements (https://sentinels.copernicus.eu/web/sentinel/missions/sentinel-1).

Following the data download, the images for a given area, have to be aligned in a common master geometry. By our convention, we use a scene in the centre of the analysis time window and all other images were recorded on this scene.

After the alignment of the SLC images, a digital elevation model was projected into radar geometry in order to forward model and subtract the topographic phase (e.g. Massonet and Feigl, 1995).

Once the images are aligned and a digital elevation model was radar-coded, different combinations of scenes were used to form the actual interferograms (STEP 4).

Then, as illustrated in the workflow diagram in figure 1, the analysis generates the amplitude and coherence maps.

Step 6 consists of filtering the interferograms using a combination of Gaussian and Goldstein filter (Goldstein and Werner, 1997) with the aim of reducing noise, improving the result and highlighting the deformation

signal and, after this step, it is possible to plot the first results, represented by the wrapped interferograms (figure 5).

These filtered interferograms, as shown in figure 5, are characterised by a different content of the InSAR data, based on the degree of correlation. At this point, the InSAR operator intervenes to inspect visually the interferograms (step 7 in figure 1). The most critical aspect should be to eliminate interferograms that are decorrelated due to the low coherence between the SAR images used to generate them and, therefore, cannot contain useful displacement information.. It has proven practical to distinguish between good intermediate and bad interferograms. Good interferograms (figure 5a) contain clear interferometric phase with overall high coherence, although not all displacements reported within it are realistic and reliable. This classification into good, medium and bad interferograms is adopted by convention by us during InSAR processing, but does not describe the results in absolute terms. Intermediate (Med in figure 5b) quality interferograms are interferograms partly decorrelated but may contain useful information or may be improved by altering the processing parameters. Bad interferograms (figure 5c) are essentially decorrelated and should not contain useful information on large parts of the area of interest.

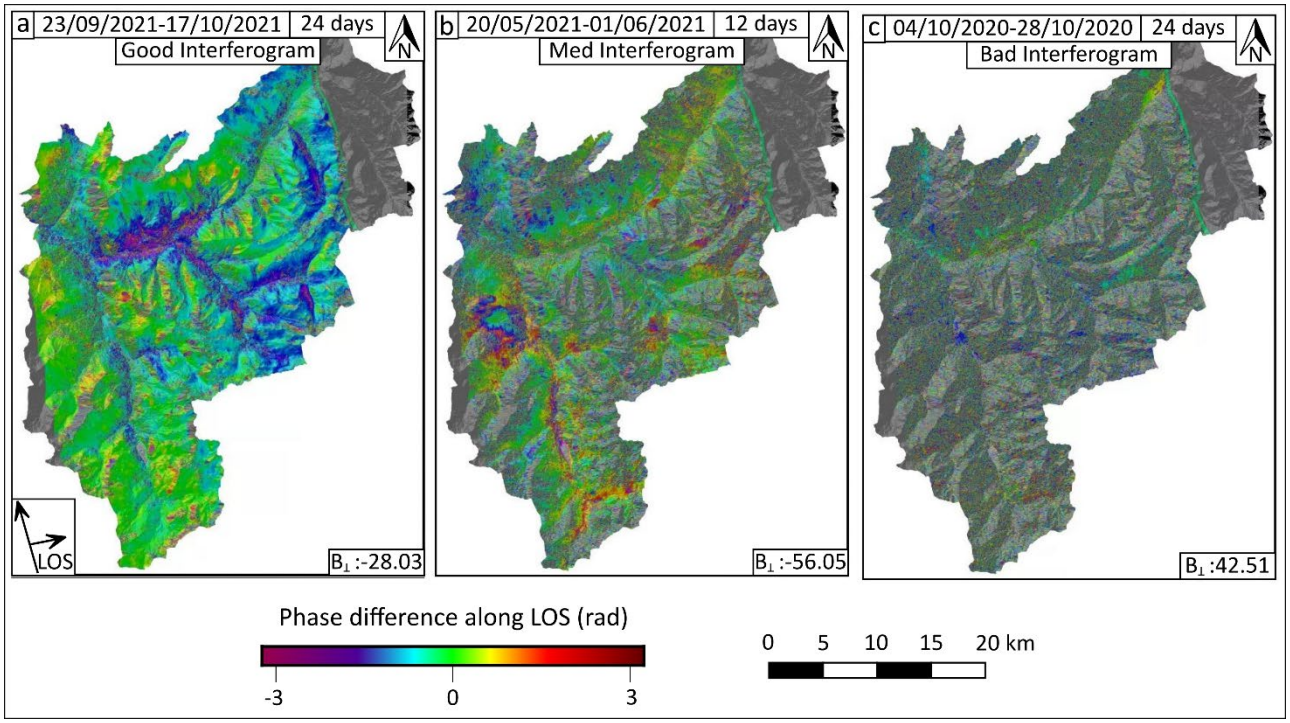


**Figure 5 -** Examples of good (a), medium (b) and bad (c) wrapped interferograms. The information at the top of the figure, from left to right, represents the date of acquisition of the SAR images that make up the interferogram (master-slave), the quality of the result and the temporal baseline; at the bottom right, the value of the spatial (or perpendicular) baseline.

At the end of the inspection and selection process of the interferograms by the operator, the list of results to be used for the next steps of the work will only consist of interferograms like the one in figure 5 a and b. Following this first selection, the filtered phase can be unwrapped (Step 8 in figure 1). GMTSAR uses the Snaphu 2D unwrapper by Chen and Zebker (2002). We use an iterative unwrapping process: the first one without any correction (step 8).

The interferometric phase still includes at this point both atmospheric disturbances as well as residual DEM errors. Assuming that the non-turbulent part of the atmospheric noise is mapped as long wavelength signals in the unwrapped interferograms (e.g. ionosphere, large cloud systems or stratified troposphere) (Bekaert et al., 2015a; Bekaert et al., 2015b), a low pass filter that includes these signals can be designed (Step 9). The filter wavelength should be chosen to be larger than the deformation signal, which is fairly easy for landslides which are small wavelength signals compared to atmosphere. During interferogram formation this large scale

atmospheric model can be passed to the GMTSAR processing chain (Step 10) which will remove it during the second round of interferogram formation. The concept is similar to the forward modelling of the topographic phase or deformation modelling (Handwerger et al., 2015).

The interferograms that were corrected by the atmospheric model are then filtered (Step 11) and unwrapped (Step 12).

The unwrapped interferograms contain still signals due to residual DEM errors and turbulent atmosphere. While the latter cannot be well-modelled, the DEM can be estimated by solving for the relationship between phase and perpendicular baseline (Fattahi and Amelung, 2015). The DEM error estimate can then be added to the atmospheric model and passed during a third and last interferograms formation (Step 14). After the third filtering (Step 15) and unwrapping (Step 16), the interferograms can be reassessed for a final selection of good and bad interferograms (Step 17 in figure 1) (figure 6). I n this way some unwrapping problems are solved (mainly due to the topographical error). If there was a phase jump before, which had to be resolved by the unwrapping process, it is possible that after these steps it is no longer present and, as a result, the stacks are of higher quality.

If we are at basin scale, it is not possible to check for unwrapping errors, but we can use site-specific analyses to study defined processes.

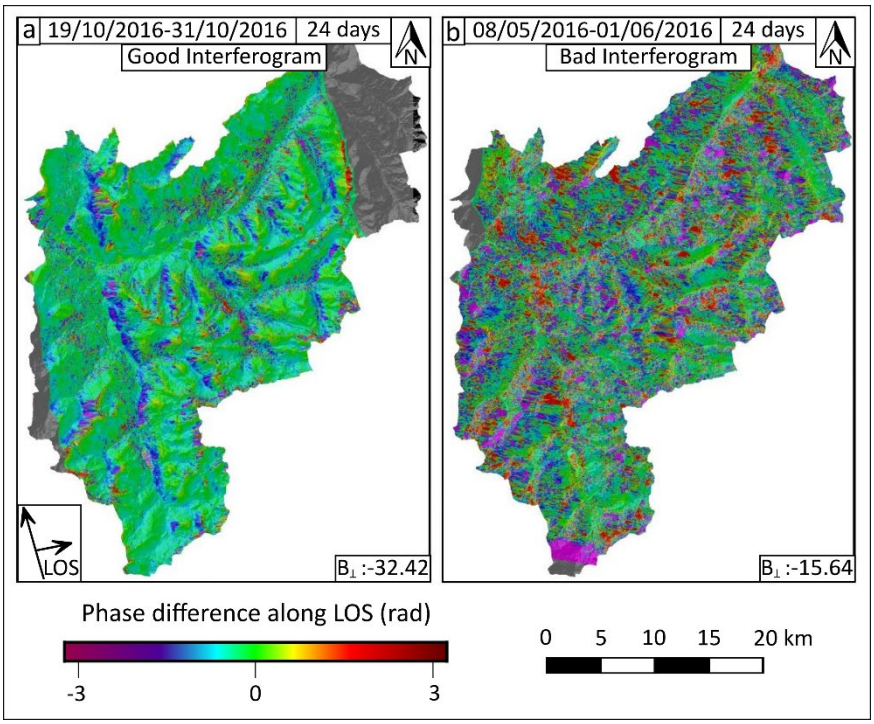


**Figure 6 -** Examples of good (a) and bad (b) unwrapped interferograms.

Again, the results are characterised by a different quality of the InSAR data, based mainly on the degree of correlation.

Even in the case of unwrapped interferograms we adopt the radian (rad) as the unit of measurement for several reasons: i) because we are looking qualitatively and preliminarily at the results and the deformation signals, ii) because switching to millimetres (or centimetres) might appear to be an accurate measurement, which is often inconsistent with what is seen in the interferometric stacks. The value described within the unwrapped interferogram could be much higher (or much lower) than that shown in the stacks for reasons discussed later and related to noise reduction during the stacking operation.

It is again necessary to inspect all the unwrapped interferograms in order to have a final list of interferograms characterised by a good data quality (example in figure 6a).

Once the final inspection is completed, interferometric stacks can be formed that statistically reduce the residual noise due to atmosphere and local decorrelation in the single interferograms, thereby increasing the signal to noise ratio (Roering et al., 2005).

For the formation of interferometer stacks, we use interferograms with different temporal baselines at 6, 12, 18 days etc. We can operate in this way because the calculation is performed by using the velocity values of the interferograms and not the displacement value (an interferogram records a displacement between two dates that can therefore be converted into velocity terms). For the creation of a monthly stack, for example, we use interferograms that last less than a month and calculate the average velocity (mm/yr) and, this value, can be converted to mm/month. If we focus on a single month, in fact, it is also possible to calculate the displacement value.

Stacks can span different time scales, which depend mainly on the goals of the work and the nature of the deformation process being investigated. For example, it is possible to create multi-year (figures 7a-d), annual (figures 7b-e), seasonal and monthly (figures 7c-f) interferometric stacks. Each of these interferometric stack types has advantages and limitations, which will be briefly discussed below.

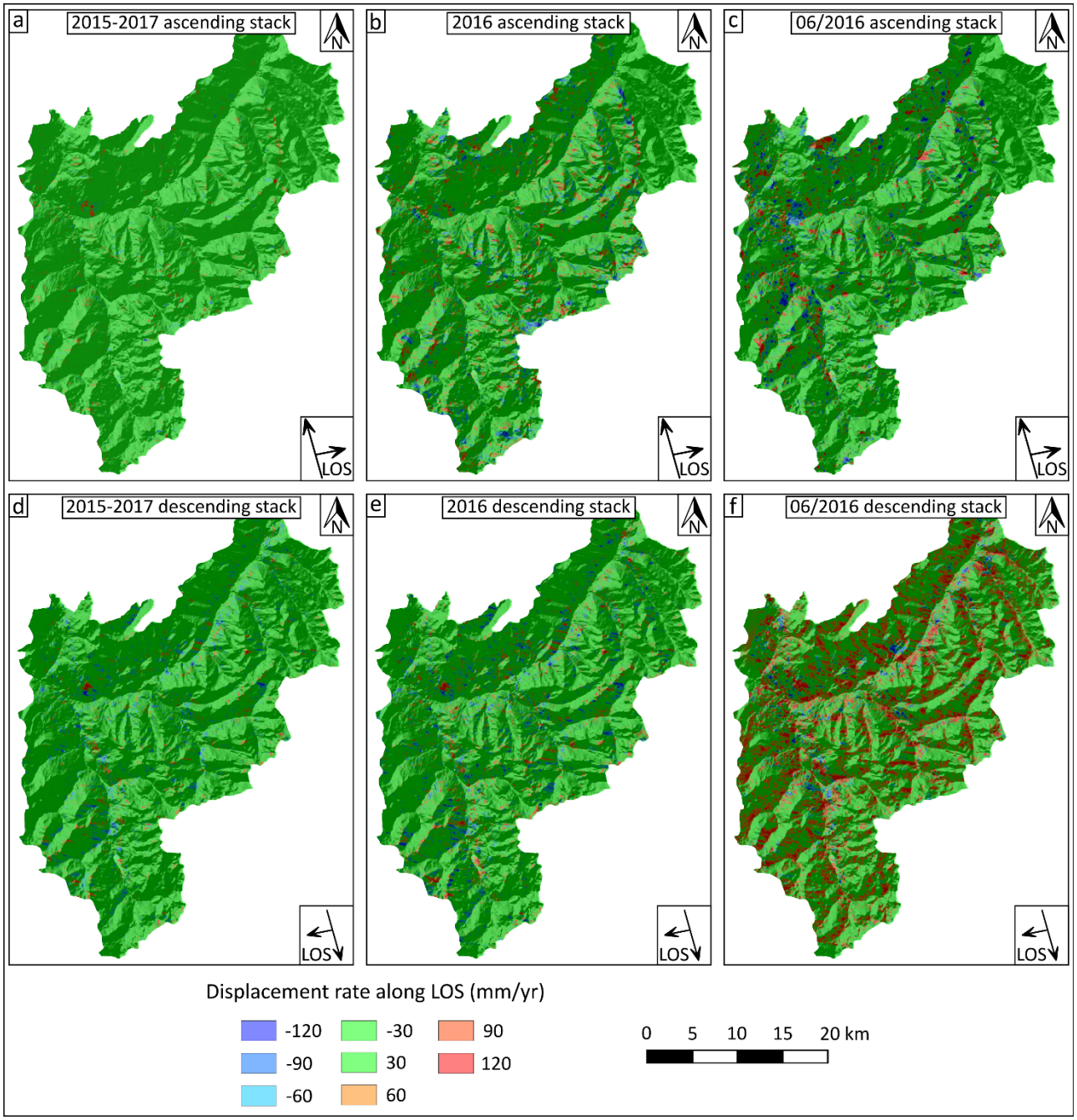


**Figure 7 -** Interferometric stacks built on different time scales and derived from ascending (a-b-c) and descending (d-e-f) acquisition orbits. Figures a and d show multi-year stacks (2015-2016-2017), figures b and e annual stacks (2016), while figures c and f show monthly stacks (June 2016).

Figure 7 shows three types of interferometric stacks. Figures 7a, b and c are obtained by processing data acquired in ascending orbit, while Figures 6d, e and f from data acquired in descending orbit. The results in figures 7a and d represent multi-year interferometric stacks, constructed for the years 2015, 2016 and 2017, figures 7b and e show annual stacks for 2017, while figures c and f represent monthly stacks for June 2016.

A preliminary deduction can be based on observation of the data. By reducing the duration of the time interval used for constructing the stack and thus decreasing the number of interferograms used for its creation, the noise is less reduced. The deformation process can be constant in time and/or space, while the noise is random. By stacking interferograms, the noise decreases, while the deformation becomes more evident (Roering et al., 2005). For this reason, the least noisy stacks are those that cover a longer time interval,

in this case several years (figures 7a-d), while the stacks with the most noise are the monthly ones (figures 7c-f).

However, it is not always possible to use interferometric stacks on a large time scale, for the detection of active landslides. We must bear in mind that if a deformation process is active during a week and then comes to a complete halt, it will not be visible within a multi-year stack because the short period of deformation accounts only for a small amount of the total data in the stack. On the other hand, a multi-year stack can be particularly useful for the recognition of very slow deformation processes. The deformation signal, due to its low displacement rate, may not be visible within single interferograms, or monthly and annual stacks, but may appear very clear within multi-year interferometric stacks.

It is necessary to be clear about the objective of the work and the processes one wishes to investigate, in order to realise the best possible interferometric data.

### *2.4. Identification and mapping of InSAR deformation signals (IDS)*

One of the main goals of the research project was to recognise and map active deformation processes by using data derived from InSAR analysis.

This section describes the methods, criteria and data used in order to map deformation processes. These processes will hereinafter be referred to as InSAR deformation signals (IDS).

We may premise that IDS recognition and mapping can also be performed using wrapped and unwrapped interferograms (figures 5 and 6), but for the works described in this document, inspection and mapping were performed by using interferometric stacks. The wrapped interferograms, for example, could reveal the presence of some deformation processes that are not clearly visible in interferometric stacks, as the filtering and unwrapping processes have not yet been applied to the data. However, the work would require more energy and time, which would not justify its use, and the validation process would also be more laborious. Whereas a deformation that is clearly visible within an interferometric stack and that is confirmed by its geological and geomorphological interpretation can be noted as an IDS with greater certainty.

As mentioned, the IDS recognition and mapping analysis was done by using the interferometric stack as input data. The work reported in Chapter 5 also describes the results of the comparison analysis between stacks with different durations, multi-year, annual and monthly, for the recognition and mapping of IDSs.

The operation is done in a GIS environment, overlaying the InSAR data with orthophotos, hillsides, slope maps and other available thematic maps, like landslide inventories or susceptibility maps. Once the anomaly is identified, it is validated to discriminate the signal associated with ground deformation from signals related to artefacts in the InSAR data, which represent errors. The validation is done either on a geomorphological basis, e.g. if a potential IDS crosses a ridge, or crosses a valley floor and/or river, it is very unlikely that it is a true deformation, but more plausible that it is an artefact (Handwerger et al., 2015). We can make a further comparison if we use more interferometric data, for example if the signal is visible in both acquisition orbits (ascending and descending), if it is visible in multiple acquisitions with the same flight geometry (if multiple ascending and descending geometries are used), if the signal is visible in stacks of different durations, if it is clearly visible in multiple annual stacks or if the IDS is active in multiple monthly stacks. The combination of all these criteria during the inspection and mapping of IDSs allows to discriminate signals related to active deformation processes from artefact-related noise in the InSAR data.

Figure 8 shows an example of a mapped IDS and how it appears using SAR data acquired in ascending orbit (Figure 8a) and descending orbit (Figure 8b).

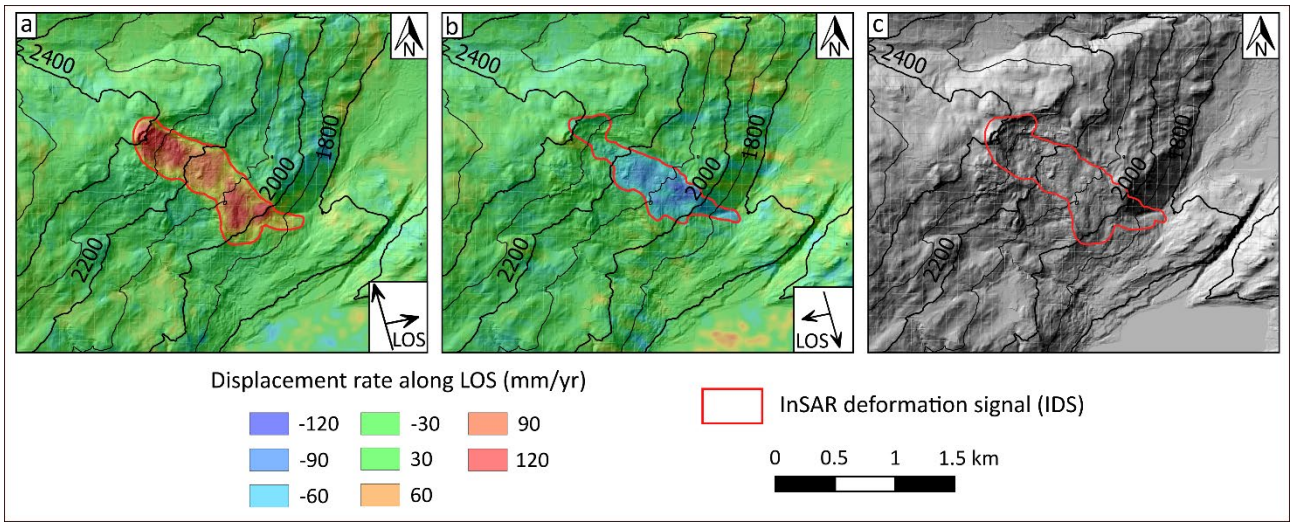


**Figure 8 -** Example of mapped InSAR deformation signal. Figure a shows multi-year stack (2015-2016-2017) derived from the processing of SAR data acquired in ascending orbit, Figure b shows the results of processing data acquired in descending orbit.

We map the IDS following its validation. In order to have boundaries as detailed as possible and not to neglect any active portion of the investigated process, the mapping is carried out on the basis of both the data acquired in an ascending orbit (figure 8a) and a descending orbit (figure 8b). The union between the two resulting polygons represents the final extension of the recognised IDS (figure 8c).

The steps just described represent the methods for recognising and mapping InSAR deformation signals for the different works presented in this paper.

### *2.5. Application and extraction of displacement time series derived from InSAR analysis*

Another goal of the work described in this paper is to investigate the possibility of using displacement time series (TS) derived from InSAR. The aim is to assess their potential and to test possible different applications. TS can be useful to better understand the behaviour of deformation processes over time and to identify the main control elements. TSs derived from InSAR can be compared with climate forcings, such as precipitation, and can be used to supplement regional warning systems, which often rely on rainfall data.

Within the following chapters (Chapters 3, 4 and 5), we tested the potential of monthly interferometric stacks and single interferograms for the extraction and study of displacement time series.

This section will briefly describe the methodology adopted for the extraction and representation of displacement time series by using the different categories of InSAR results.

The source data used come from both interferometric stacks and single interferograms. They are available in raster format (.tiff or .grd) and, for each pixel, a displacement or velocity value is recorded.

The automatic extraction operation consists of obtaining the 75$^{th}$ percentile value of the velocity in the polygon relative to the IDS studied.

In case we used the percentile method for the time series:

The velocity time series represent the 75$^{th}$ percentile of velocity values inside the polygon. This percentile value is higher than the average value which may not best describe the behaviour of the process, as large parts of the polygon may be stable. At the same time, the maximum value may be excessive and not be representative of the deformation occurring on the slope. The testing of different statistical parameters revealed that the 75th percentile is a reasonable compromise and representative of the high values within the investigated deformation process.

Figure 9 shows some examples of monthly stacks used to construct the displacement time series for the analysed landslide and the resulting series.

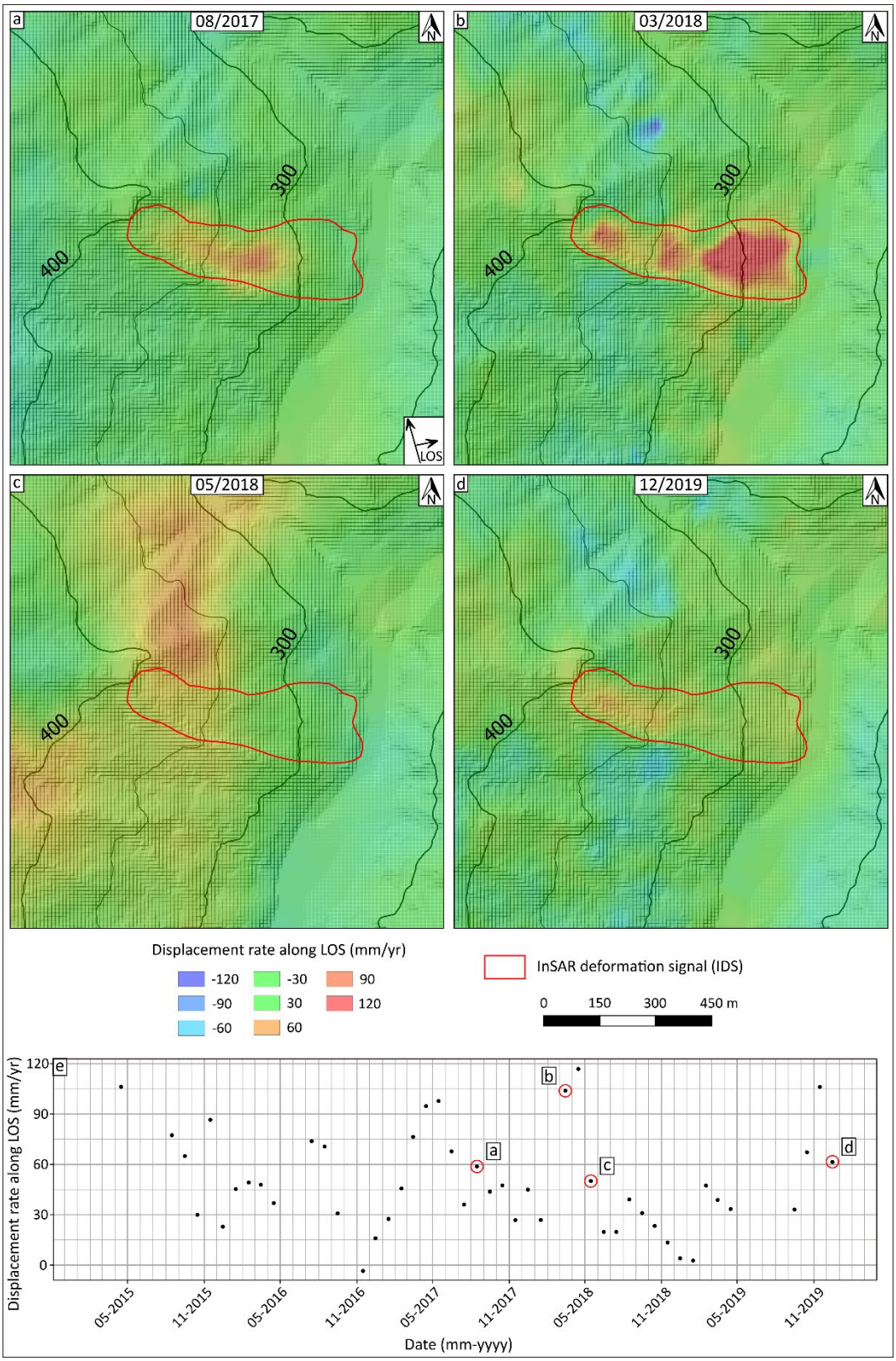


**Figure 9 -** Example of monthly interferometric stacks (a-b-c-d) used for the extraction and construction of the displacement time series (e) for the studied IDS. The red circles in Figure 8e with the label describe the displacement values along the LOS of the stacks shown.

Figure 9 shows 4 examples of monthly stacks (figures a, b, c, d) used for the extraction of velocity values for the studied IDS, characterised by different activity states. Acceleration and deceleration events are clearly visible within the resulting time series (figure 9e).

In this way, it is possible to have a monthly displacement value for the time interval investigated. The missing data correspond to the months for which, due to the low quality of the interferograms, no interferometric stack was formed. This occurred mostly in late spring and during summer when vegetation growth causes prolonged decorrelation.

In order to study the weekly evolution of the investigated deformation processes and to test the potential related to the maximum resolution of the InSAR data (6 days for the Sentinel-1 satellites), within the work described in Chapter 4, we extracted the displacement time series from the 6-day interferograms (examples in figure 10).

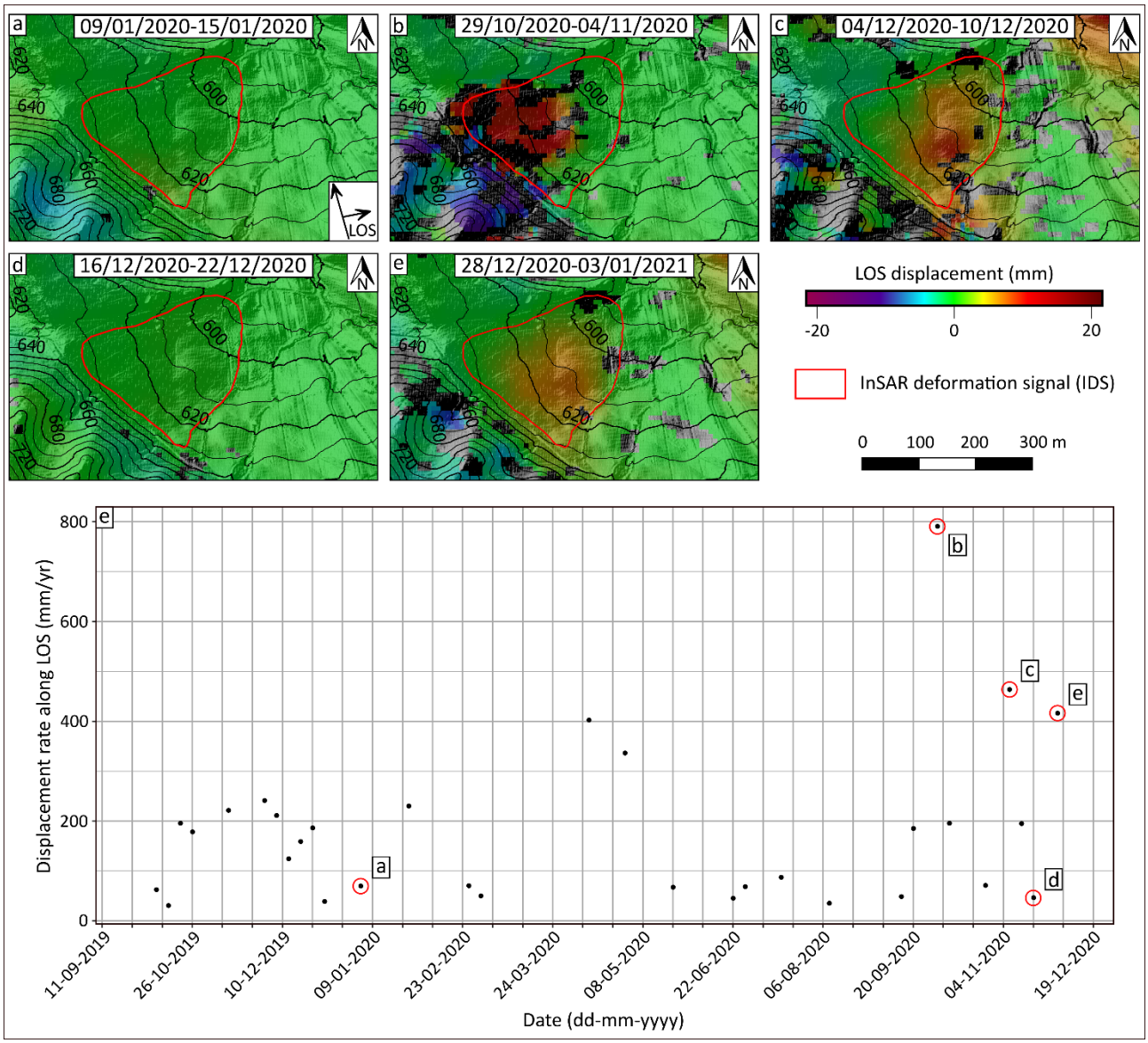


**Figure 10 -** Example of 6-day interferograms (a-b-c-d-e) used for the extraction and construction of the displacement (e) time series for the studied IDS. The red circles in Figure 9e with the label describe the displacement values along the LOS of the interferograms shown.

This can be useful when, as in our case, we wanted to compare ground deformation and parameters with a sampling frequency (or temporal resolution) that is similar and comparable to that of the InSAR data used for our analysis (6 days for Sentinel 1).

Figure 10 shows an example of 6-day interferograms (figures a, b, c, d, e) used for the construction of the displacement time series and the resulting series (figure f).

Again, the missing data are for the summer season and are related to the rapid growth of vegetation. Here again, the missing data were assigned 'no value'.

The use of 6-day interferograms allows to construct a denser displacement time series, with one data per week, for the whole study period.

### *2.6. Definition of IDS activity thresholds on an InSAR basis*

For the work described in Chapters 4 and 5, InSAR data was used to define the activity state of the IDS. This was done in order to have a binary information on the activity state of the InSAR deformation signal (IDS): active or inactive.

The identification of the activity threshold was performed by comparing the velocity (or displacement) value derived from the monthly interferometric stack (or interferogram) with the visual inspection of the corresponding stack (or interferogram).

The operation was developed by defining an activity threshold. In some cases we recognised the threshold for each IDS, while in others we set a threshold of general validity.

Figure 11 shows the same example as figure 9, on which we have defined the threshold.

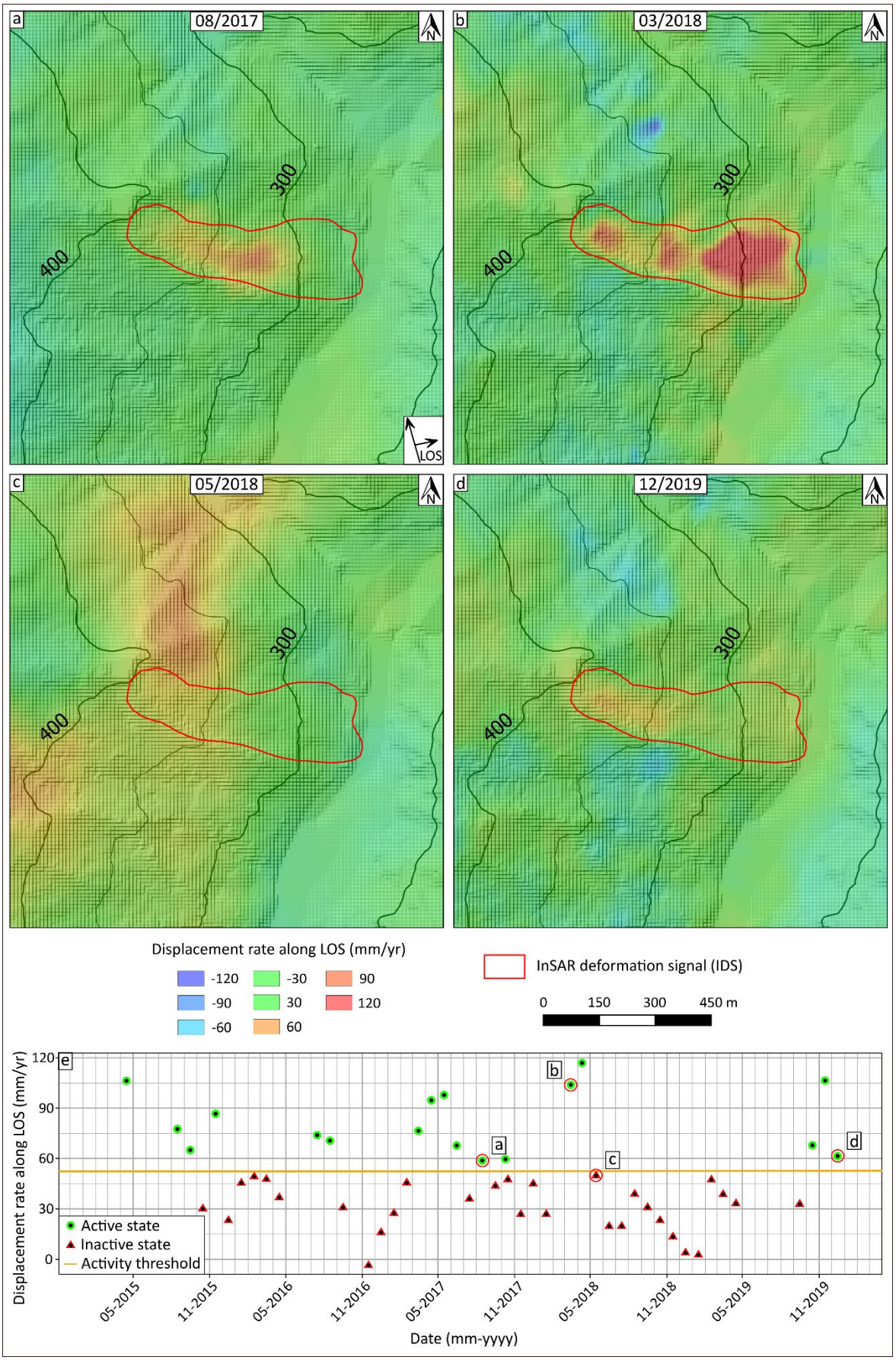


**Figure 11 -** Example of monthly interferometric stacks (a-b-c-d) used for the extraction and construction of the displacement (e) time series for the studied IDS and corresponding activity state. The red circles in Figure 8e with the label describe the displacement values along the LOS of the stacks shown.

The threshold (figure 11e), shown with the orange line, separates the active and inactive states of the studied IDS. The green dots in figure 11e describe the monthly stacks that show deformation signal and are visible in figures 11a, b and d, while the red triangles are associated with monthly stacks that do not show deformation signal, such as the one shown in figure 11c.

In the case shown as an example and described in figure 11, the activity threshold corresponds to a displacement value along the LOS of 55 mm/yr.

All monthly stacks showing a total value greater than 55 mm/yr describe active state conditions, those with a lower value, an inactive state.

*2.7 References*

Anjasmara, I. M., Yulyta, S. A., Cahyadi, M. N., Khomsin, Taufik, M., & Jaelani, L. M. Land subsidence analysis in Surabaya urban area using time series InSAR method. In AIP Conference Proceedings (Vol. 1987, No. 1, p. 020071). AIP Publishing LLC (2018).

Aslan, G. et al. Landslide mapping and monitoring using persistent scatterer interferometry (PSI) technique in the French Alps. Remote Sens. 12(8), 1305 (2020).

Bayer, B., Simoni, A., Mulas, M., Corsini, A., & Schmidt, D. (2018). Deformation responses of slow moving landslides to seasonal rainfall in the Northern Apennines, measured by InSAR. Geomorphology, 308, 293-306.

Bayer, B., Simoni, A., Schmidt, D., & Bertello, L. (2017). Using advanced InSAR techniques to monitor landslide deformations induced by tunneling in the Northern Apennines, Italy. Engineering geology, 226, 20-32.

Bekaert, D.P.S., Hooper, A., Wright, T.J., 2015a. A spatially variable power law tropospheric correction technique for InSAR data. J. Geophys. Res. Solid Earth 120 (2), 1345–1356.

Bekaert, D.P.S., Walters, R.J., Wright, T.J., Hooper, A.J., Parker, D.J., 2015b. Statistical comparison of InSAR tropospheric correction techniques. Remote Sens. Environ. 170, 40–47.

Berardino, P., Fornaro, G., Lanari, R., & Sansosti, E. (2002). A new algorithm for surface deformation monitoring based on small baseline differential SAR interferograms. IEEE Transactions on geoscience and remote sensing, 40(11), 2375-2383.

Bürgmann, R., Rosen, P.A., Fielding, E.J., 2000. Synthetic aperture radar interferometry to measure Earth's surface topography and its deformation. Annu. Rev. Earth Planet. Sci. 28, 169–209.

C. W. Chen and H. A. Zebker, ``Phase unwrapping for large SAR interferograms: Statistical segmentation and generalized network models,'' IEEE Transactions on Geoscience and Remote Sensing, vol. 40, pp. 1709-1719 (2002).

Colesanti, C., Ferretti, A., Prati, C., & Rocca, F. (2003). Monitoring landslides and tectonic motions with the Permanent Scatterers Technique. Engineering geology, 68(1-2), 3-14.

Dini, B., Manconi, A., Loew, S., 2019. Investigation of slope instabilities in NW Bhutan as derived from systematic DInSAR analyses. Engineering Geology 259, 105111.

Farr, T. G., et al. (2007), The Shuttle Radar Topography Mission, Rev. Geophys., 45, RG2004, doi:10.1029/2005RG000183.

Fattahi, H., Amelung, F., 2015. InSAR bias and uncertainty due to the systematic and stochastic tropospheric delay. Journal of Geophysical Research: Solid Earth 120, 8758–8773.

Ferretti, A., Fumagalli, A., Novali, F., Prati, C., Rocca, F., & Rucci, A. (2011). A new algorithm for processing interferometric data-stacks: SqueeSAR. IEEE Transactions on Geoscience and Remote Sensing, 49(9), 3460-3470.

Ferretti, A., Prati, C., & Rocca, F. (2001). Permanent scatterers in SAR interferometry. IEEE Transactions on geoscience and remote sensing, 39(1), 8-20.

Gabriel, A. K., Goldstein, R. M., & Zebker, H. A. (1989). Mapping small elevation changes over large areas: differential radar interferometry. Journal of Geophysical Research: Solid Earth, 94(B7), 9183-9191.

Goldstein, R. M. and C. L. Werner, (1997) "Radar ice motion interferometry," in Proc. 3rd ERS Symp., vol. 2, Florence, Italy, 1997, pp. 969–972.

Goldstein, R.M., Werner, C.L., 1998. Radar interferogram filtering for geophysical applications. Geophys. Res. Lett. 25, 4035–4038.

Handwerger, A. L., Roering, J. J., Schmidt, D. A., & Rempel, A. W. (2015). Kinematics of earthflows in the Northern California Coast Ranges using satellite interferometry. Geomorphology, 246, 321- 333.

Hilley, G. E., Bürgmann, R., Ferretti, A., Novali, F., & Rocca, F. (2004). Dynamics of slow-moving landslides from permanent scatterer analysis. Science, 304(5679), 1952-1955.

Hooper, A. (2008). A multi‐temporal InSAR method incorporating both persistent scatterer and small baseline approaches. Geophysical Research Letters, 35(16).

Hooper, A., Zebker, H., Segall, P., & Kampes, B. (2004). A new method for measuring deformation on volcanoes and other natural terrains using InSAR persistent scatterers. Geophysical research letters, 31(23).

Isya, N. H., Niemeier, W. & Gerke, M. 3D estimation of slow ground motion using InSAR and the slope aspect assumption, a case study: the puncak pass landslide, Indonesia. ISPRS Ann. Photogramm. Remote Sens. Spatial Inf. Sci. IV-2/W5, 623–630 (2019).

Massonnet, D., & Feigl, K. L. (1995). Discrimination of geophysical phenomena in satellite radar interferograms. Geophysical research letters, 22(12), 1537-1540.

Massonnet, D., & Feigl, K. L. (1998). Radar interferometry and its application to changes in the Earth's surface. Reviews of geophysics, 36(4), 441-500.

Massonnet, D., Briole, P., & Arnaud, A. (1995). Deflation of Mount Etna monitored by spaceborne radar interferometry. Nature, 375(6532), 567.

Rezaei, A. & Mousavi, Z. Characterization of land deformation, hydraulic head, and aquifer properties of the Gorgan confined aquifer, Iran, from InSAR observations. J. Hydrol. 579, 124196 (2019).

Roering, J.J., Kirchner, J.W., Dietrich, W.E., 2005. Characterizing structural and lithologic controls on deep-seated landsliding: implications for topographic relief and landscape evolution in the oregon coast range, usa. Geol. Soc. Am. Bull. 117 (5–6), 654–668.

Rosen, P. A., Hensley, S., Joughin, I. R., Li, F. K., Madsen, S. N., Rodriguez, E., & Goldstein, R. M. (2000). Synthetic aperture radar interferometry. Proceedings of the IEEE, 88(3), 333-382.

Sandwell, D. T. and E. J. Price, Phase gradient approach to stacking interferograms, J. Geophys. Res., 103, 30183-30204, 1998.

Sandwell, D., Mellors, R., Tong, X., Wei, M. & Wessel, P. (2011): GMTSAR: An InSAR Processing System Based on Generic Mapping Tools, url: http://www.escholarship.org/uc/item/8zq2c02m; - retrieved 05.06.2016.

Senturk, S., Cakir, Z. & Ustundag, B. B. The potential of Sentinel-1A interferometric SAR data in monitoring of surface subsidence caused by over drafting groundwater in agricultural areas. In 2016 Fifth International Conference on Agro-Geoinformatics (Agro-Geoinformatics) (pp. 1–4). IEEE (2016).

Squarzoni, G.; Benedikt, B.; Franceschini, S.; Simoni, A. Pre- and post-failure dynamics of landslides in the Northern Apennines revealed by space-borne synthetic aperture radar interferometry (InSAR). Geomorphology 2020, 369, 107353.

Sreejith, K. M. et al. Audit of stored strain energy and extent of future earthquake rupture in central Himalaya. Sci. Rep. 8(1), 1–9 (2018).

Suresh, D. & Yarrakula, K. InSAR based deformation mapping of earthquake using Sentinel 1A imagery. Geocarto Int. 35(5), 559–568 (2020).

Ulma, T., Anjasmara, I. M. & Hayati, N. Atmospheric phase delay correction of PS-InSAR to Monitor Land Subsidence in Surabaya. In IOP Conference Series: Earth and Environmental Science (Vol. 936, No. 1, p. 012033). IOP Publishing (2021).

Wasowski, J., & Bovenga, F. (2014). Investigating landslides and unstable slopes with satellite Multi Temporal Interferometry: Current issues and future perspectives. Engineering Geology, 174, 103- 138.

Wessel, P., and W. H. F. Smith, New, improved version of Generic Mapping Tools released, EOS Trans. Amer. Geophys. U., vol. 79 (47), pp. 579, 1998.

## 3. Paper 1

**Deformation Detection in Cyclic Landslides Prior to Their Reactivation Using Two-Pass Satellite Interferometry***

Pierpaolo Ciuffi, Benedikt Bayer, Matteo Berti, Silvia Franceschini and Alessandro Simoni

* Published in **Applied Sciences (MDPI)**

applied sciences

MDPI

*Article*

# Deformation Detection in Cyclic Landslides Prior to Their Reactivation Using Two-Pass Satellite Interferometry

**Pierpaolo Ciuffi [1], Benedikt Bayer [2], Matteo Berti [1], Silvia Franceschini [2] and Alessandro Simoni [1,*]**

[1] Department of Biological, Geological and Environmental Sciences, University of Bologna, Via Zamboni 67, 40126 Bologna, Italy; pierpaolo.ciuffi2@unibo.it (P.C.); matteo.berti@unibo.it (M.B.)
[2] Fragile s.r.l., Viale Fanin 48, 40127 Bologna, Italy; benedikt.bayer86@gmail.com (B.B.); silvia@fragilesrl.it (S.F.)
* Correspondence: alessandro.simoni@unibo.it

**Abstract:** Landslides are widespread geological features in Italy's Northern Apennines, with slow-moving earthflows among the most common types. They develop in fine-grained rocks and are subject to periodic rainfall-induced reactivations alternating to phases of dormancy. In this paper, we use radar interferometry (InSAR) and information about landslide activity to investigate deformation signals on an areal basis and to assess the dynamics of recently reactivated earthflows. We use traditional two-pass interferometry by taking advantage of the short revisit time of the Sentinel 1 satellite to characterize 4 years of slope deformations over the 60 km$^2$ study area, where 186 landslides are mapped. Our results show that most intense and sustained deformation signals are associated with phenomena on the verge of reactivation, indicating that radar interferometry may have a potential for early warning purposes. By focusing on three specific earthflow reactivations, we analyze their dynamics through the years that preceded their failure. Despite inherent uncertainties, it was possible to retrieve the deformation signal's temporal evolution, which displayed seasonally recurring accelerations, peaking during the major precipitation episodes in the area.

**Keywords:** InSAR; landslides; earthflows; reactivation; rainfall-induced landslides



**Citation:** Ciuffi, P.; Bayer, B.; Berti, M.; Franceschini, S.; Simoni, A. Deformation Detection in Cyclic Landslides Prior to Their Reactivation Using Two-Pass Satellite Interferometry. *Appl. Sci.* **2021**, *11*, 3156. https://doi.org/10.3390/app11073156

Academic Editors: Edoardo Rotigliano and Fernando Marques

Received: 30 December 2020
Accepted: 28 March 2021
Published: 1 April 2021



## 1. Introduction

Landslides represent one of the most diffuse and problematic natural hazards in many mountain chains of the world [1]. In many countries, landslides are responsible for large economic losses, damages to houses and infrastructures and fatalities [1,2]. They are common morphological features throughout the whole Northern Apennines of Italy.

Here, most slope deformations occur on old landslide bodies that already failed in the past [3] and continue to exhibit repeated partial or complete reactivations. In many cases, the reactivation of old deposits causes the regression of the main scarp and the physical degradation of the material, which moves downwards as an earthflow. In other cases, the reactivation is more complex and different types of landslides may be present on the same slope [4]. In this context, accurate landslide mapping and detection are important for a correct hazard assessment.

Conventional methods used for mapping and monitoring slope instabilities could benefit from remote sensing systems, which allow rapid and easily updatable acquisitions of data over wide areas, reducing fieldwork and costs [5–7].

A powerful technique for the displacements monitoring of large areas is the synthetic aperture radar interferometry (InSAR, DInSAR) that can measure the deformations of the landslide deposits during the slow-motion stage [8].

Radar interferometry has been successfully used to assess subsidence [9], volcanic inflation or deflation [10], and the deformation field of earthquakes [11,12]. It was also applied to detect the deformation caused by landslides [13,14] as well as subsurface excavation and tunneling [15].

The first application of radar interferometry to a landslide investigation dates back to the mid-1990s [16]. However, it was only in the following decade that this technique attracted the attention of the landslide community. Recent advances in radar satellite capabilities (e.g., high spatial resolution and high temporal frequency acquisitions), together with the development of new robust techniques based on the interferometric analysis of large datasets of radar images (multi-interferogram approach), such as the permanent scatterers (PS) [17] or the small baseline technique (SBAS) [18], have increased the potential of remote sensing for landslide investigations. One of the main limitations of multitemporal techniques is the absence of stable reflectors on most active landslides, making them difficult to apply in many critical cases. Traditional two-pass InSAR allows the detection of slow-moving landslides up to several cm per year, following the classifications of Cruden and Varnes, 1996 [19], and was successfully used to investigate the seasonal kinematics of earthflows in California [14–20]. However, before 2015 only L-band data delivered spatially quasi-continuous data in settings like the Northern Apennines. Different InSAR techniques were used in the past to retrieve spatial and temporal displacement of slow slope deformations [13,20–22]. The launch of the new Sentinel 1 satellite constellation, which is characterized by a high acquisition frequency of up to six days, is suited to reduce decorrelation in the derived interferograms [23,24] and permits obtaining promising results with higher temporal resolution [25].

This paper investigates the temporal evolution of surface displacements in a mountainous area characterized by widespread landslides using standard two-pass InSAR analysis. The study area is located in the Northern Apennines of Italy, has an extent of 60 km$^2$, and during the 4 years of analysis (from January 2016 to December 2019), was subject to the reactivation of three existing landslides caused by intense rainfall.

We used an areal InSAR analysis to detect active slope movements during the period of interest. Then we used a local analysis to investigate the relationship between rainfall and landslides acceleration events. The results show that this technique can retrieve spatially quasi-continuous deformation maps, even in areas characterized by the absence of good quality reflectors (mainly buildings and infrastructures). Moreover, through a careful interferogram analysis and selection, it is possible to characterize the evolution of landslide displacement through time and its relationship with the rainfall regime.

## 2. Study Area

The study area has an extension of 60 km$^2$ and is located in the Reno River valley South of Bologna in Italy's Northern Apennines. The Northern Apennines is a collisional belt formed from the convergence of the European and Adriatic plates between the Cretaceous and Early Miocene [26,27]. In the study area, the most common lithologies are chaotic clay-shales with block-in-matrix fabric [28,29] and deposits of turbidity currents, also known as flysch [30]. Flysch consists of a stratified alternation of sandstone, siltstone, and marlstone beds. In the following, we use the term "coarse-grained flysch" and "pelitic flysch" to indicate heterogeneous rocks where fine-grained beds are, respectively, less or more abundant than coarse-grained beds. Landslide types are related to bedrock lithology: earthflows dominate in the clay-shales [31], while a broader spectrum of landslide types can be observed in the flysch. However, the most common phenomena consist of translational or rotational earth- or rockslides in the upper part of the slopes that propagate as earthflow further down-slope [32–34].

This style of activity is typical for the whole Emilia-Romagna Region. Bertolini and Pellegrini, 2001 [4] reported more than 32,000 landslide bodies in the regional territory, most of which can be described as complex landslides, associating roto- transitional slides with earthflows. According to the authors, typical velocities are millimeters to centimeters per year during the dormant phase (which may last years to hundreds of years) and increase up to meters per hour during periodic reactivations. These rapid stages of movement typically occur after periods of heavy rainfall and can lead to the transition of the moving mass from slide to flow [35].

Within the area of interest (Figure 1), the regional inventory reports the presence of 186 landslides that were classified by the local Geological Survey as "active" or "dormant" based on geomorphic evidence. Approximately 18.8% of them are set within coarse-grained flysch, 31.2% within pelitic flysch, 38.2% within chaotic clay shales, and only 11.8% within other sedimentary rocks. Only four landslides underwent paroxysmal reactivation during the analysis period (2015–2019). All of them are located inside the chaotic clay shales. One of these landslides (the Marano earthflow) occurred in March 2020 and has already been studied using radar interferometry [8]. The other three (Braina, Carbona, and Spareda) occurred in November–December 2019 and are the subject of this study.

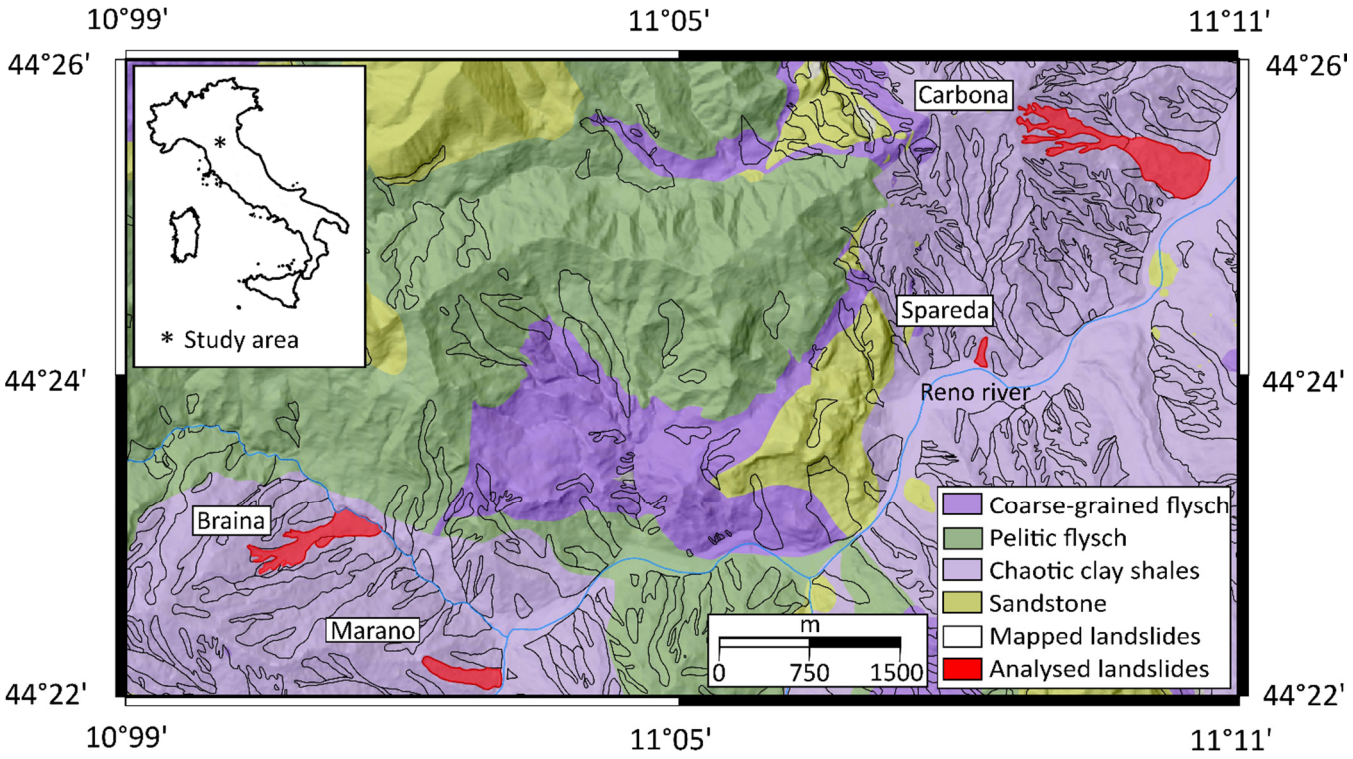


**Figure 1.** Schematic map with elements of the geology of the study area; labeled landslides are those reactivated during the study period (Geological, Seismic and Soil Service of the Emilia Romagna Region).

The area has a Mediterranean climate, with total annual precipitation of about 1300–1400 mm [36]. The temporal precipitation pattern is characterized by intense rainfall in spring and autumn, separated by dry summers and relatively dry winter months when precipitation partly occurs as snowfall [37–39].

### *2.1. The Braina Landslide*

The Braina landslide (Figure 2) is located within the municipality of Gaggio Montano, in the province of Bologna (Italy), between 375 and 596 m a.s.l. It is 1250 m long and between 100 and 400 m wide, with an average slope of 12.6 degrees. The landslide reactivated as an earthflow [19] inside chaotic clay-shales belonging to the Ligurian domain, known as Palombini Shale Formation [40].

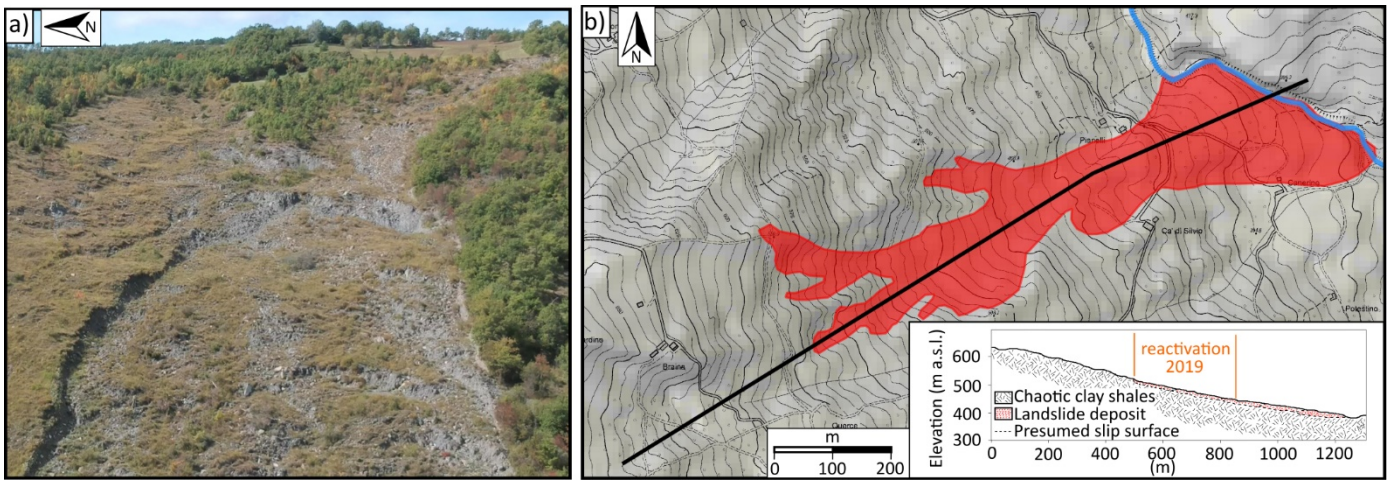


**Figure 2.** UAV (Unmanned Aerial Vehicle) photograph of Braina earthflow taken after reactivation (**a**). Schematic map and profile of the landslide deposit (**b**).

Since 1900, the landslide reactivated three times. The first event took place at the beginning of March 1934 after a prolonged rainfall [41]. Then, the landslide remained dormant for more than 60 years and reactivated a second time on 30 October 1999. According to the eyewitnesses, the landslide activated as a translational movement and then evolved into an earthflow. The reactivated area was 780 m long and between 60 and 17 m wide; the overall extent was about 47,000 $m^{2,}$ and the approximate volume 470,000 $m^3$. The landslide disrupted the minor hydrographic network, damaged a building, and destroyed the municipal road. Local authorities carried out extensive works to consolidate the slope, such as draining trenches, hydrographic network arrangement, bridles, and wooden crib walls [41]. Despite these efforts, the landslide reactivated again in late 2019, between 15 and 21 November, due to the continuous precipitation in the second half of November. The reactivated area during this event was 1250 m long and between 100 and 450 m wide. The overall extent was about 23,000 $m^2$. This event partially damaged the municipal road and destroyed most of the ditches realized in 1999.

### *2.2. The Carbona Landslide*

The Carbona landslide (Figure 3a,b) is located within the municipality of Vergato (province of Bologna, Italy). It develops on a slope composed of chaotic clay-shales belonging to the Palombini Shale Formation [40]. This landslide has been known since the first half of 1800, and, up to the present day, six activations are reported [41]. The first one occurred during the spring of 1837. The second one occurred in late 1901 and caused serious damages to the main road located at the toe of the slope. The third activation dates 28 September 1937. In this case, the reactivated portion had a length of more than 1000 m and an average width of 500 m. In this case, the landslide caused damages, such as the displacement of some meters of telegraph and electricity poles. Another activation occurred during the night between 27 and 28 November 1965, affecting a 900 m long and 150 m wide area. The last historical event took place in the night between 5 and 6 November 1979. On that occasion, the landslide showed signs of movement in the previous months (May and September, according to the reports). The failed mass had a length of 1500 m and an average width of 1000 m for an area of 300,000 $m^2$. Rainfall was the cause of the trigger. The landslide damaged a house (declared uninhabitable), forced local authorities to evacuate several families and created swellings and cracks for a stretch of about 100 m along the main road at the toe [41]. The portion that reactivated during the last event during December 2019 develops from an altitude of 308 to 564 m a.s.l. with an average slope of 16.5 degrees. During this last reactivation, the landslide moved as earthflow [19] after the persistent rainfall in mid and late November. Furthermore, In this case, damages occurred to the municipal road that crosses the slope.

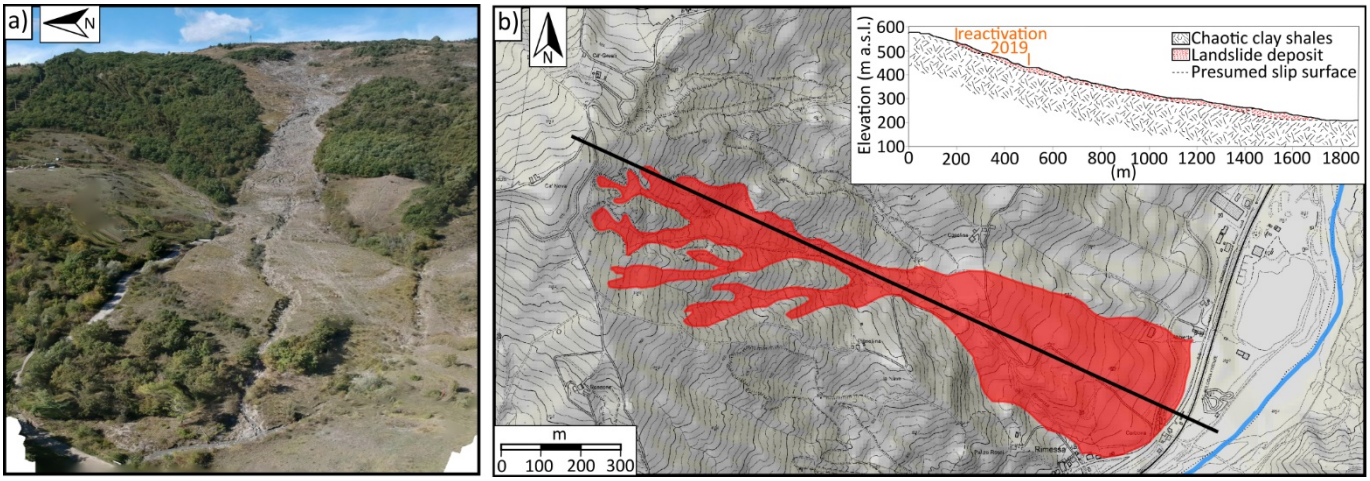


**Figure 3.** UAV photograph of the Carbona earthflow taken after reactivation (**a**). Schematic map and profile of the landslide deposit (**b**).

### *2.3. The Spareda Landslide*

The Spareda landslide (Figure 4a,b) is located within the municipality of Vergato (province of Bologna, Italy). It was last reactivated as a rotational slide [19] between 1 and 6 December 2019 due to the persistent rainfall of November.

The landslide develops between an altitude of 230 and 285 m a.s.l.; it has an average slope of 15.7 degrees, length of 1300 m and width between 50 and 150 m, with an area of about 19,000 $m^2$. During this last event, the landslide destroyed the municipal road that crosses the slope. Furthermore, this landslide is hosted by the chaotic clay-shales of the Palombini Shales [40]. The regional inventory [41] reports that a previous activation occurred during mid-March 2011. In this case, the extent of the landslide is difficult to determine exactly. Both the 2011 and 2019 reactivations were caused by rainfall, but we cannot exclude that the erosion at the foot of the slope by the Reno River [41] also had a considerable influence. This second cause may also have contributed to the reactivation that occurred during December 2019.

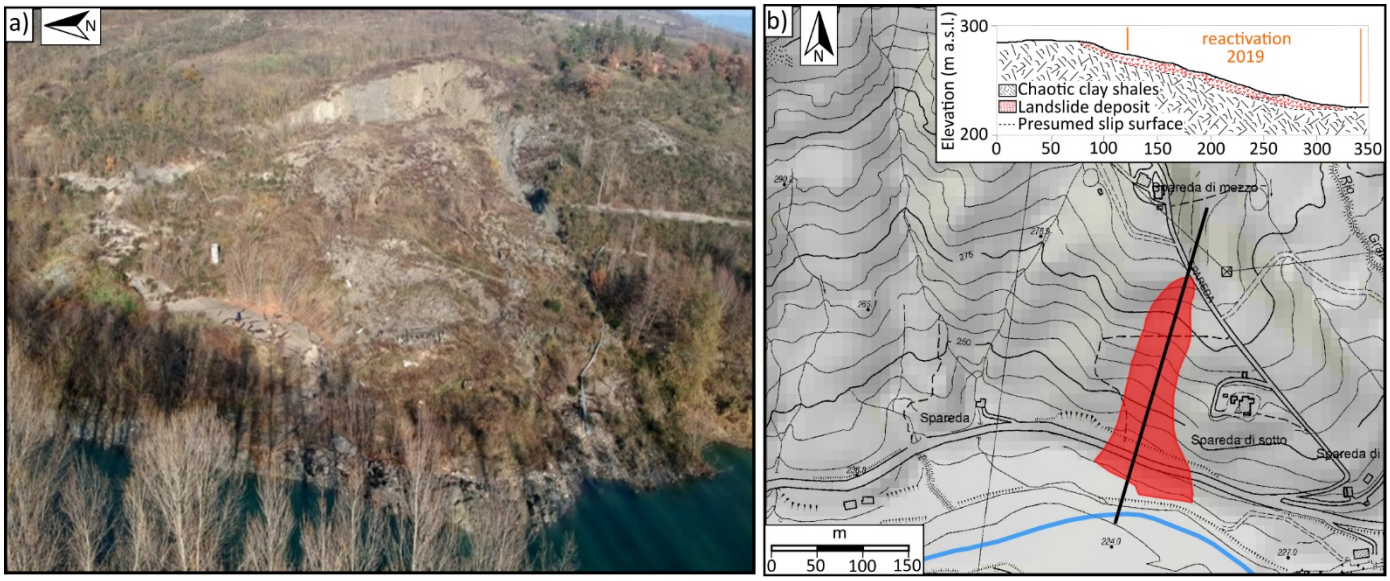


**Figure 4.** UAV photograph of Spareda landslide taken after reactivation (**a**). Schematic map and profile of the landslide deposit (**b**).

## 3. Material and Methods

### *3.1. Synthetic Aperture Radar Interferometry (InSAR): Techniques, Potentials and Limitations*

Since the first studies that used radar interferometry to map differential displacements over agricultural fields [42], synthetic aperture radar (SAR) interferometry, or InSAR, has become a useful remote sensing technique to study surface deformations [43]. Different InSAR techniques were used in the past to retrieve spatial and temporal deformation of slow slope deformations [14,20–22].

Data from numerous spaceborne synthetic aperture radar (SAR) missions with different wavelengths are available to retrieve surface deformation by radar interferometry, and the basic principles of this differential remote sensing technique are reviewed for instance, in Rosen et al. 2000 [44], Burgmann et al. 2000 [11], while examples of geological engineering applications can be found in Colesanti and Wasowski 2006 [13]. The major limitations for this technique are the following factors:

1. Phase ambiguity: The differential phase of an interferogram is measured as a fraction of the wavelength, and a deformation field is mapped in the range between $-\pi$ and $\pi$ radians. At this point, the phase is generally named wrapped phase, and in deforming areas, a spatial pattern called interferometric fringes can often be observed [45]. Switching from one end of the spectrum to the other is also commonly called phase-jump. Resolving this phase-ambiguity to obtain absolute values requires a process that is called phase unwrapping and can be solved numerically by different approaches [46,47];
2. Decorrelation: Especially in rural or densely vegetated areas, decorrelation of the interferogram can happen [48]. It is mainly due to surface changes between two acquisitions (temporal decorrelation), which can result from high deformation rates, rapid vegetation growth, snow cover or the long period of the interferogram. Decorrelation may also occur if the distance of the sensors between two acquisitions (known as perpendicular baseline) is large, which is called baseline decorrelation. If coherence is low, unwrapping will also be more problematic [49];
3. Phase noise: Even if the interferometric phase is coherent, it could contain unwanted residual noise due to the differential phase generated by DEM errors, atmospheric phase delay, and orbital inaccuracies [49–51].

Several multitemporal techniques, such as persistent scatterers interferometry [10,17,52], small baseline techniques [9–18], or hybrid approaches [53], were developed to address the problems of decorrelation and estimate different error terms of the phase. More recently, various authors [8,22,25] have shown that traditional two-pass interferometry can be successfully used to investigate gravitational slope movements thanks to shorter satellite revisit intervals and/or improved radar image quality.

### *3.2. InSAR Dataset and Processing*

In this work, synthetic aperture radar images captured by Copernicus Sentinel 1 A-B satellites were used. These images are acquired in C-Band (5.6 cm radar wavelength). The acquisition intervals are 12 days before August 2016 and reach 6 days after the launch of Sentinel 1 B. Interferogram processing was done using GMTSAR [53], and interferograms were unwrapped with the statistical-cost network-flow algorithm SNAPHU [46]. We studied the period between January 2015 and December 2019 by analyzing two ascending and two descending orbits (for a total of four datasets for each landslide). The orbits used are the following: track 15 and 117 (ascending); Track 168 and 95 (descending). In general, we obtained better quality results in terms of coherence from tracks 117 and 95, which is why the results described here are obtained from those datasets. We performed an areal InSAR analysis over the whole study area to identify landslides showing deformation signals with a certain temporal continuity. Then, to analyze the extent and time interval of the deformation in more detail, a site-specific analysis was developed for each landslide. The topographic phase was calculated and subtracted [11,45] by using a digital surface model ($2 \times 2$ m$^2$ DSM, provided by the Emilia Romagna Region Services). Large-scale

atmospheric noise was treated and reduced by selecting a stable reference area as close as possible to each investigated landslide. All the stable reference areas used in the different analyses were selected in areas outside the deforming regions, typically w.r.t. anthropic features (e.g., stable buildings) located near the landslides of interest. In addition, Gaussian and Goldstein filters [54] were applied to reduce the noises, eliminate phase differences related to other factors (atmospheric, etc.) and enhance the deformation signals due to landslide displacements. In periods characterized by high displacement rates, unwrapping problems continued to occur despite the acquisition frequency of six days. Only in these cases, we adopted a method proposed by Handwerger et al. 2015 [22], which consists of using a deformation model to aid the unwrapping problem. Both for the areal and the site-specific InSAR analyses, approximately 3000 interferograms were processed and inspected carefully. The inspection is accompanied by a coherence measurement, which is generally satisfactory given the small size of the temporal baseline. Based on our experience, the evaluation of the average coherence is only partially helpful, and the visual inspection of the interferograms is crucial. In fact, interferograms with high coherence values may contain noticeable residual noise and be discarded, while interferograms with low coherence values may contain displacement information that includes them in the selected dataset. Only the interferograms, where residual noise was relatively low and where the phase ambiguity was correctly solved, were used in the final analyses. The temporal baselines of selected interferograms have intervals of 6, 12 and 24 days, while the spatial baselines never exceed 200 m.

## 4. Results

### *4.1. InSAR Areal Analysis*

The areal InSAR analysis was performed over the entire study area (60 km$^2$) and covered the period from February 2016 to December 2019. Figure 5 reports an interferometric stack acquired in descending viewing geometry that spans the period 2018–2019. Almost the entire territory shows little or no movement, with displacement rates less than 20 mm/year (green pixels). Extensive decorrelated areas (gray/transparent pixels) are observed along the steep slopes exposed to the North.

Only four slopes show consistent signs of movement during the period of our analysis (Figure 5). Three of them (Braina, Carbona and Spareda) correspond to the landslides that suffered catastrophic failures during November–December 2019; the fourth is represented by the Marano landslide, which was reactivated during March 2018. The detected interferometric signals can be interpreted as slow downslope displacements before the reactivation. In fact, interferograms related to the late 2019 reactivation events are excluded from the areal stacking (Figure 5). Therefore, the analysis refers to the years prior to the catastrophic failure.

The analysis of the temporal evolution of deformation signals, which was developed by observing the monthly areal stacks, reveals that Braina, Carbona and Spareda were actively deforming during the entire analysis period, preceding their reactivation. The Marano landslide reactivated catastrophically in March 2018, and the deformation signal is less evident (i.e., lower average displacement rate). In this case, the deformation takes place mostly during the first months of 2018 [8], while in the post-failure phase, only small displacements are observed. According to the regional landslide database, no other landslides were exhibited high displacement rates in the study area during the observation period. Therefore, no landslides went undetected.

These results show that the InSAR analysis can provide useful information on the landslide activity for most of the mountain territory (~85%) despite the scattered and sparse presence of infrastructures. The only areas without information are the decorrelated slopes characterized by dense vegetation on steep slopes exposed to the North.

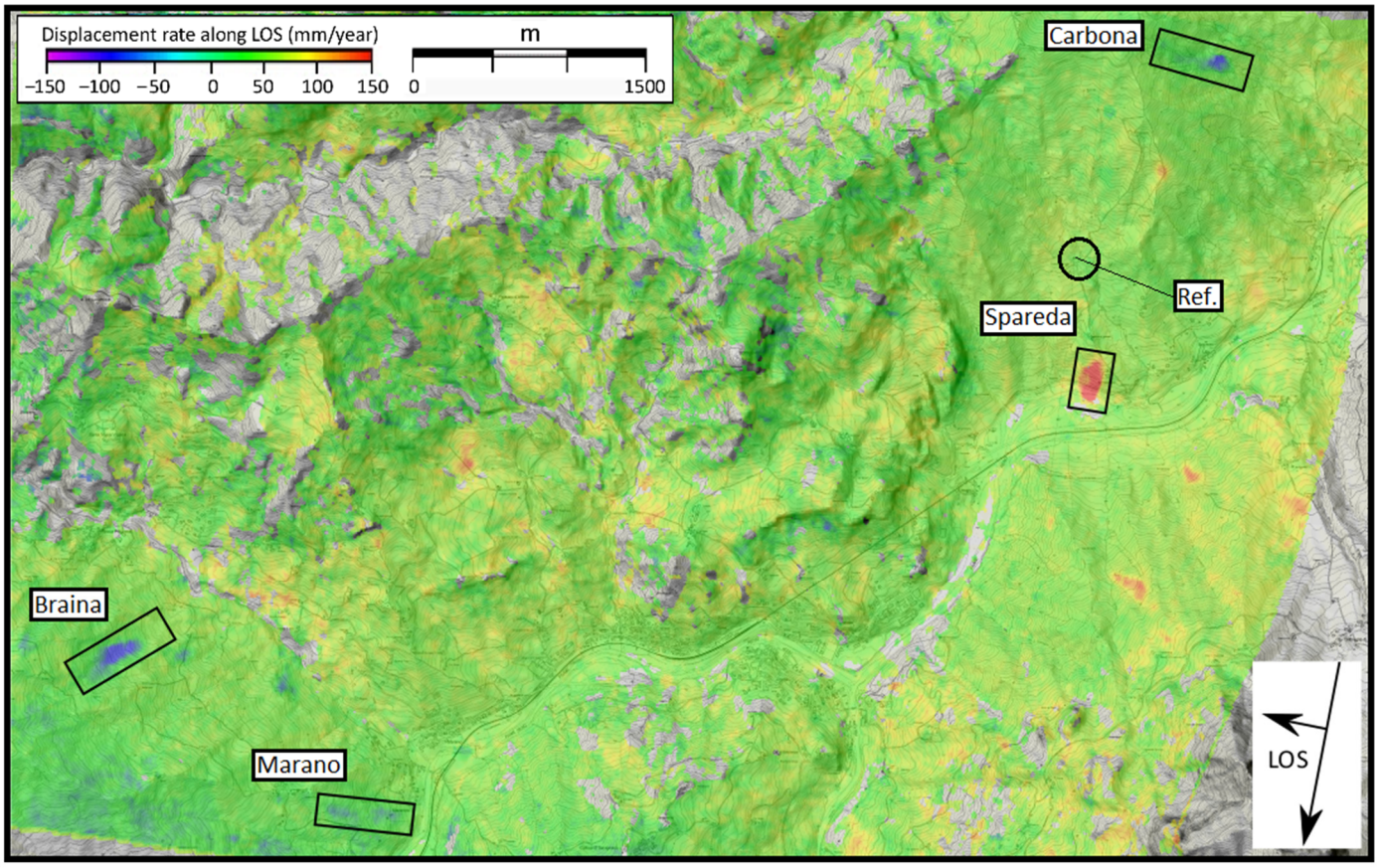


**Figure 5.** Results of areal radar interferometry (InSAR) analysis (descending orbit #95), 2018–2019 interferometric stack.

### *4.2. InSAR Site-Specific Analysis*

A site-specific analysis was carried out to obtain more detailed information about the kinematics of the three landslides detected by the areal analysis. Besides using different reference areas, we performed an independent interferogram selection for each case study. The results described below consist of deformation maps obtained by stacking the selected interferograms of the whole analysis period (2016–2019). Figure 6 shows the total stacks obtained for the ascending and descending orbits for the three case studies. The deformation fields show similar shapes in both orbits, while the direction of the displacement is inverted for the different orbits. This difference is common in landslides and should be interpreted as a displacement along the downslope direction.

As expected, in the case of Braina and Carbona, the analysis reveals positive displacement rates (movement away from the satellite) for the ascending orbit and negative displacement rates for the descending orbit along the east-facing slopes.

In the case of Spareda, the displacement signals are reverted in relation to the orbit and compatible with the south-west facing slope. The total stacks indicate that the three landslide bodies have been subject to some degree of deformation in the four years preceding the catastrophic failure.

The Braina earthflow (Figure 6a,b) has been subject to pre-failure deformations mostly affecting the upper part, between approximately 440 m and 550 m a.s.l. This area shows average values of LOS(Line Of Sight)-displacements ranging from 40 mm/year to 120 mm/year.

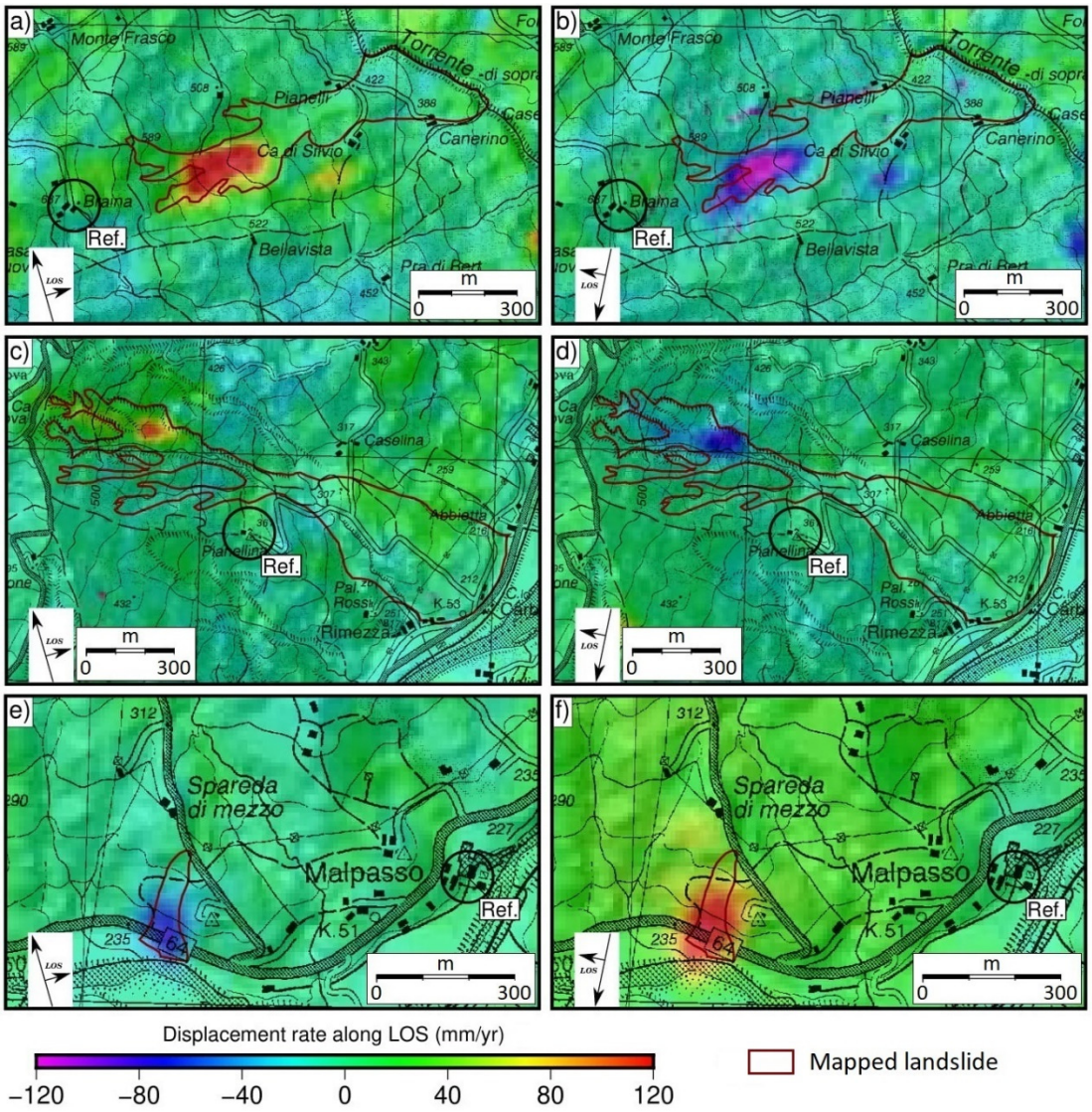


**Figure 6.** Results of site-specific analysis; stacks from January 2016 to December 2019 in both acquisition geometries for Braina (**a**,**b**), Carbona (**c**,**d**), Spareda (**e**,**f**).

Similarly, the Carbona earthflow underwent continuous deformations during the study period. Figure 6c,d shows that the upper portion of the main landslide body was affected by large displacements with maximum LOS-displacement values of 100–110 mm/year. The total stack in descending geometry (Figure 6d) gives values of the displacement rate along the LOS of 30 mm/year in the upper part (about 530 m a.s.l.); it also reveals that in the period of analysis, the whole upper portion of the main landslide body moved remarkably. The last pair of images (Figure 6e,f illustrate the Spareda landslide, showing the area affected by deformations during the four years preceding the landslide reactivation. In this case, the landslide is smaller, and the displacement signal entirely covers the mapped landslide. The movements extend from the toe of the landslide, locally incised by the Reno River at an altitude of 220 m a.s.l., up to 580 m a.s.l. The maximum displacement along the LOS exceeds 120 mm/year. The movements also affect the Municipal Road running along the slope, which was damaged by the landslide reactivation of November 2019. The descending orbit is almost parallel to the direction of movement of the Spareda landslide, while the ascending orbit forms an azimuth angle of 25–30°. Therefore, the descending dataset solely detects the vertical component of movement, while the ascending record a combination between vertical and horizontal. The

observed LOS-deformation signals are compatible with a downslope movement whose vertical lowering component can only be seen from the descending orbit. The ascending orbit, instead, records the vertical (range increase) and the horizontal components (range decrease) with opposite signs indicating that the latter is larger, as demonstrated by the negative LOS-displacement sign.

In order to investigate the dynamics of deformation through time, short timescale stacks can be used. We analyzed monthly stacks during the four year investigation period and discuss some of them below. Figure 7 shows the Carbona landslide's evolution in October and November 2019, the two months preceding the reactivation of the landslide, in ascending geometry.

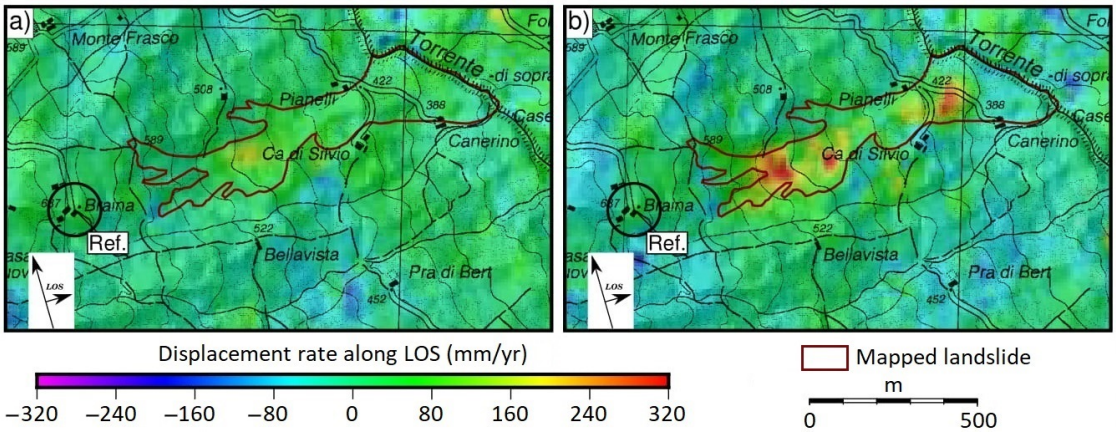


**Figure 7.** Monthly stacks were obtained for the period preceding the reactivation (15–21 November 2019). October (**a**), November (**b**).

During October (Figure 7a), the moving area is small and located between 480 m and 510 m a.s.l. The maximum displacement rates along the LOS reach about 250 mm/year, indicating an ongoing relevant acceleration when compared to typical velocities of dormant/inactive earthflow [31]. In November, the moving area is clearly larger and involves a large portion of the medium-upper earthflow body, at a short distance from few houses and a secondary road. LOS-displacement rates exceed locally 300 mm/year. The progressive acceleration that occurred in October and November 2019 preceded the reactivation of the earthflow that happened at the beginning of December. The corresponding monthly stacks capture the highest displacement rates within our analysis period. In the four years preceding the catastrophic failure, lower speeds were recorded, with minimum values during the summer and winter seasons and relatively higher values during spring and autumn. The average of all these speed values leads to the numerical values in Figure 6.

In the case of Spareda, we report three pairs of wrapped and unwrapped interferograms (Figure 8). The images are obtained by processing SAR data acquired from the ascending track 117. The temporal baseline of each interferogram is six days. The first pair (Figure 8a,b) precedes the failure, the second pair (Figure 8c,d) includes the reactivation date, and the last (Figure 8e,f) follows the failure. Cold colors and negative values indicate that displacements are towards the satellite, while warm colors and positive values describe displacements away from the satellite along the LOS.

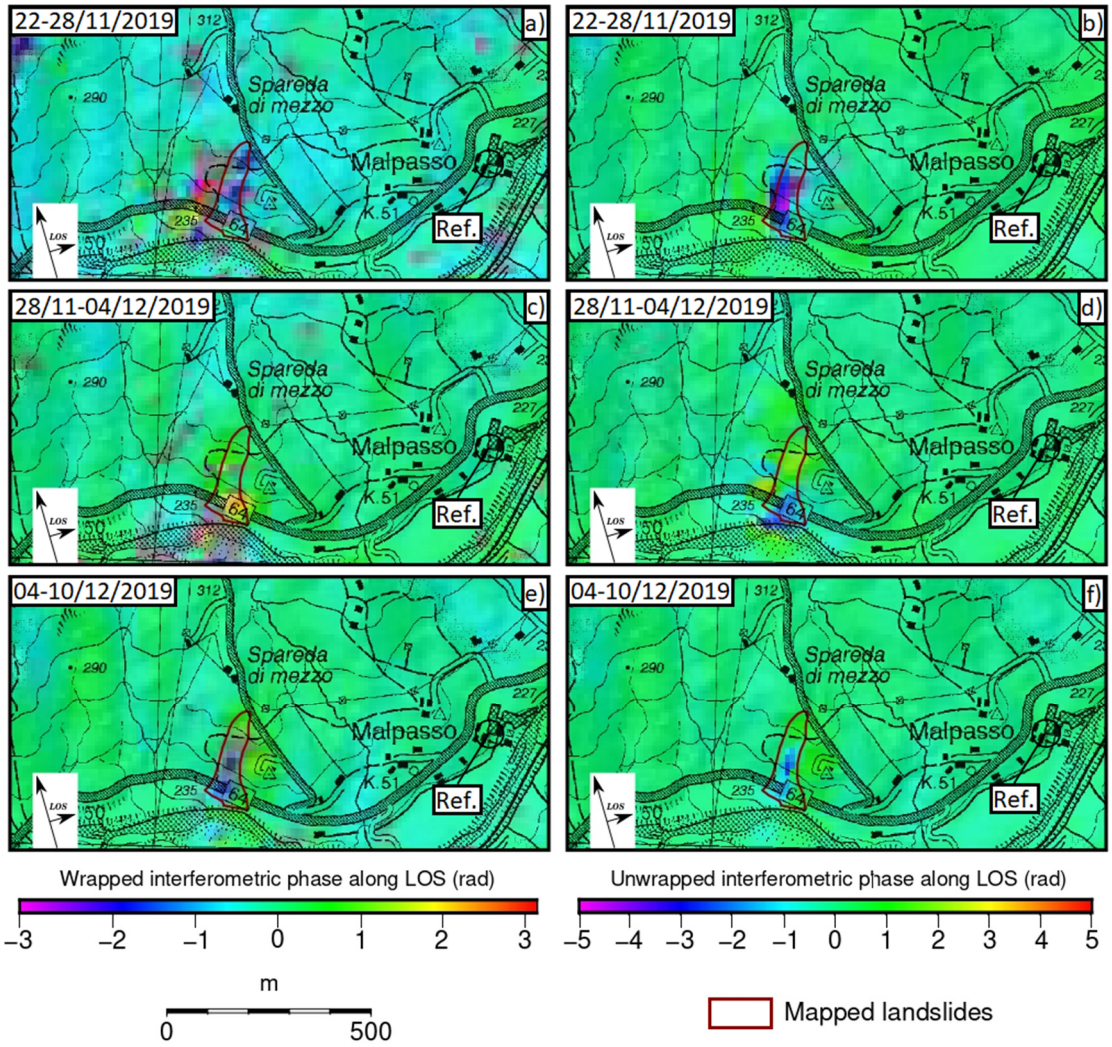


**Figure 8.** Six-day interferograms are covering the period of the Spareda landslide reactivation. Wrapped interferograms are reported in the left column (**a**,**c**,**e**) and corresponding unwrapped in the right column (**b**,**d**,**f**).

Figure 8a shows interferometric fringes that were correctly unwrapped into the range decrease in Figure 8b. Figure 8c is decorrelated on the landslide body because of the ongoing failure, and multiple phase jumps are visible ("fast-displacement decorrelation"). The phase ambiguities are only partially resolved, and it is possible that more than one cycle got lost, which is why the unwrapped displacements underestimate the true displacements (Figure 8d). It is worth noting that the range increase (movement away) from the satellite in the upper part could also be caused by a relevant vertical component due to the rotational kinematics of sliding. The last pair of images (Figure 8e,f) show again lower displacement rates with interferometric fringes that were correctly unwrapped. The signal indicates sustained sliding with displacements in directions away from the satellite in the upper part of the landslide body (surface lowering) and towards the satellite at the bulging toe.

### *4.3. InSAR Analysis: Areal vs. Site-Specific (the Example of Spareda)*

In this section, we use the Spareda case study to describe the differences observed between areal and site-specific results. As an example, we considered three months in spring 2019. Figure 9 shows the comparison between the stacks obtained by the areal (a,b) and the site-specific InSAR analyses (c,d) for the ascending (a,c) and descending orbits (b,d).

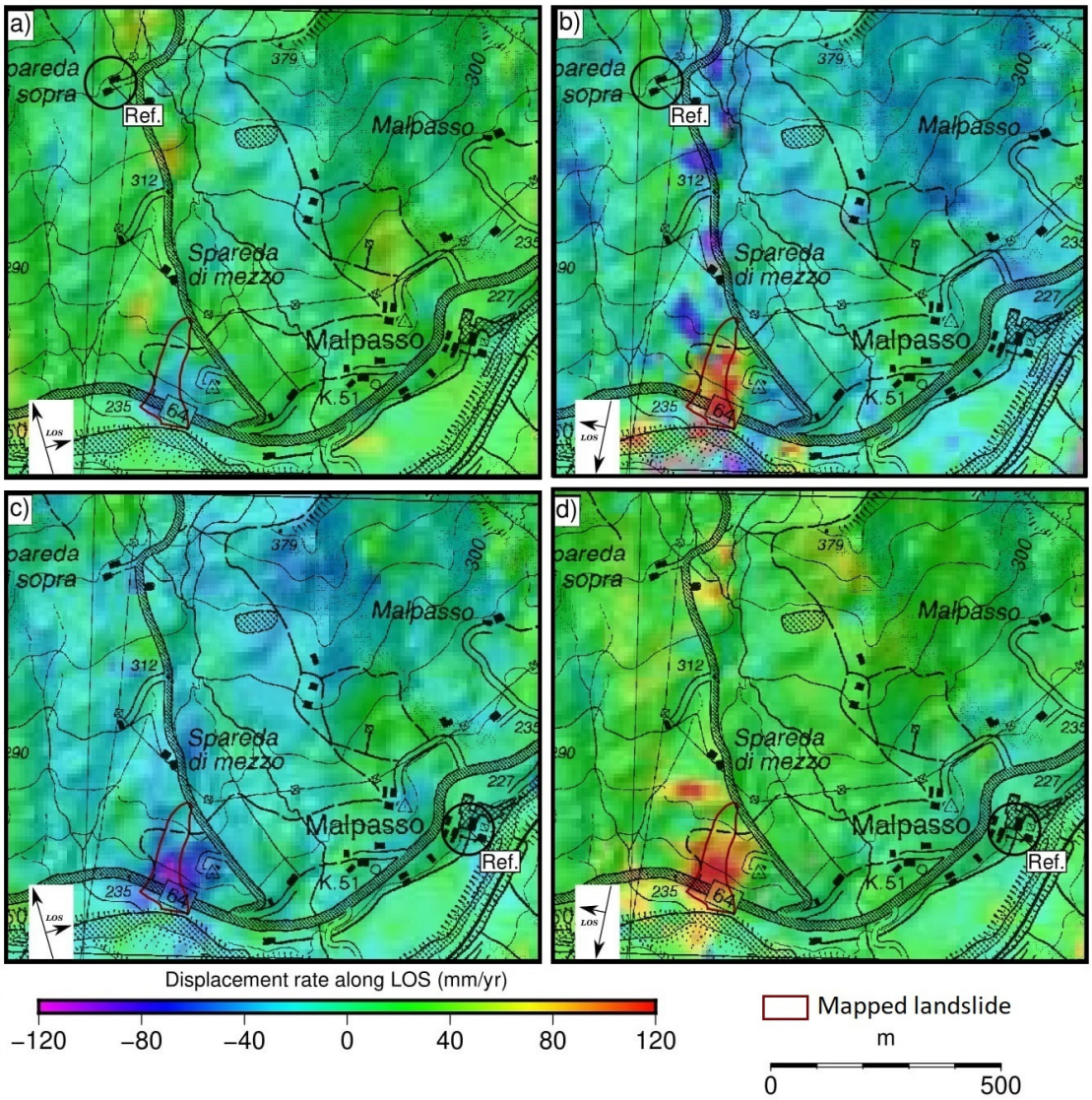


**Figure 9.** Comparison between three-month stacks obtained by the areal InSAR analysis (**a**,**b**) and site-specific InSAR analysis (**c**,**d**) for the ascending (**a**,**c**) and descending orbits (**b**,**d**).

The results indicate that the areal analysis can be used successfully to locate active landslides (Figure 9a,b), while the site-specific analysis improves the quality of results, both in terms of the spatial pattern of the signal as well as in terms of absolute velocities. The fact that the areal datasets contain higher residual noise can be explained by the different processing parameters. When working on a regional scale, compromises regarding the reference area but also regarding the interferograms included in the analyses must be made. It is, for example, possible that the overall coherence of an interferogram is good and will be included in the areal analysis. However, the same interferogram may be decorrelated on a specific landslide and would be excluded in the local-scale analysis.

During spring 2019, the areal analysis clearly reveals the deformation signal only in the descending dataset, but it provides lower quality data in the area outside the landslide; the displacement values along the LOS are also less accurate with this kind of analysis. The site-specific analysis is more accurate, showing less noisy results due to a more successful unwrapping process and of a careful site-specific interferogram selection.

### *4.4. Time Series vs. Precipitation Values*

Site-specific results describe a complex behavior of sustained deformation occurring on the landslides in the four years preceding their reactivation. In order to describe

the temporal evolution of the three phenomena, we calculated the mean velocity of the deformation signal in the landslide for each monthly interferometric stack (i.e., July velocity is measured in the stack covering the period 1 to 31 July). The extraction polygon used to obtain the data reported in the time series (Figure 10) corresponds to the extension of the most intense deformation signal visible in Figure 6. It has an extension of 50,371 $m^2$ for Braina, 28,035 $m^2$ for Carbona and 8846 $m^2$ for Spareda. Figure 10 shows the time series obtained for the three landslides compared with precipitation data. The precipitation values are represented with the cumulated equivalent rain of 30 days that includes snow melting. The calculation is performed on a daily basis by summing the values pertaining to the preceding 30 days.

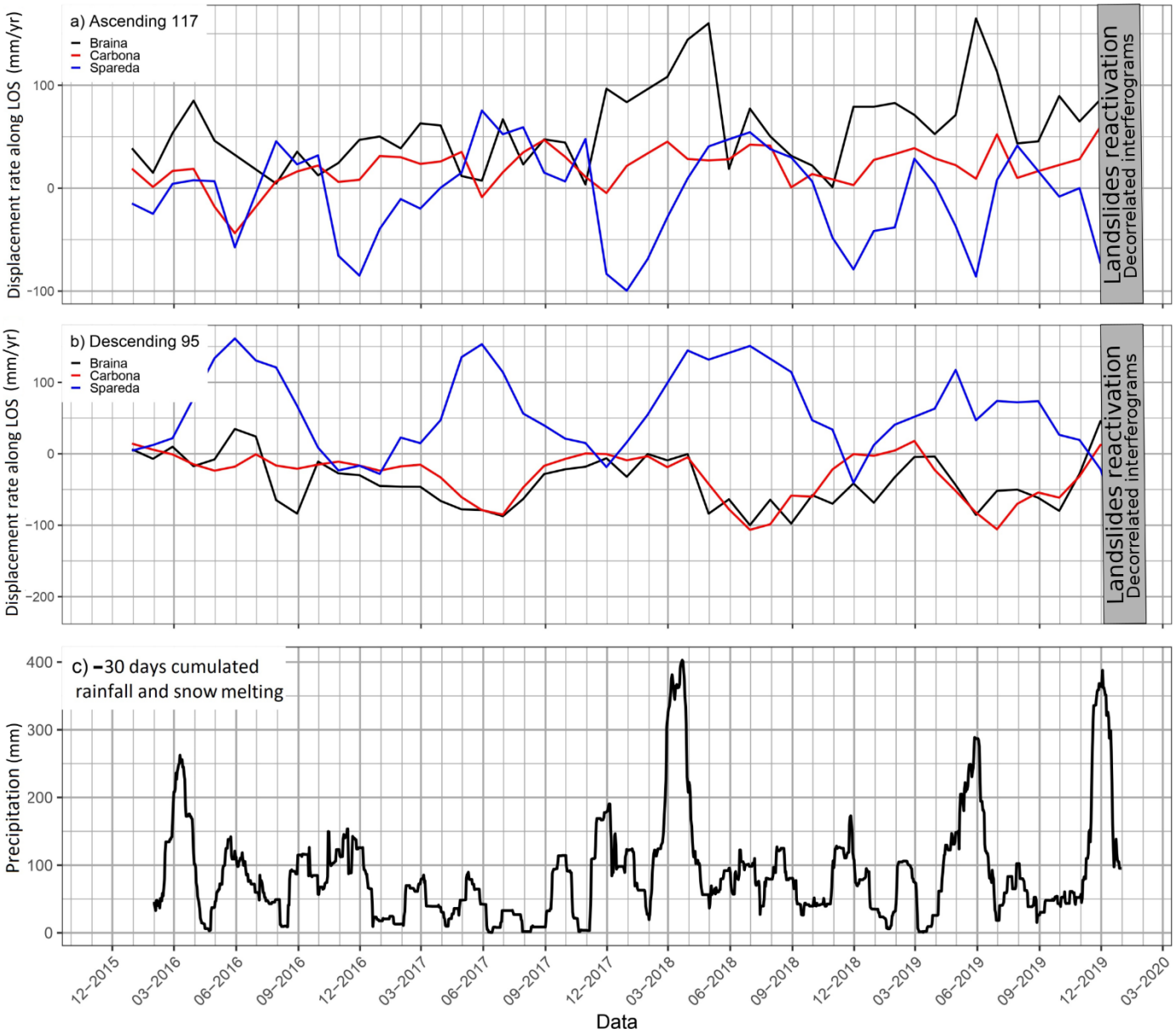


**Figure 10.** Time series of LOS (Line Of Sight) displacements rate for the ascending (**a**) and descending (**b**) orbits compared to 30 days cumulated precipitation calculated on a daily basis (**c**).

The major acceleration episodes are roughly synchronous for the three landslides and can be related to the wettest periods (March–April 2018, May and late 2019).

The comparison of the results obtained from the two orbits serves as a brief discussion. Ideally, in the case of gravitational slope movements, the displacement rate values mea-

sured by the ascending (looking eastward) and descending (looking westward) geometry should be opposite in sign when slopes have preferential east or west plunge and moderate steepness. The module would also be similar, provided the two geometries are symmetrical with respect to the direction of movement. Typically, however, the displacement signal is clearer in one of the two geometries. This is true for Braina and Carbona, where the ascending and descending LOS-displacement rates are, respectively, higher.

The main 30-day cumulative rainfall peaks occurred in March–April 2018, May 2019 and November–December 2019, the latter being the rainfall that triggered the reactivation of our case studies. Comparison of the first rainfall peak with the time series of displacement rates (Figure 10) suggests that Braina and Spareda experienced an acceleration during the precipitation, leading to displacement rate peaking occurring from April to May of the same year. The values exceed 100 mm/year and have an antithetic sign in the ascending and descending orbit. In the case of Carbona, a smaller acceleration is captured by the ascending dataset, but maximum displacement rates are relatively low (about 50 mm/year), and no corresponding acceleration is measured by the descending data.

Therefore, we do not interpret this information as completely reliable.

After the rainfall peak in May–June 2019, the deformation response has a similar pattern. In ascending orbit, we observe a clear acceleration in June for the Braina and Spareda case studies (Figure 10). Again, the response at Carbona is less clear and uncertain.

Using the analysis of individual interferograms as a complementary contribution, it seems that the peak of rainfall in late 2019 caused an increase in the displacement along the LOS, for both orbits, from the beginning of November. The descending results (Figure 10a red line) show a more impulsive response to the rainfall event. The acceleration that preceded the catastrophic failure in late 2019 is captured by the ascending dataset for all three cases. It shows an increase in the LOS displacement rate since November, i.e., since the onset of the rains.

For the Spareda landslide, the results obtained from ascending and descending acquisition are different because of the peculiar orientation of the satellite tracks compared to the direction of movement. Figure 10 shows phases where the antithesis between the two orbits is evident and others, such as December 2018, where such antithesis is not respected. In addition, in March 2018, there is a clear movement recorded in the descending dataset as a range increase, while in the ascending one, a decreasing LOS-velocity is observed. Such behavior probably results from the combination of vertical and horizontal movement associated with the prevailing downslope deformation (Figure 10a,b blue line). In this case, we interpret the data as the result of the relative orientation between the main direction of movement (i.e., SSW) and the satellite LOS. The observations are compatible with slope-parallel movement or with roto-translational sliding. This latter may contribute to additional vertical displacement whose effects are the only measured in descending geometry and that, instead, contribute to decrease the negative velocity measured in ascending geometry.

The second rainfall peak, in May 2019, shows a marked relationship with the time-series of the ascending orbit (Figure 10a). The acceleration starts with the rain and peaks in June. Later, during the same year, the rains of November caused a progressive acceleration of the movement until the landslide reactivation caused widespread decorrelation. This acceleration is more pronounced in the ascending dataset, which, in the case of Spareda, often appears more reliable compared to the descending.

## 5. Discussion and Conclusions

Our work is conceived following the reactivation of existing landslides in the Northern Apennines of Italy caused by the rains of autumn 2019. We selected three cases of reactivation and the area that includes them (about 60 $km^2$) to investigate the dynamics of gravitational slope movements by means of radar interferometry. Our aim is to detect and investigate active slope movements on an areal basis during the four years preceding the reactivations (2015–2019). Focused, site-specific analyses were then performed on the

three landslide cases to improve the quality and temporal resolution of the remotely sensed displacement information.

The areal mapping of deformation phenomena is performed using traditional two-pass differential interferometry, which helped to overcome the limitations that more rigorous multi-temporal approaches typically exhibit over largely vegetated areas where man-made structures or rock outcrops are sparse [55]. In our study, area good quality reflectors are rare, and only the large deep-seated landslides with small villages and houses on top can be assessed in detail via multitemporal InSAR approaches [15]. Traditional interferometry was used in the past over large areas taking advantage of long-wavelength (L-band) data from ALOS [14,22,56]. Due to the high acquisition frequency and small spatial baseline, C-band Sentinel data have also recently proved suitable for obtaining high-quality interferograms on landslides similar to the ones described in this paper [8,25].

From a technical point of view, our areal analysis results indicate that traditional InSAR can deliver almost continuous deformation maps of mountainous areas of the Northern Apennines characterized by a gentle slope (15–35°) and variable vegetation cover. Based on our experience, this latter prevents the detection of a coherent interferometric signal only when represented by dense forest cover. To detect sustained deformation through time that may correspond to active landslides, we use variable-duration stacked interferograms. This way, residual noise and artifacts are minimized, and displacement rates are averaged.

Our areal results show that stacked interferograms are useful to identify slope movements against surrounding stable slopes. During the 4 years of investigation, only 4 out of the 186 landslides mapped in the study area exhibited clearly recognizable deformation signals. Three of them correspond to the 2019 reactivations, and the fourth is represented by a landslide reactivated in March 2018. The analysis did not detect any noticeable and sustained movement neither on the remaining 182 mapped landslides nor along other slopes where first-time landslides may develop. Although the small number of moving landslides does not allow for statistical considerations, these results suggest that landslides prone to catastrophic reactivation are subject to measurable deformations for months or years before the actual failure occurs. In our case, failures were triggered by heavy and intense rainfall events whose occurrence cannot be predicted except in the short-term. However, detecting deformation signals using areal InSAR analysis may prove useful to identify active, slow-moving landslides more susceptible to reactivations than similar dormant cases. In the latter, the deformation could actually be absent or so slow that traditional InSAR (<3–4 cm per year) cannot detect it.

The areal InSAR analysis can also help to document the spatial evolution of the slope movements. For this purpose, the analysis must consider shorter interferometric stacks (seasonal to monthly) or even single interferograms. On a large scale, both exhibit an increasing presence of artifact or noise-related signals that make interpretation difficult. Therefore, we performed more focused analyses on the three active landslides reactivated at the end of 2019. The landslides can be classified as earthflows. They develop along gentle slopes made of chaotic clay shales and, like many others in our study area, exhibit a flow-like morphology associated with dominant sliding [31].

Site-specific analysis confirms that the earthflows were subject to noticeable deformation in the years preceding the reactivation. In the two larger cases (Braina and Carbona), ongoing deformation was concentrated in the upper part of the earthflow where multiple headscarps feed the main earthflow body, while in the smaller landslide (Spareda), the pre-failure deformation affected the whole body. In all cases, pre-failure deformation progressed with yearly averaged values of 60–90 mm/year and peak monthly values about twice.

During the reactivation phase, multiple phases jumps appear in the interferograms of the landslides. Given coherence is otherwise satisfactory, such a type of signal can be attributed to relatively fast displacements. However, it is difficult to correctly resolve the wrapped phase (Figure 9) even using the forward modeling of deformation [22–25]. We

believe that this is essentially due to the uneven deformation occurring on the surface that is favored by open crevices and fissures along, which high differential displacements occur. Despite unwrapping problems, during the November 2019 failure, interferograms show both surfaces lowering in the upper source area and bulging at the toe for the Spareda landslide (Figure 8). Such deformation pattern is compatible with a sliding style of movement, including some rotational components. In the two larger earthflows, instead, the reactivation interested only the upper source area and did not reach the accumulation zone.

Velocity variations during the pre-failure stage are well documented by the velocity time series that we measure monthly for each satellite track (Figure 10). Displacement rates range from virtually null values to more than 100 mm/month. The interpretation of velocity time series must consider the results derived from both flight geometries and the effects that the relative orientation between slope orientation and satellite LOS produce on the same results. We recognize that the quantitative meaning of displacement rates must be taken with great caution due to inherent uncertainties. However, the time-series show interesting qualitative trends. Late summer velocity decline is generally observed though the general trend cannot be described as seasonal but rather dependent on the rainfall regime. Repeated accelerations are generally observed during the wettest periods with delayed peaking compared to 30 days cumulated rainfalls. Interestingly, the reactivation of late 2019 occurred in coincidence with the peak of a rainfall period with no appreciable delay. Though capable of registering acceleration in the month preceding failure, our InSAR measures do not show any exceptionality compared to other accelerations, therefore, being of little use for the prediction of the time of failure. However, our analysis demonstrates that major precipitation events on a weekly to monthly scale are the main drivers of landslide accelerations and reactivations in our study area. More particularly, the catastrophic earthflow reactivations that occurred during the 4 year investigation period were caused by rainfalls and snow-melting episodes that exceeded 300 mm on a monthly basis. Unlike other authors, [14] we do not observe a clear trend of seasonal velocity variation, but rather, a general tendency to attain the lowest yearly velocities during late summer.

To conclude, we believe that traditional two-pass interferometry can be useful to investigate the dynamics of landslides. From a spatial perspective, it provided good coverage of the territory and proved capable of detecting active slope movements in the LOS-velocity range of few centimeters to few tens of centimeters per year. From an evolutionary perspective, it allows capturing the main landslide dynamics on a monthly, or possibly shorter, scale.

**Author Contributions:** Conceptualization, P.C. and A.S.; methodology, B.B., S.F. and A.S.; processing, P.C. and B.B.; validation, B.B., S.F. and M.B.; field investigation, P.C. and M.B.; writing—original draft preparation, P.C. and A.S.; writing—review and editing, P.C., B.B., S.F., M.B. and A.S.; supervision, A.S. All authors have read and agreed to the published version of the manuscript.

**Funding:** This research received no external funding.

**Institutional Review Board Statement:** Not applicable.

**Informed Consent Statement:** Not applicable.

**Data Availability Statement:** The data presented in this study are available on request from the corresponding author. The data are not publicly available due to their complex structure and storage limitations.

**Conflicts of Interest:** The authors declare no conflict of interest.

## References

1. Schuster, R.L. Socioeconomic significance of landslides. *Transp. Res. Board Spec. Rep.* **1996**, *247*, 12–35.
2. Casagli, N.; Catani, N.; Del Ventisette, C.; Luzi, G. Monitoring, prediction and early warming using ground-based radar interferometry. *Landslides* **2010**, *7*, 291–301. [CrossRef]

3. Bertolini, G.; Casagli, N.; Ermini, L.; Malaguti, C. Radiocarbon data on lateglacial and holocene landslides in the northern Apennines. *Nat. Hazards* **2004**, *31*, 645–662. [CrossRef]
4. Bertolini, G.; Pellegrini, M. The landslides of the Emilia Apennines (northern Italy) with reference to those which resumed activity in the 1994–1999 period and required Civil Protection interventions. *Quad. Geol. Appl.* **2001**, *8*, 27–74.
5. Mantovani, F.; Soeters, R.; Van Westen, C.J. Remote sensing techniques for landslide studies and hazard zonation in Europe. *Geomorphology* **1996**, *15*, 213–225. [CrossRef]
6. Hervás, J.; José, I.B.; Rosin, P.L.; Pasuto, A.; Mantovani, F.; Silvano, S. Monitoring landslides from optical remotely sensed imagery: The case history of Tessina landslide, Italy. *Geomorphology* **2003**, *54*, 63–75. [CrossRef]
7. Metternicht, G.; Hurni, L.; Gogu, R. Remote sensing of landslides: An analysis of the potential contribution to geo-spatial systems for hazard assessment in mountainous environments. *Remote Sens. Environ.* **2005**, *98*, 284–303. [CrossRef]
8. Squarzoni, G.; Benedikt, B.; Franceschini, S.; Simoni, A. Pre- and post-failure dynamics of landslides in the Northern Apennines revealed by space-borne synthetic aperture radar interferometry (InSAR). *Geomorphology* **2020**, *369*, 107353. [CrossRef]
9. Schmidt, D.; Bürgmann, R. Time-dependent land uplift and subsidence in the Santa Clara valley, California, from a large interferometric synthetic aperture radar data set. *J. Geophys. Res. Solid Earth* **2003**, *108*, 2416. [CrossRef]
10. Hooper, A.; Zebker, H.; Segall, P.; Kampes, B. A new method for measuring deformation on volcanoes and other natural terrains using insar persistent scatterer. *Geophys. Res. Lett.* **2004**, *31*, L23611. [CrossRef]
11. Bürgmann, R.; Rosen, P.A.; Fielding, E.J. Synthetic aperture radar interferometry to measure earth's surface topography and its deformation. *Annu. Rev. Earth Planet. Sci.* **2000**, *28*, 169–209. [CrossRef]
12. Fialko, J.; Simons, M.; Agnew, D. The complete (3-D) surface displacement field in the epicentral area of the 1999 M(w) 7.1 Hector Mine earthquake, California from space geodetic observations. *Geophys. Res. Lett.* **2001**, *28*, 3063–3066. [CrossRef]
13. Colesanti, C.; Wasowski, J. Investigating landslides with space-borne Synthetic Aperture Radar (SAR) interferometry. *Eng. Geol.* **2006**, *88*, 173–199. [CrossRef]
14. Handwerger, A.; Roering, J.; Schmidt, D. Controls on the seasonal deformation of slow-moving landslides. *Earth Planet. Sci. Lett.* **2013**, *377*, 239–247. [CrossRef]
15. Bayer, B.; Simoni, A.; Schmidt, D.; Bertello, L. Using advanced InSAR techniques to monitor landslide deformations induced by tunneling in the Northern Apennines, Italy. *Eng. Geol.* **2017**, *226*, 20–32. [CrossRef]
16. Fruneau, B.; Achache, J.; Delacourt, G. Observation and modelling of the saint-etienne-de-tinée landslide using sar interferometry. *Tectonophysics* **1996**, *265*, 181–190. [CrossRef]
17. Ferretti, A.; Prati, C.; Rocca, F. Permanent scatterers insar interferometry. *IEEE Trans. Geosci. Remote Sens.* **2001**, *39*, 8–20. [CrossRef]
18. Berardino, P.; Fornaro, G.; Lanari, R.; Sansosti, E. A new algorithm for surface deformation monitoring based on small baseline differential sar interferograms. *IEEE Trans. Geosci. Remote Sens.* **2002**, *40*, 2375–2383. [CrossRef]
19. Cruden, D.M.; Varnes, D. *Landslides: Investigation and Mitigation. Chapter 3-Landslides Types and Processes. Transportation Research Board Special Report*; Transportation Research Board: Washington, DC, USA, 1996.
20. Roering, J.; Stimely, L.; Mackey, B.H.; Schmidt, D.A. Using DInSAR, airborne LiDAR, and archival air photos to quantify landsliding and sediment transport. *Geophys. Res. Lett.* **2009**, *36*, L19402. [CrossRef]
21. Bovenga, F.; Wasowski, J.; Nitti, D.O.; Nutricato, R. Using COSMO/SkyMed X-band and ENVISAT C-band SAR interferometry for landslides analysis. *Remote Sens. Environ.* **2012**, *119*, 272–285. [CrossRef]
22. Handwerger, A.; Roering, J.; Schmidt, D.; Rempel, A. Kinematics of earthflows in the northern California coast ranges using satellite interferometry. *Geomorphology* **2015**, *246*, 321–333. [CrossRef]
23. Intrieri, E.; Raspini, F.; Fumagalli, A.; Lu, P.; Del Conte, S.; Farina, P.; Allievi, J.; Ferretti, A.; Casagli, N. The Maoxian landslide as seen from space: Detecting precursors of failure with Sentinel-1 data. *Landslides* **2018**, *15*, 123–133. [CrossRef]
24. Carlà, T.; Farina, P.; Intrieri, E.; Keitzmen, H.; Casagli, N. Integration of ground-based radar and satellite InSAR data for the analysis of an unexpected slope failure in an open-pit mine. *Eng. Geol.* **2018**, *235*, 39–52. [CrossRef]
25. Handwerger, A.; Huang, M.; Fielding, E.; Booth, A.; Bürgmann, R. A shift from drought to extreme rainfall drives a stable landslide to catastrophic failure. *Sci. Rep.* **2019**, *9*, 9569. [CrossRef]
26. Boccaletti, M.; Elter, P.; Guazzone, G. Plate tectonic models for the development of the western alps and Northern Apennines. *Nature* **1971**, *234*, 108–111. [CrossRef]
27. Picotti, V.; Pazzaglia, F.J. A new active tectonic model for the construction of the Northern Apennines mountain front near Bologna. *J. Geophys. Res. Solid Earth* **2008**, *113*, B08412. [CrossRef]
28. Pini, G.A. Tectonosomes and olistostromes in the argille scagliose of the Northern Apennines, Italy. *Soc. Pap. Geol. Soc. Am.* **1999**, *335*, 1–70.
29. Vannucchi, P.; Maltman, A.; Bettelli, G.; Clennell, B. On the nature of scaly fabric and scaly clay. *J. Struct. Geol.* **2003**, *25*, 673–688. [CrossRef]
30. Ricci Lucchi, F. The Oligocene to recent foreland basins of the Northern Apennines. *Science* **1986**, *8*, 105–139.
31. Simoni, A.; Ponza, A.; Picotti, V.; Berti, M.; Dinelli, E. Earthflow sediment production and holocene sediment record in a large Apennine catchment. *Geomorphology* **2013**, *188*, 42–53. [CrossRef]
32. Borgatti, L.; Corsini, A.; Barbieri, M.; Sartini, G.; Truffelli, G.; Caputo, G.; Puglisi, C. Large reactivated landslides in weak rock masses: A case study from the Northern Apennines (Italy). *Landslides* **2006**, *3*, 115–124. [CrossRef]

33. Corsini, A.; Farina, P.; Antonello, G.; Barbieri, M.; Casagli, N.; Coren, F.; Guerri, L. Space-borne and ground-based SAR interferometry as tools for landslide hazard management in civil protection. *Int. J. Remote Sens.* **2006**, *27*, 2351–2369. [CrossRef]
34. Berti, M.; Bertello, L.; Bernardi, A.; Caputo, G. Back analysis of a large landslide in a flysch rock mass. *Landslides* **2017**, *14*, 2041–2058. [CrossRef]
35. Bertello, L.; Berti, M.; Castellaro, S.; Squarzoni, G. Dynamics of an active earthflow inferred from surface wave monitoring. *Earth Surf.* **2018**, *123*, 1811–1834. [CrossRef]
36. Berti, M.; Simoni, A. Observation and analysis of near-surface pore-pressure measurements in clay-shales slopes. *Hydrol. Process.* **2012**, *26*, 2187–2205. [CrossRef]
37. Tomozeiu, R.; Busuioc, A.; Marletto, V.; Zinoni, F.; Cacciamani, C. Detection of changes in the summer precipitation time series of the region Emilia-Romagna, Italy. *Theor. Appl. Climatol.* **2000**, *63*, 193–200. [CrossRef]
38. Tomozeiu, R.; Lazzeri, M.; Cacciamani, C. Precipitation fluctuations during the winter season from 1960 to 1995 over Emilia-Romagna, Italy. *Theor. Appl. Climatol.* **2002**, *72*, 221–229. [CrossRef]
39. Pavan, V.; Tomozeiu, R.; Cacciamani, C.; Di Lorenzo, M. Daily precipitation observations over Emilia-Romagna: Mean values and extremes. *Int. J. Climatol.* **2008**, *28*, 2065–2079. [CrossRef]
40. Panini, F.; Bettelli, G.; Bonazzi, U.; Fioroni, F.; Fregni, P. *Note Illustrative Alla Carta Geologica d'Italia a Scala 1:50.000. pp. Foglio N. 237, Sasso Marconi*; APAT: Parma, Italy, 2002.
41. Geological Seismic and Soil Service of the Emilia-Romagna Region, Historical Archive of Landslides in the Emilia-Romagna Region. 2019. Available online: http://geo.regione.emilia-romagna.it/schede/fs/fs_dis.jsp?id=60575 (accessed on 20 April 2020).
42. Gabriel, G.K.; Goldstein, R.M.; Zebker, H.A. Mapping small elevation changes over large areas: Differential radar interferometry. *Solid Earth* **1989**, *84*, 9183–9191. [CrossRef]
43. Hooper, A.; Bekaert, D.; Spaans, K.; Arikan, M. Recent advances in SAR interferometry time series analysis for measuring. *Tectonophysics* **2012**, *514*, 1–13. [CrossRef]
44. Rosen, P.A.; Hensley, S.; Joughin, I.R.; Li, F.K.; Madsen, S.N.; Rodriguez, E.; Goldstein, R.M. Synthetic aperture radar interferometry. *Proc. IEEE* **2000**, *88*, 333–382. [CrossRef]
45. Massonnet, D.; Feigl, K. Radar interferometry and its application to changes in the earth's surface. *Rev. Geophys.* **1998**, *36*, 441–500. [CrossRef]
46. Chen, C.W.; Zebker, H.A. Two-dimensional phase unwrapping with use of statistical models for cost functions in nonlinear optimization. *J. Opt. Soc. Am.* **2001**, *18*, 338–351. [CrossRef] [PubMed]
47. Hooper, A.; Segall, P.; Zebker, H. Persistent scatterer interferometric synthetic aperture radar for crustal deformation analysis, with application to Volcán Alcedo, Galápagos. *J. Geophys. Res. Atmos.* **2007**, *112*, B07407. [CrossRef]
48. Zebker, H.A.; Villasenor, J. Decorrelation in interferometric radar echoes. *Trans. Geosci. Remote Sens.* **1992**, *30*, 950–959. [CrossRef]
49. Tarayre, H.; Massonnet, D. Atmospheric propagation heterogeneities revealed by ERS-1 interferometry. *Geophys. Res. Lett.* **1996**, *23*, 989–992. [CrossRef]
50. Zebker, H.; Rosen, P.; Hensley, S. Atmospheric effects in interferometric synthetic aperture radar surface deformation and topographic maps. *J. Geophys. Res. Solid Earth* **1997**, *102*, 7547–7563. [CrossRef]
51. Fattahi, H.; Amelung, F. InSAR bias and uncertainty due to the systematic and stochastic tropospheric delay. *Solid Earth* **2015**, *120*, 8758–8773. [CrossRef]
52. Ferretti, A.; Fumagalli, A.; Novali, F.; Prati, C.; Rocca, F.; Rucci, A. A new algorithm for processing interferometric data-stacks: Squeesar. *IEEE Trans. Geosci. Remote Sens.* **2011**, *49*, 3460–3470. [CrossRef]
53. Hooper, A. A multi-temporal InSAR method incorporating both persistent scatterer and small baseline approaches. *Geophys. Res. Lett.* **2008**, *35*, L16302. [CrossRef]
54. Goldstein, R.; Werner, C. Radar interferogram filtering for geophysical application. *Geophys. Res. Lett.* **1998**, *25*, 4035–4038. [CrossRef]
55. Wasowski, J.; Bovenga, F. Investigating landslides and unstable slopes with satellite multi temporal interferometry: Current issues and future perspectives. *Eng. Geol.* **2014**, *174*, 103–138. [CrossRef]
56. Bennet, G.L.; Roering, J.; Mackey, B.H.; Handwerger, A.L.; Schmidt, D.A.; Guillod, B.P. Historic drought puts the brakes on earthflows in Northern California. *Geophys. Res. Lett.* **2016**, *43*, 5725–5731. [CrossRef]

## 4. Paper 2

**Regional-scale InSAR investigation and landslide early warning thresholds in Umbria, Italy***

Francesco Ponziani, Pierpaolo Ciuffi, Benedikt Bayer, Nicola Berni, Silvia Franceschini and Alessandro Simoni

* Submitted to **Engineering Geology**

# Regional-scale InSAR investigation and landslide early warning thresholds in Umbria, Italy

Francesco Ponziani (1), Pierpaolo Ciuffi (2), Benedikt Bayer (3), Nicola Berni (1), Silvia Franceschini (3), Alessandro Simoni* (2)

(1) Regione Umbria Civil Protection Office- Functional Centre. Foligno (Pg), Italy;

(2) Department of Biological, Geological and Environmental Sciences (BiGeA), University of Bologna, Via Zamboni 67, 40126 Bologna, Italy;

(3) Fragile s.r.l., Viale Fanin 48, 40127 Bologna, Italy;

* corresponding author: alessandro.simoni@unibo.it

**Abstract**: In this work, we use conventional two-pass differential satellite interferometry for the investigation of active landslides at regional scale in the Umbria Region of Italy. First, we use InSAR for the detection of active slope movements during the study period (October 2019 to January 2021). Then, we characterize the displacement rates and their variation through time for selected active slopes, by analysing 6-days interferograms. The evolutionary trends of the phenomena are compared to the pertaining climate and soil parameters that are used by the regional landslide early warning system (LEWS) to predict the possibility of landslide occurrence over the territory. We aim to explore the potential of differential interferometry to detect and monitor active landslides and, through that, to validate a geographical LEWS:

Through the analysis of stacked interferograms, we identified 256 InSAR deformation signals (IDS) corresponding to active slope movements. Their distribution is compared to the geological map and the landslide inventory, illustrating how active landslides are favoured by weak lithologies and pre-existing slope instability. Also, the relative orientation of the satellite's line of sight with respect to the slope influences the results indicating a bias in the completeness of remotely sensed data. However, in the context of land management and civil protection, the results constitute a valuable information dataset for plans managed by local authorities.

The analysis, at the interferogram scale (6-days), of 13 clearly recognizable IDSs illustrates the dynamics of the slopes through the variation of the displacement rates. Due to decorrelation, only about half of the interferograms can be used for this purpose, and interpretation is required. The comparison to the alert thresholds of the Umbria region show the remarkable relationship between InSAR-derived landslide activity and the parameters used for landslide prediction (i.e., 24h rainfall and soil moisture conditions). The maximum 24h cumulative rainfall and the soil saturation index prove effective to predict landslide reactivations and accelerations. We provide uncertainty measures of the landslide prediction through binary classification metrics. Such results are only preliminary, given the limited number of landslides and timespan of our dataset. However, it represents one of the few attempts to validate the forecast of a regional LEWS quantitatively.

Keywords: INSAR, LEWS, alert threshold, active landslide, landslide recognition, landslide monitoring

## 1. Introduction

Landslides shape mountainous regions where they pose a relevant hazard to people and infrastructures resulting in hundreds of deaths and billions of dollars in damages every year (Kishore et al., 2018). However, given the widespread occurrence of relatively small but damaging events (Guzzetti, 2000), the economic consequences are difficult to estimate and tend to be underestimated. The combination of a rapidly increasing global population and the intensifying weather extremes associated with recent climate change suggests that landslide risk will dramatically increase over the next decades (Gariano and Guzzetti, 2016).

Given their complex physics and the diverse nature of triggering mechanisms (e.g., rainfall, earthquakes, frost cracking), documentation of landslide dynamics through monitoring is critical for hazard evaluation and risk management. Landslide deformation can be extremely slow (a few millimetres per year) or involve sudden failure (Hungr et al., 2014), so their hazards include both enduring damage to manmade structures and catastrophic destructive events. While small landslides make up the vast majority of landslide events in any given year (Glade and Crozier, 2005), large landslides tend to be responsible for most damage and loss of life (Froude and Petley, 2018). In most regions of the world, the characterization of their locations and impacts is still problematic due to the variety of landslide types and morphologies and the difficulty of collating and updating inventories. It is thus important that we continue to develop tools and techniques to detect and monitor these gravitational slope processes.

Landslides can be mapped and monitored with field observations, digital elevation models, satellite and airborne imagery (Mantovani et al., 1996; Guzzetti et al., 2012, Chae et al., 2017). Remote sensing techniques combine the inherent advantages of their areal perspective with the remarkable precision of the more advanced radar-based methodologies (Cohen-Waeber et al., 2018). Furthermore, the number of satellite-based sensors is steadily increasing together with the frequency of acquisitions, making the observations more detailed in space and time (Mondini et al., 2021).

Interferometric processing of synthetic aperture radar images (InSAR) has proven useful to investigate gravitational slope movements both for specific landslide studies (Xu et al., 2020; Wasowski and Bovenga, 2014) and for regional analysis (Solari et al., 2020; Zhang et al., 2018). In the latter case, InSAR has been used not only for the detection of active landslides (Dini et al., 2019; Zhao et al., 2012) but also for deformation monitoring (Bekaert and Handwerger, 2020; Shi et al., 2020). However, the regional investigation of landslides through InSAR techniques is still challenging due to several factors. Landslide displacement detection and monitoring is not possible when snow cover is present while the presence of dense vegetation induces temporal decorrelation. Atmospheric delay anomalies, topographic artefacts (Liang et al., 2018; Murray et al., 2019) and decorrelation due to large deformation gradients (Hu et al., 2019, Manconi, 2021) are among the factors significantly influencing our ability to measure surface displacements. In addition, the satellite orbital geometry and the side-looking SAR imaging makes some slope orientations less favourable and causes layover and shadowing over steep mountainous terrain (Wasowski and Bovenga, 2014).

In the last decades, various interferometric techniques have been proposed to process multi-temporal SAR acquisitions over large areas. They can be grouped in two main families: standard InSAR methods that include classic two-pass interferometry and interferometric stacking (Dini et al., 2019; Handwerger et al., 2013; 2015) and multi-temporal methods that include the so-called Persistent Scatterer Interferometry (PSI) and Small Baseline Subsets (SBAS) methods (Raspini et al., 2019; Zhang et al., 2020). In general, multi-temporal methods allow obtaining better accuracy and precision for good quality reflectors (houses, infrastructures, rock outcrops) but standard InSAR yields a more continuous coverage of the territory also when sparse to medium vegetation cover is present.

Archived and newly acquired SAR images can be interferometrically processed to extract displacement time series. Their analysis can be used to determine the sensitivity of landslide motion to external factors such as seasonal precipitation and seismic shaking (Cohen-Waeber et al., 2018; Handwerger et al., 2015; Albano al., 2018) and may have a significant potential in detecting precursory deformation preceding catastrophic failures (Dong et al., 2017; Ciuffi et al., 2021; Xie et al., 2020).

This work presents the results of a regional InSAR investigation performed by using standard differential methodologies and C-band Sentinel 1 SAR images. The Umbria region of central Italy is the study area (8456 $km^2$), and our analysis covers the period between October 2019 and January 2021.

We aim to detect and map active slope movements by analysing stacked interferograms. We also intend to use the phase information contained in single differential interferograms to monitor the slope deformation through time. The use of conventional two-pass interferometry is used to achieve a better territorial coverage compared to multi-temporal techniques and to detect landslide acceleration/decelerations with the highest possible frequency (6 days).

The work compares the location of detected InSAR deformation signals (IDS) to existing geological and geomorphological information to gain understanding of their correlation. Interferograms are used to describe the evolution of selected landslide whose state of activity is compared to rainfall and soil moisture parameters. The Civil Protection of the Umbria region uses such parameters to forecast landslide occurrence over its territory and issue alert bulletins. To our knowledge, this work represents one of the first attempts of using remotely sensed displacement data to support the calibration and validation of predictive methodologies for landslide early warning systems (LEWS). Encouraging results indicate that InSAR detection of actively moving landslides can be helpful for territorial surveillance and for the development of predictive tools for geographical LEWS.

## 2. The study area and the landslide early warning system

The morphology of the Umbria Region (8456 $km^2$), located in central Italy, spans from alluvial plains to hills and mountains, with elevations ranging from 50 to 2436 m a.s.l. (Figure 1). The geology is dominated by the presence of sedimentary rocks with post-orogenic marine and continental facies, flysch deposits consisting of

clay-schist and clay-marl sediments, well-bedded limestones and subordinate volcanic rocks (Cardinali et al., 2002). Agriculture/arable land covers about 54% of the territory, forest 32% urban areas account for about 5%.

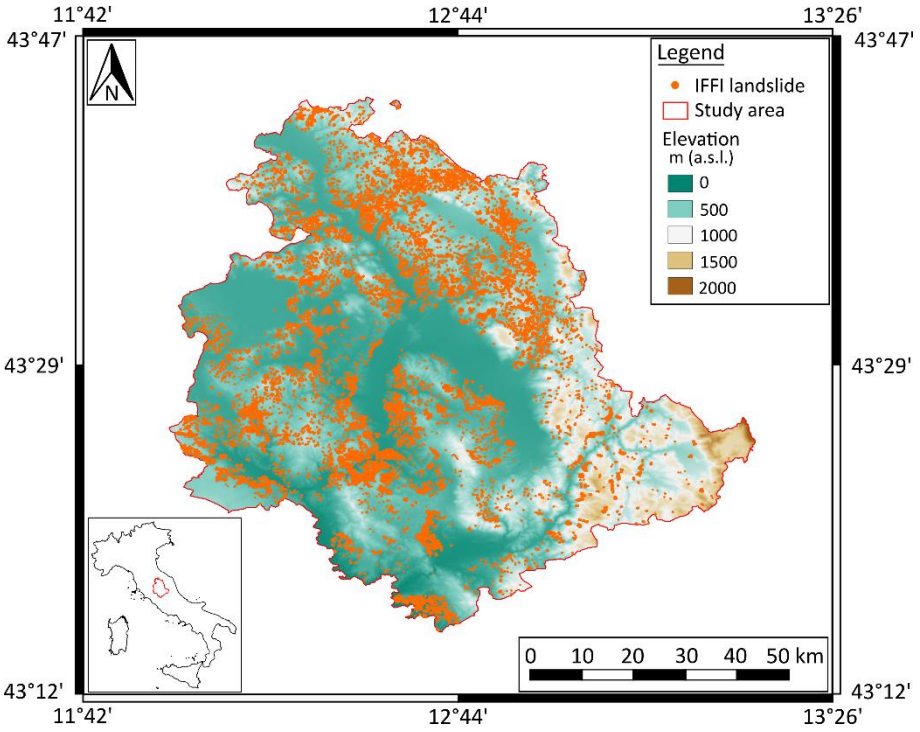


*Figure 1. Schematic elevation map of Umbria Region and distribution of the landslides mapped by the IFFI inventory.*

Landslides are widespread and recurring: all municipalities in Umbria are exposed to some degree of landslide risk, and landslide deposits cover about 9% (650 km$^2$) of the area. According to the national inventory IFFI (Trigila et al., 2010), more than 70% of the 12477 mapped landslides are dormant while the remaining are active, mostly based on geomorphological criteria.

The precipitation regime can be classified as Mediterranean. There are distinct dry and wet seasons, with Mediterranean-type precipitation regime, higher generally during the autumn-winter period when landslides and floods are more common. Mean annual precipitation is about 1000 mm; mean annual temperature is 11°C; snowfalls at altitude below 500 m are sporadic and unusual.

In Italy, each region is in charge of monitoring, and forecast weather phenomena and weather-related natural risks in real time. The landslide early warning system (LEWS) of the Umbria region aims to predict conditions of local (first level alert) or widespread (second level alert) landslide occurrence over the territory which is divided in six alert zones (> 500 km$^2$) for this purpose. Landslide hazard scenarios are updated every 24 hours and support the decision-making authorities with a first-order regional alert procedure.

Given the uncertainties inherent to landslide prediction (Chae et al., 2017), the daily forecast is based on simplified, empirical systems. Most methods rely on precipitation parameters, such as return time-based rainfall thresholds, or intensity-duration landslide triggering thresholds (Guzzetti et al., 2021; Peruccacci et al., 2011). Operational systems based on parameters other than rainfall are rare. The operational simplicity of these

systems, however, can cause problems to Civil Protection duties. Switching from probabilistic forecasts with strong uncertainty to a decision-making procedure based on discrete alert levels can generate "wear" following false alarms or missed alarms.

In this context, the Umbria civil protection authorities implement the regional LEWS. The threshold methodology relies on measured/forecasted rainfall parameters and a Soil Saturation Index (SSI). Recent literature increasingly reports the key influence of soil saturation as a parameter of primary importance in landslide triggering processes (Lazzari et al., 2018; Wiki et Al., 2020; Bezak et Al., 2021). The 24-hour rainfall parameter has a resolution of 1 km and is obtained through a merging procedure combining radar reflectivity and rain gauges (Sinclair and Pegram, 2005; Bruno et al., 2021). The calculation of SSI is based on distributed precipitation measurements and a soil water balance model (Brocca et al, 2010a, Silvestro et al., 2013; 2015) calibrated against experimental monitoring data (i.e., soil moisture probes network, river discharge, ASCAT satellite wetness index) as described by Brocca et al., 2010b. Our threshold-based methodology uses SSI to estimate the water content of the soil at the beginning of the landslide triggering rainfall. The SSI implicitly takes into account the pattern and space-time distribution over the territory of antecedent precipitation, simplifying the description of triggering rainfalls. Using information available on landslides inventories, Ponziani et al. (2012) studied the correlation between SSI and maximum cumulated rainfall values during landslide events. Results highlighted that the introduction the soil moisture index leads to an improvement in data dispersion, therefore to a lower uncertainty (i.e., lower false and missed alarms numbers).

Based on the comparison between predicted parameters with the first and second level alert thresholds, the operational Umbria LEWS issues daily bulletins describing the evolution of weather phenomena and associated landslide alert levels for a grid of 750 point distributed over the entire regional territory.

## 3. Materials and Methods

### 3.1 InSAR analysis and active landslide mapping

We use a traditional two-pass interferometry approach to process SAR images acquired by Copernicus Sentinel 1 A/B satellites. The Sentinel images are C-band images (5.6 cm radar wavelength) acquired every six days (interval between Sentinel 1A and Sentinel 1B).

Our analysis spans between October 2019 and January 2021 and considers two descending and two ascending orbit. We divided the relatively vast Umbria region (8456 $km^2$), in 7 sub-basins that were separately processed. Geocoding and interferogram processing is performed by means of GMTSAR InSAR package (Sandwell et al., 2011) while complex interferograms were unwrapped with SNAPHU (Chen et al., 2001). We produced 1120 interferograms with temporal baseline in the range 6 to 24 days.

The topographic phase was calculated and subtracted (e.g. Massonnet and Feigl, 1998; Bürgmann et al., 2000) by using an external digital elevation model (10 x 10 m up to elevation = 200 a.s.l. and SRTM above). Large scale atmospheric noises have been reduced by high pass filtering the interferograms and by selecting a stable

reference area: we typically chose geomorphological features (e.g. ridges) that are not involved in gravitational movements. Goldstein filters (Goldstein and Werner, 1998) have been applied to reduce residual noises and enhance the deformation signal.

We identified actively moving landslides by stacking interferograms and then crosschecking our results with the morphology of the slopes and with recent aerial photographs. Interferogram stacking improves the signal to noise ratio and highlights features moving at a rate sufficient to observe deformation in a short time span, yet slow enough to avoid loss in radar coherence. The interpretation of interferometric stacks led to the identification and mapping of InSAR deformation signals likely caused by landsliding, that we refer to as IDS, in the following.

In compiling our IDS inventory, we excluded signals extending across rivers or mountain crests, and, whenever we encountered dubious signals, we inspected single interferograms to check for possible residual topographic errors. Typically, our deformation signals show a sign inversion of the movements measured by the ascending and descending orbits, which is consistent with a downslope deformation, especially when the slope gradient is gentle and the along-slope displacement dominant. Similar approaches were used for areal investigation of active slope movements by other authors (Handwerger et al., 2015; Ciuffi et al., 2021; Tong and Schmidt, 2016).

### 3.2 Analysis of InSAR results: spatial distribution of InSAR deformation signals

We compared our IDS inventory to four simple geological and geomorphological control elements: bedrock lithology, slope gradient, exposure and landslide inventory. The aim is to detect significant correlation with each control element and, therefore, to improve our understanding of the spatial distribution of the signals over the territory. In order to do so, we adopted an established approach (Meyer et al., 2014, Regmi et al., 2010) to evaluate the topographical predictability of landslides. The technique is based on the theory of weights of evidence (WOE). WOE is a data-driven method (Bonham-Carter, 1994), which is basically the Bayesian approach in a log-linear form (Spiegelhalter, 1986) and uses prior (unconditional) probability and posterior (conditional) probability. In order to get more information about the analysis, there are papers available in the literature that explain the methodology in detail applied in different geological contexts such as Regmi et al., 2010 and Meyer et al., 2014.

The control elements and the classes used for the analysis are reported in Table 1. The classes of bedrock lithology are obtained by grouping Geological Formations (Pialli et al., 2009) based on their age and expected geomechanical behaviour. The landslide inventory control element considers the presence of a mapped landslide in the national inventory and its inferred state of activity (IFFI, Trigila et al., 2010).

The rasters of the 4 control elements were intersected with the deformation signal inventory. For each class $j$ of the control elements $V_i$ (with $j$ = 1...n), we evaluated the number of cells corresponding to the four possible combinations (Table 2). The values are used as input data for the computation of the Contrast (C): a statistical

parameter that expresses the degree of correlation between a given factor (the class of a control element, $V_{i,j}$) and the dependent variable (in our case the deformation signals).

| Control elements | Classes |
|---|---|
| Bedrock lithology | 1) Quaternary deposits<br>2) Carbonatic rocks<br>3) Plio-Pleistocene coarse deposits<br>4) Plio-Pleistocene fine deposits<br>5) Sandstone terrigenous deposits<br>6) Predominantly pelitic and/or chaotic terrigenous deposits |
| Landslide inventory | 1) No landslide<br>2) Relict landslide<br>3) Active landslide<br>4) Dormant landslide |
| Slope gradient | 7 classes of 5° width (2.5° to 37.5°) + 8$^{th}$ class for higher values |
| Aspect | 8 classes of 45° width |

*Table 1. Control elements and classes used for analysis.*

| | | Control elements ($V_{i,j}$) | |
|---|---|---|---|
| | | Present (1) | Absent (0) |
| **Deformation signal** | Present (1) | $N_{pix1}$ | $N_{pix2}$ |
| | Absent (0) | $N_{pix3}$ | $N_{pix4}$ |

*Table 2. Intersections performed between InSAR deformation signals and classes of control elements.*

The Contrast is obtained from the difference of the weights $W^+_{i,j}$ e $W^-_{i,j}$ :

$$C_{i,j} = W^+_{i,j} - W^-_{i,j} \quad [1]$$

where:

$$W^+_{i,j} = \log \{[N_{pix1}/(N_{pix1}+ N_{pix2})]/[(N_{pix3}/(N_{pix3}+ N_{pix4})]\}$$

$$W^-_{i,j} = \log \{[N_{pix2}/(N_{pix1}+ N_{pix2})]/[(N_{pix4}/(N_{pix3}+ N_{pix4})]\} \quad [2]$$

$W^+_{i,j}$ expresses the probability of finding a given class ($V_{i,j}$) in a deformation signal. Conversely, $W^-_{i,j}$ expresses the degree of anti-correlation of such class with the dependent variable. If the Contrast is positive ($C > 0$), the class of the control element is favourable for the development of a deformation signal; if the Contrast is negative ( $C < 0$ ), it is unfavourable.

In our case, when the value of Contrast is small, the significance of the correlation is uncertain because the deformation signals occupy a very small portion of the study area. Similarly, uncertainty can occur because a certain class of a given control element (e.g., carbonatic rocks of the bedrock lithology) is poorly represented in the considered territory. It is therefore inevitable that the Contrast is affected by an uncertainty that complicates its interpretation.

In order to get an estimate of the uncertainty associated to the Contrast, we use a bootstrapping technique consisting in the generation of N synthetic rasters of random polygons whose size and total area are similar to the InSAR-detected deformation signals. Each synthetic raster is then cross-referenced with the control

elements (Table 1) and Contrast is calculated (N values of the Contrast for each class of the control element, $V_{i,j}$). Finally, the standard deviation of the Contrast is calculated for each $V_{i,j}$. Such standard deviation represents the statistical variability of the Contrast that is used to describe the uncertainty associated to the Contrast calculated for the actual deformation signals. Whenever the Contrast, despite the associated uncertainty, is greater (or smaller) than zero, the control element is positively (or negatively) correlated to the presence of deformation signals. If the uncertainty band straddles zero, out data show no significant correlation.

### 3.3 Analysis of InSAR results: velocity time series of selected deformation signals

The aim of this analysis is to obtain velocity information for selected IDSs. 13 clearly recognizable and sustained deformation signals were selected, among those mapped in stacked interferograms, based on the visual inspection of 6-days single interferograms.

The maximum temporal resolution of InSAR-derived measures is 6 days (satellite revisit time), and we use 6-days interferograms to extract the displacement rates of the 13 selected IDSs. Depending on the geometry of the slope, we use interferograms derived from SAR images acquired in ascending or descending orbit. In order to compensate for the relative orientation of the slope and the line-of-sight (LOS), we convert LOS displacement in downslope displacement, by assuming that the movement is parallel to the slope (Hilley et al., 2004).

We use the $75^{th}$ percentile of the downslope displacement measured by single 6-days interferograms to estimate the velocity ($V_{75}$) of the selected deformation signals through time (Figure 2). Highly decorrelated interferograms were discarded based on visual inspection, and "no value" is assigned to the displacement rate of the corresponding period. Decorrelation may derive from very different conditions: large ground displacements (> 1/2 wavelength which corresponds to 2.8 cm approx., in case of C-band Sentinel 1 data), technical errors (i.e., orbital and DEM inaccuracies), reflective properties change (i.e., plowing of agricultural fields), and others (Wasowski and Bovenga, 2014). We refer to the resulting time series as InSAR-derived velocity time series ($V_{75}$TS). Given that numerical velocity values derived from interferograms can be affected by uncertainty (i.e., residual noise from topography, atmosphere, and temporal decorrelation), we combine velocities with the interpretation of the signal. More particularly, we introduce the binary classification of landslide activity based on a limit value of $V_{75}$. The value of the limit derives from the visual interpretation of the interferograms: it distinguishes "active state" (i.e., deformation signal clearly recognizable) and "inactive state" (i.e., deformation signal weak or absent). Examples will be presented in section 4.3. Based on the interpretation of the interferograms for each case analysed; the $V_{75}$ classification limit value varies between 30 mm/yr and 180 mm/yr for all selected cases. The use of different thresholds is required because the relative orientation of LOS and displacement vectors influences the numerical value of the displacement rate and because the dynamics of landslides is inherently different.

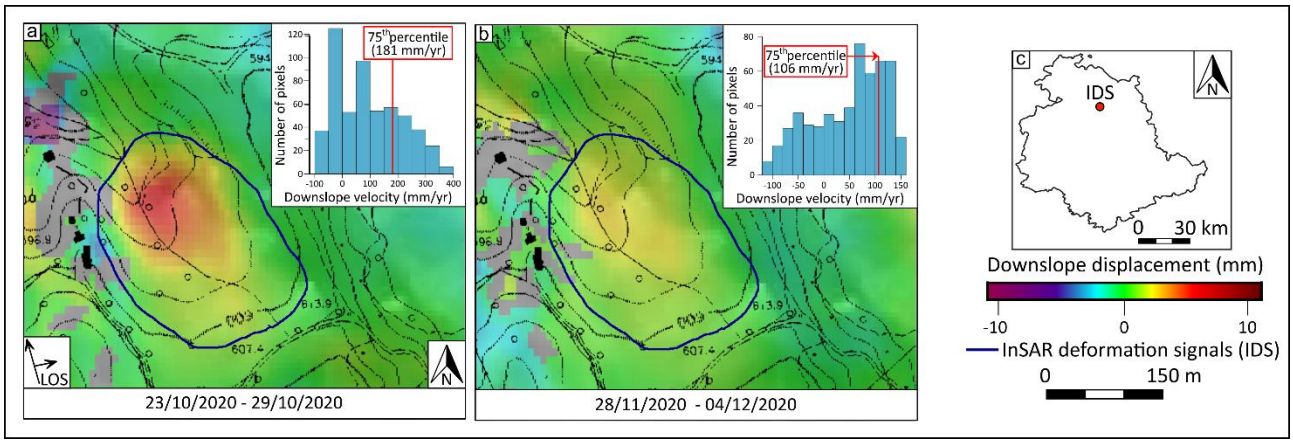


*Figure 2. 6-days interferograms describing the evolution of an example IDS. The IDS polygon is drawn based on stacked interferograms. Insets show the frequency distribution of the downslope-projected displacement rate inside the polygon. The displacement rate is evaluated in each interferogram by using the 75$^{th}$ percentile. Location of the example IDS on the regional territory shown on the right.*

### 3.5 Comparison between landslide velocities, rainfalls and soil saturation index.

InSAR-derived velocity information ($V_{75}$) have maximum nominal resolution of 6 days. Such information include some missing values. In fact, when highly decorrelated, interferograms are discarded and no velocity information is retrieved. The date of acquisition of the later SAR image, used to generate the 6-day interferogram, is assigned to available $V_{75}$ values.

Given rainfall measurement and soil saturation index have higher resolution than $V_{75}$, we need to downsample to allow comparison. First, we extracted 24-hours rainfalls and SSI into the nearest grid points to selected IDSs. Then, we selected the maximum 24-hours cumulated rainfall (max24rain) and the minimum soil saturation index (SSI) recorded during the corresponding $V_{75}$ time window (6 days). In case of rainfall events longer than 24 hours, only the highest value of rainfall cumulated over 24 hours is used together with SSI at the onset of the rain.

To take into consideration the possibility that the "active state" exhibited by a IDS (cfr. section 3.3) could be caused by rainfalls occurred before the beginning of the pertaining time window, we check the rainfall pattern of active IDSs associated to scarce or no rain (< 10 mm/24 h). If a larger rainfall episode is recorded in the previous time window, we consider such rainfall, and the corresponding preceding SSI, as associated to the landslide velocity information of the following time window.

Our methodology is designed to allow comparison between InSAR-derived landslide velocities and meteorological parameters used for territorial landslide early warning.

## 4. Results

### 4.1 Regional InSAR Analysis

We recognized active landslides by stacking interferograms (i.e., time-averaged deformation) over the entire investigation period (October 2019 to May 2020). Stacking enhances the signal-to-noise ratio and highlights features that are persistent in time and space.

Figure 3 shows two portions of the analyzed area where deformation signals are mapped based on the interferometric stacks. These latter show good coverage of the territory with decorrelated areas (i.e., grey areas in Figure 3) mostly located along steep, heavily vegetated slopes. InSAR deformation signals that we associate to active landslides are typically patches with relatively high LOS velocity and high standard deviation of LOS velocity. Furthermore, the comparative analysis of the interferometric stacks derived from the two orbits reveals that IDSs show very often the sign inversion of the displacement. The inversion is compatible with displacements whose horizontal component prevail over the vertical, such as sliding along a moderately inclined slope. We didn't find signal inversion in any other deformation signal except in landslides. Finally, we verified our IDSs with local morphology in aerial photographs and shaded relief map.

Overall, we identified 252 active landslides across the mainly hilly and mountainous territory of the Umbria region (Figure 4). The deformation signals have planform area ranging from 0.01 to 0.5 $km^2$ approx., with an average of 0.07 $km^2$. The majority of IDSs (166) are recognized in landslide deposits mapped by the Landslide Inventory (Trigila et al., 2010). In this case, they indicate the active state of the entire landslide or of a part of it. Otherwise, IDSs are located along slopes where landslide features are not recognized nor mapped, indicating either first-time impending slope failures or the reactivation of previously undetected landslides.

**4.2 Spatial distribution of InSAR deformation signals.**

The IDS inventory shows an uneven distribution over the territory. By comparing the spatial distribution of IDSs with four control elements (Table 1), we obtain an objective measure of their correlation. The results are expressed by the value of Contrast [1] in Figure 5. Contrast is calculated for each class of the control elements and the associated uncertainty estimated by means of a bootstrapping technique (section 3.2).

The results are coherent with the basic geological and geomorphological characteristics of the area.

The bedrock lithology has a strong influence on the distribution of active slope movements identified by IDSs. Pelitic/chaotic terrigenous deposits (class 6 in Figure 5a) is the type of substratum most favourable to their occurrence. In this case, the value of Contrast is highest, demonstrating the relative abundance of active slope movements along the slopes made of fine-grained weak rocks. Positive correlations are also found for recent, Pliocene-Pleistocene, fine deposits (class 4) and Sandstones (class 5). Significant negative correlation is obtained for classes 1 and 2, corresponding to quaternary deposits (class 1) and carbonate complexes (class 2). In this case, the values of Contrast capture the good stability conditions of the slopes made of carbonatic rocks and the low gradients of the slopes made of young sedimentary deposits.

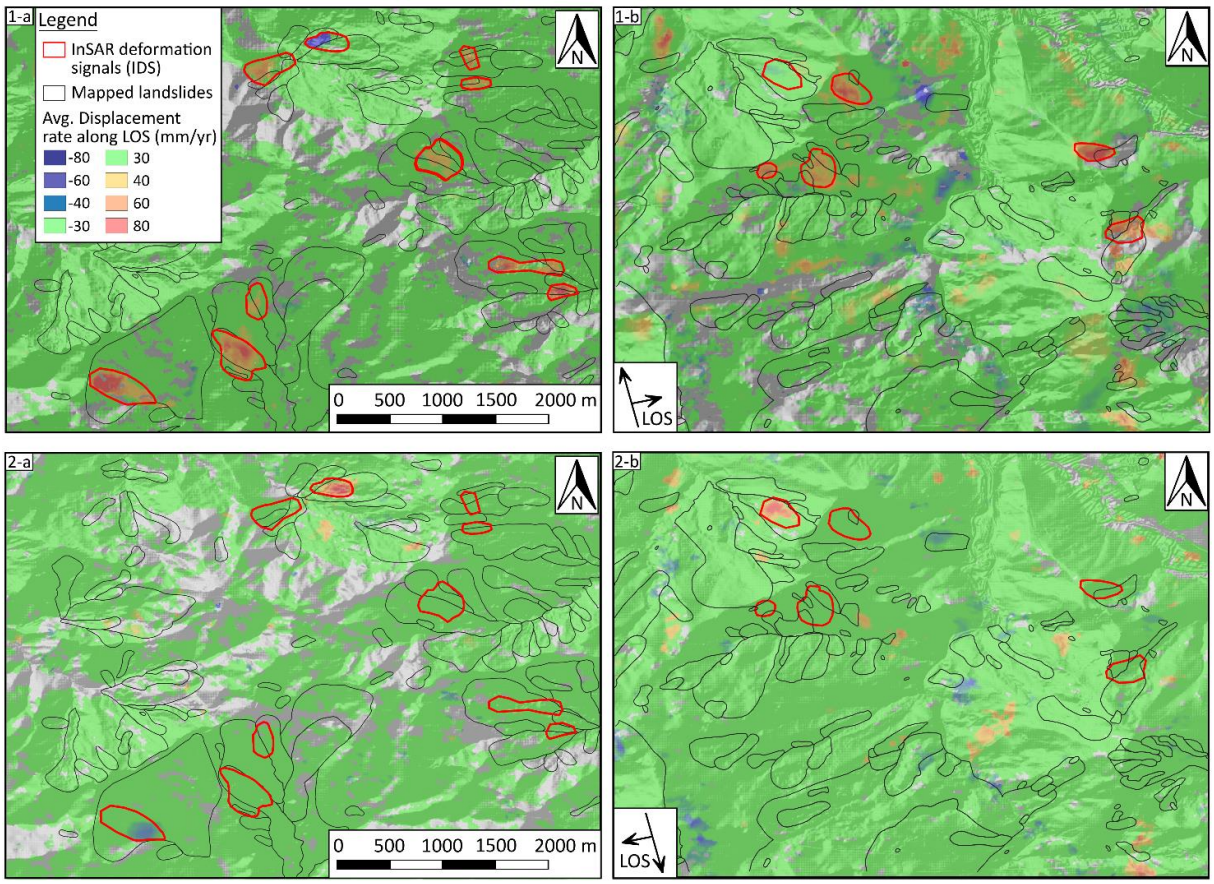


*Figure 3. Two example areas of the interferometric stack obtained in ascending (1a-b) and descending (2a-b) geometry for the Umbria region (see location in Figure 4) encompassing the period of analysis (01/10/2019 to 31/05/2020). Stacks are used for recognition and mapping of InSAR deformation signals. Displacement rates in the range -30 to +30 mm/yr are considered too low to be detectable by our analysis, therefore shown in green color.*

The aspect of the slope (Figure 5b) has a positive correlation mainly for slopes facing East while it is negative for the remaining classes. The trend of the Contrast values may indicate the conditioning of the geometry of SAR acquisition that makes displacements more problematic to measure when they occur along North or South facing slopes. In this cases, along-slope displacements have a smaller component of displacement along the satellite LOS compared to East and West facing slopes.

By comparing IDSs with the landslide inventory, we get positive correlation (C >> 0) with mapped landslides (Figure 5c), regardless of their inferred state of activity (active, quiescent, relict). The opposite is found for the slopes where landslide deposits are absent.

The spatial correlation with slope gradients (Figure 5d), indicates that the signals are more abundant along moderately steep slopes (7.5° to 17.5°) while the negative correlation becomes progressively stronger for higher gradients. The result is consistent with what we obtained for the bedrock lithologies since moderately steep slopes made of fine-grained weak rocks are the most susceptible to landsliding in Umbria.

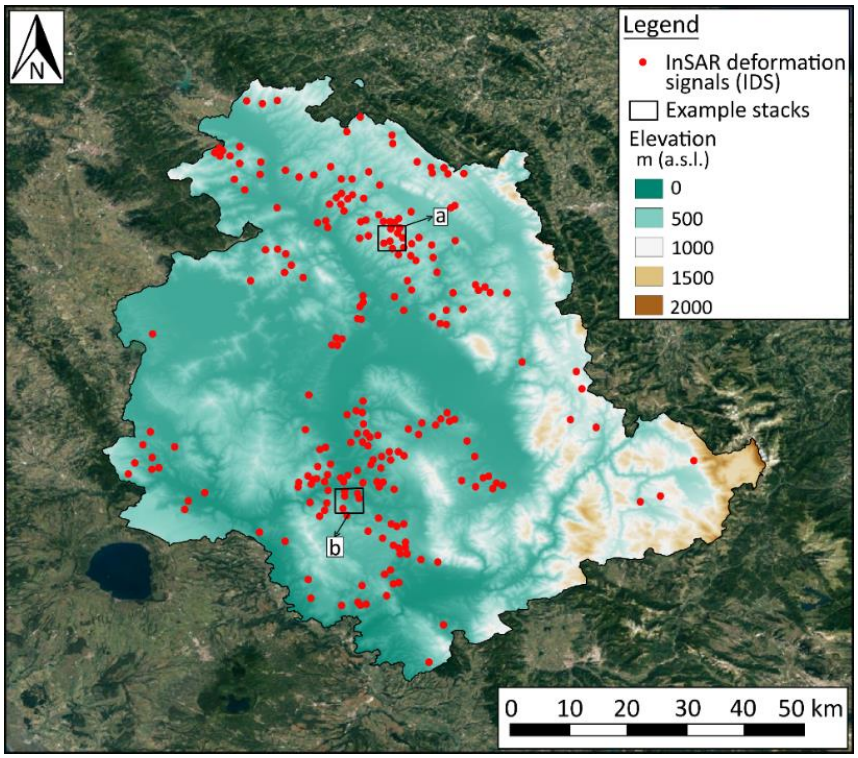


*Figure 4. Elevation map of Umbria and spatial distribution of InSAR deformation signals (IDSs) within Umbria region.*

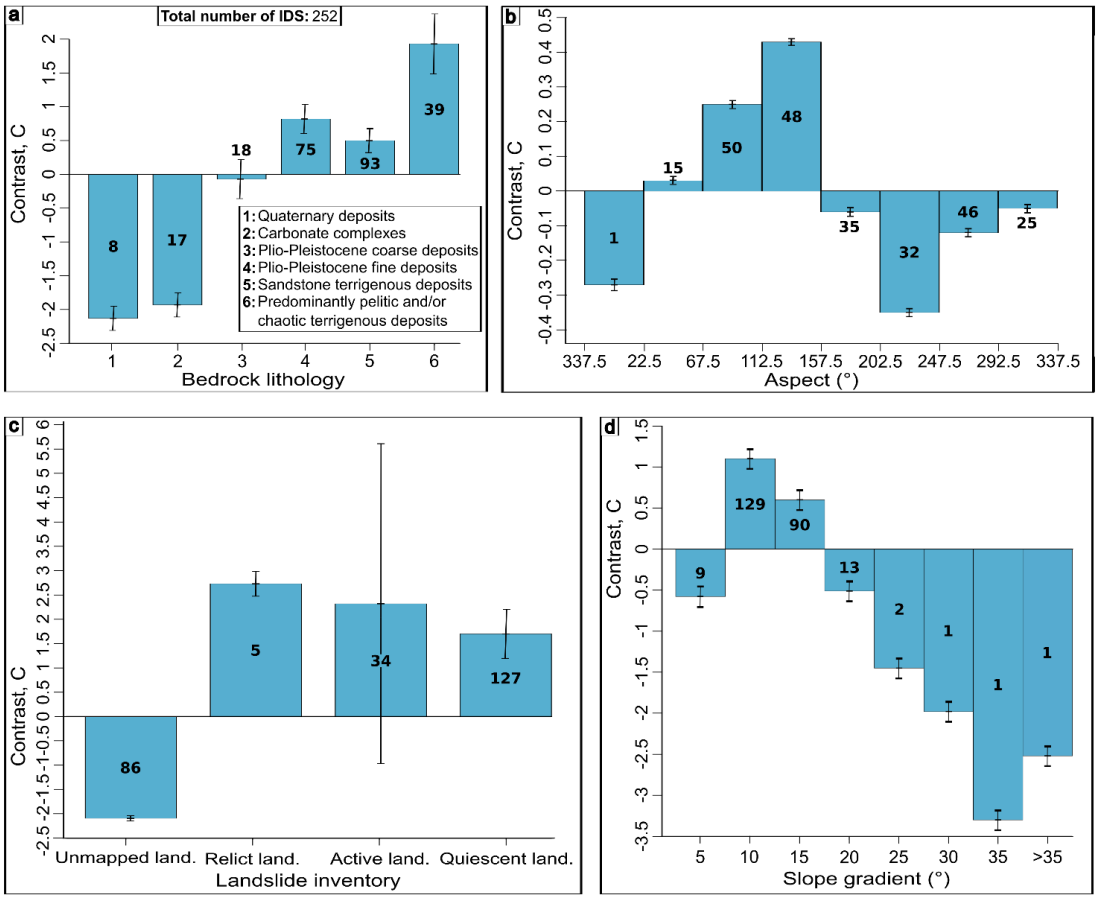


*Figure 5. Values of Contrast (C) obtained for the classes of the control elements. Positive values describe the spatial correlation between the class and IDSs. Error bars indicate the uncertainty associated to the correlation measure, numbers in the histograms indicate the abundance of InSAR deformation signals (IDS) for each class.*

### 4.3 Interferogram interpretation and evolution of IDSs through time: some examples

Although stacking interferograms proved very useful to recognize and map meaningful deformation signals, single interferograms potentially yield information about the evolution of the phenomena through time. Given they are also prone to include the effects of residual noise (Yunjun et al., 2019) and temporal decorrelation (Zebker and Villasenor, 1992), visual expert interpretation is required to extract relevant information (Manconi, 2021).

Here, we illustrate three examples of the 13 IDSs that we selected for time series retrieval. The scope is to give the reader a better idea of the information contained in single interferograms and associated uncertainties.

Example 1: Case Basse

The InSAR deformation signal of Case Basse do not correspond to a mapped landslide (IFFI, National Inventory of Landslides). The movement involves fine deposits of Plio-Pleistocene age along a gently dipping slope (9.2°) facing East. Interferometric results, shown in Figure 6, document slow movements peaking towards the end of the analysis period (December 2020) when our velocity estimates reach values of about 800 mm/yr. The velocity time series (Figure 6) show active state prevailing during the cold season (Figure 6b, c, e) and weak to absent deformation signal during summer (Figure 6a, d). The activity threshold is placed at 80 mm/yr (see section 3.3). During spring, there is a no-data period due to high decorrelation caused by rapid vegetation growth and/or by agricultural processing (temporal decorrelation). In all the interferograms, the highest deformation rates are located in the lower part of the slope (260 to 235 m a.s.l.).

Figure 7 shows the IDS draped over aerial photography and a UAV photo showing the irregular morphology of the landslide deposit, despite agricultural processing.

Example 2: Coldivecchio

Similarly to the first example, Coldivecchio is not mapped in the National Inventory of Landslide (IFFI). The slope movement involves Sandstone terrigenous deposits of Miocene age belonging to the Member of Galeata (Pialli et al., 2009) along a moderately dipping slope (9.3°) facing NW.

Interferograms (Figure 8) document high displacement rates at the end of the analysis period, during decembre 2020. The highest velocity of 560 mm/yr is recorded between December 4$^{th}$ and 10$^{th}$ and the corresponding interferogram is shown in Figure 8d. Interferograms "a", "b" and "e" are not plotted within the time series and this, because they record displacement values below our threshold of 80 mm/yr. The velocity time series (Figure 8) shows multiple stages of slope movement activity, separated by relatively long stages of little or no movement (inactive state). During the spring-summer period, between April and September 2020, highly decorrelated interferograms do not allow for a meaningful estimate of the displacement rate at Coldivecchio, likely due to rapid vegetation growth and agricultural practices. Also, in this case, the NW exposure of the slope is not favourable to InSAR, especially in descending orbit.

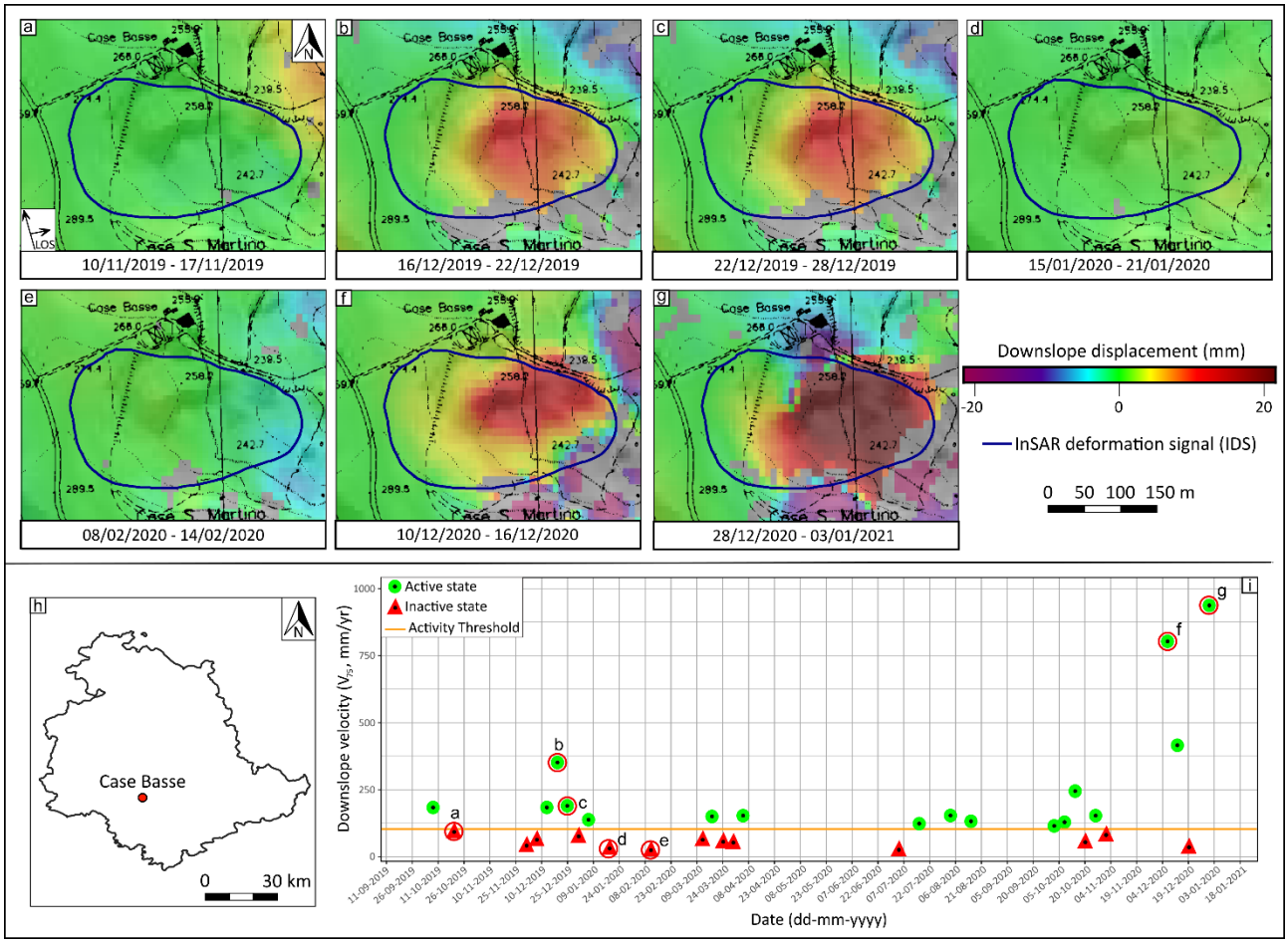


*Figure 6. Example interferograms obtained for the Case Basse IDS illustrating different states of activity (a-g). Velocity time series (i) reports $V_{75}$ obtained from interferograms. Symbols with labels refer to the example interferograms. Location of the landslide on the regional territory shown at the bottom left (h).*

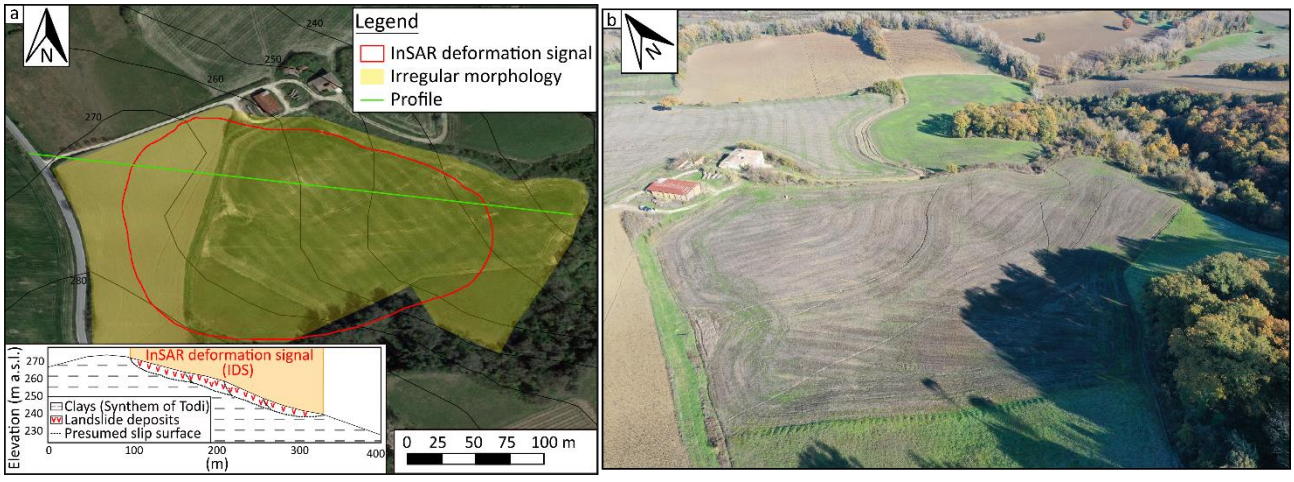


*Figure 7. UAV (Unmanned Aerial Vehicle) photograph of the "Case Basse" slope. Within the cultivated field in the centre of the photo, the irregular morphology of the slope and the presence of a surface water network are recognizable.*

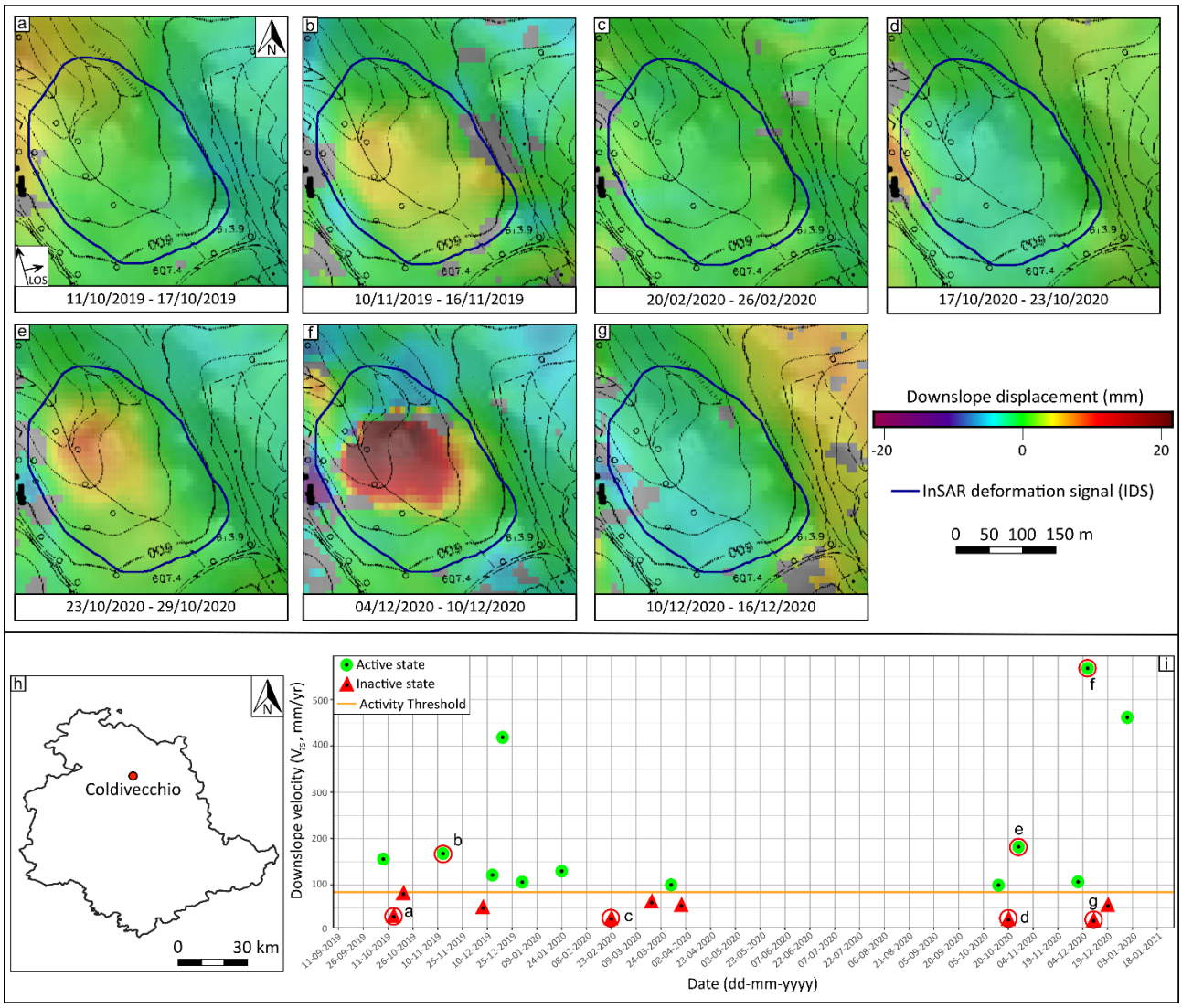


*Figure 8. Example interferograms obtained for the Coldivecchio IDS illustrating different evolution states of activity (a-g). Velocity time series (i) reports $V_{75}$ obtained from interferograms. Symbols with labels refer to the example interferograms. Location of the landslide on the regional territory shown at the bottom left (h).*

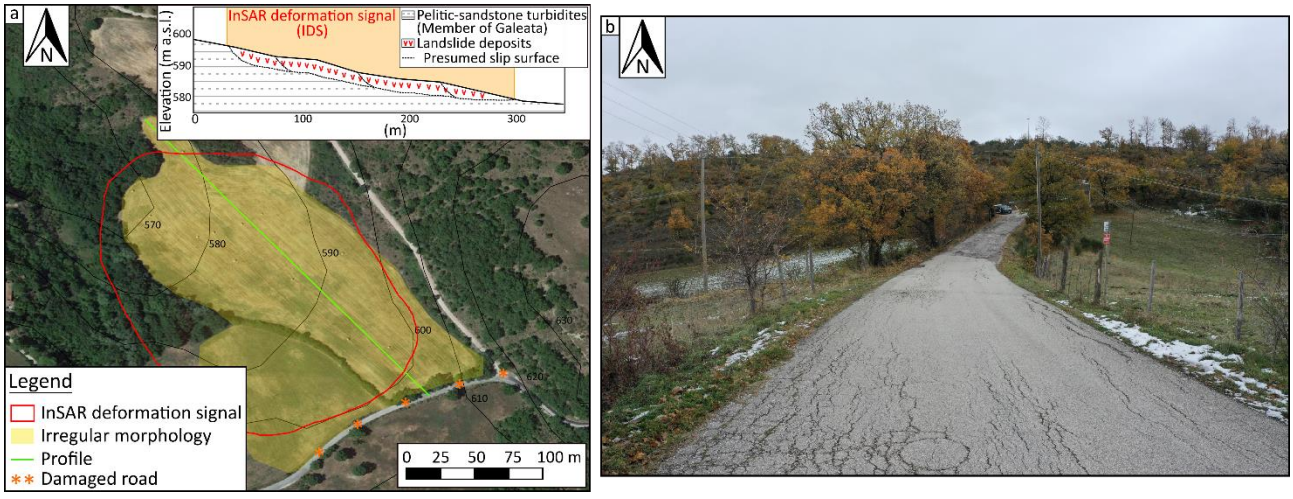


*Figure 9. Detail of undulating and cracked road for the case study "Coldivecchio". The deformed road shown is the one recognizable within Figure BB, within the series of interferograms, located at higher elevations (approximately 608 m a.s.l.).*

During the active state, higher velocities are recorded at lower elevations but deformations involve the whole IDS. Field surveys identified the landslide-related irregular morphology of the slope (Figure 9) and demonstrated that the road running in the crown area is also interested by notable deformation (Figure 9b).

Example 3: Montanaldo

The landslide of "Montanaldo" is mapped in the National Inventory of Landslide Phenomena (IFFI). It involves pelitic and/or chaotic terrigenous deposits belonging to the Olistostromes of the Galeata member (Pialli, 2009), of Miocene age. The average slope and aspect are 8.5° and 278°, respectively. By comparing the IDS (Figure 10) with the mapped landslide (IFFI landslide), Figure 11 shows how the deformation signal is located in the lower portion of the mapped landslide, extending beyond its lateral margins and toe.

The Montanaldo IDS shows velocities peaking in the cold season with maximum values at the end of 2020. Example interferograms (Figure 10) show very variable displacement rates at Montanaldo with peak values of about 800 mm/yr at the end of 2020 (Figure CCe). The slope movements at Montanaldo are generally sustained with occasional above-threshold deformations also during spring and summer. In this case, some good quality interferograms allow for velocity estimates also during the spring-summer period, possibly due to the favourable W orientation of the slope and/or type of crop and agricultural practices.

The area characterized by more intense deformations, in this case, is the one located at lower elevations, but evidence of deformations is not lacking even in the upper part of the slope. Figure 11 shows the extent of the mapped landslide and of the IDS; the UAV photo captures irregular morphology with frequent local counter slopes. In addition, in this case, agricultural practices erase other morphological evidences of movement such as small scarps and fractures.

For all three case studies shown within this section, and all the remaining 10 selected IDSs, the field evidence of deformation is rarely evident given the most common land use is agricultural. However, upon site inspection, we invariably found features, such as irregular morphology with occasional counter slopes, water ponding and cracks along roads, which are compatible with ongoing deformations. The InSAR standard analysis produces good quality interferograms, especially during the cold season. The rapid growth of vegetation and the cultivation for agricultural purposes of the areas during the spring-summer season, typically deteriorate the quality of interferograms introducing significant decorrelation.

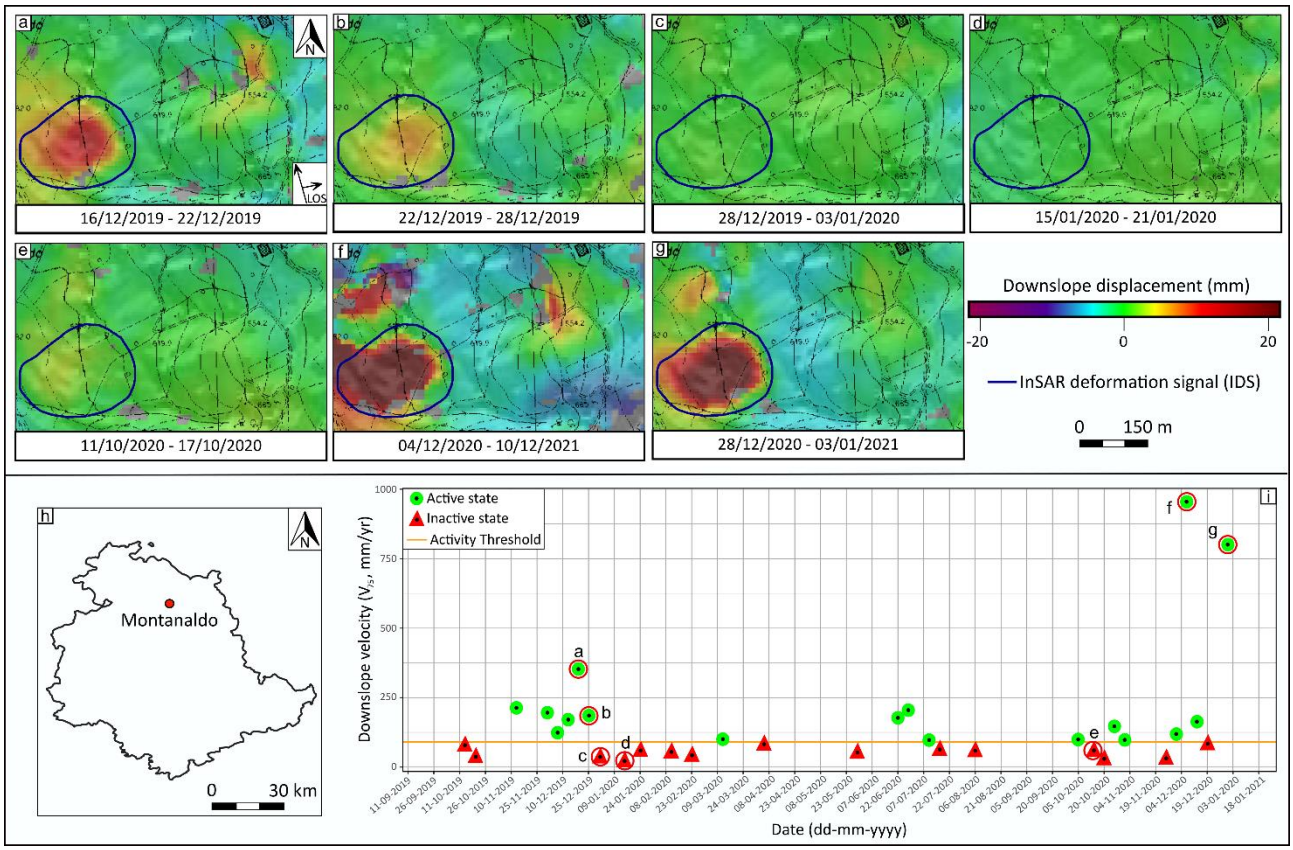


*Figure 10. Example of 6-day interferograms for the Montaldo IDS illustrating different states of activity (a-g). Velocity time series (i) reports $V_{75}$ obtained from interferograms. Symbols with labels refer to the example interferograms. Location of the landslide on the regional territory shown at the bottom left (h).*

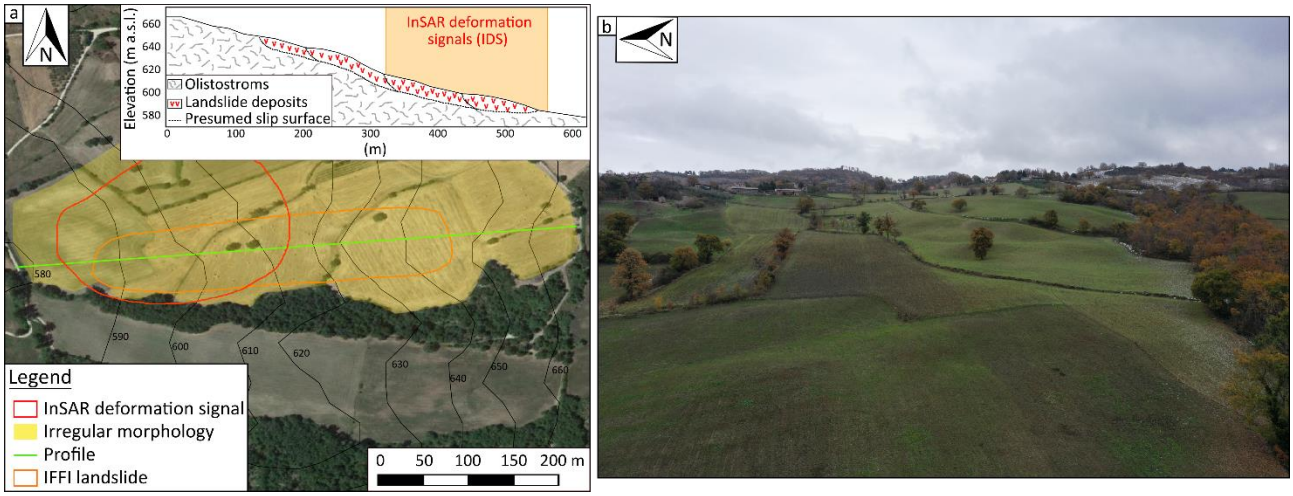


*Figure 11. Schematic map of the slope (left) with aerial photograph showing the perimeters of the mapped landslide and of the IDS. UAV (Unmanned Aerial Vehicle) photograph for the case study "Montanaldo" (right): although the slope is characterized by cultivated fields, the irregular morphology of the slope and the presence of reverse slopes is recognizable.*

### 4.4 Comparison of landslide velocity, 24-hours rainfall and soil moisture index

By visually inspecting interferograms, we gain the perception that major rainfall events cause the velocities of IDSs to increase. More particularly, multiple IDSs show relatively high velocities following significant rainfall events that hit the area during the study period (October 2019 to January 2021). In order to verify our qualitative

observations, we average velocity time series ($V_{75}$TS) of 13 selected IDSs and compare them to corresponding averaged values of rainfalls and SSI in Figure 12. The following observations can be done:

- During October 2019, averaged $V_{75}$ are lower than 200 mm/yr in association to moderate SSI values and no relevant rainfalls.
- During November 2019, rainfalls cause the increase of SSI and available velocities show some increase despite decorrelation problems limiting their retrieval.
- In mid-December, heavy rainfalls and high SSI values are associated with averaged $V_{75}$ of about 300 mm/yr and clearly visible displacements signals in many cases.
- During January and February 2020, very scarce precipitation is associated to a decrease of averaged velocities.
- At the beginning of March, the SSI is still relatively high and rainfalls cause a clear acceleration of IDSs, which translates into averaged $V_{75}$ increasing from 50 to 200 mm/yr approx.
- The spring and summer season record low precipitation values, decreasing SSI and highly decorrelated interferograms which translate into missing values of averaged velocities in Figure 12a. The effects of the rains occurred during the first half of June, therefore, cannot be evaluated.
- Finally, the two saturation and rainfall peaks of early and late December 2020 are well correlated with IDS acceleration in interferograms and averaged $V_{75}$ reaching peaks of about 500 mm/yr.

In Figure 13, we report climate-dependent parameters together with InSAR-derived velocities for the IDS of Case Basse, Coldivecchio and Montanaldo that were previously described (see section 4.3). Green circles correspond to active state of IDS deformation while magenta circles represent inactive state (see section 3.3). The diameter of green circles is proportional to the downslope velocity ($V_{75}$) of the IDS.

Active and inactive IDS states show a good degree of separation in the SSI – 24-hours rain space though there are some exceptions. In particular, some active signals plot in the lower part of the graph where *max24rain* is very low. This may happen when, following a reactivation, displacement rates slowly decrease over time before the mass stops (Cascini et al., 2014; Lacroix et al., 2020; Leroueil et al., 1996). The opposite is rarely seen and the upper right part of the chart is mainly populated by active states.

Given that SSI and max24rain are available for the same area and period of the InSAR analysis, we can compare the alert thresholds of the LEWS to all rainfall and soil conditions associated to remotely estimated state of activity of the selected slopes. Conceptually, such comparison allow evaluating the separation of climatic conditions that have and have not resulted in landslide activity (Berti et al., 2012), and check the position of alert thresholds in use for the regional LEWS in such context. Our comparison considers only 13 unstable slopes and a limited timespan; therefore, results intend to provide partial indications together with exploring the suitability of traditional two-pass interferometry for this purpose.

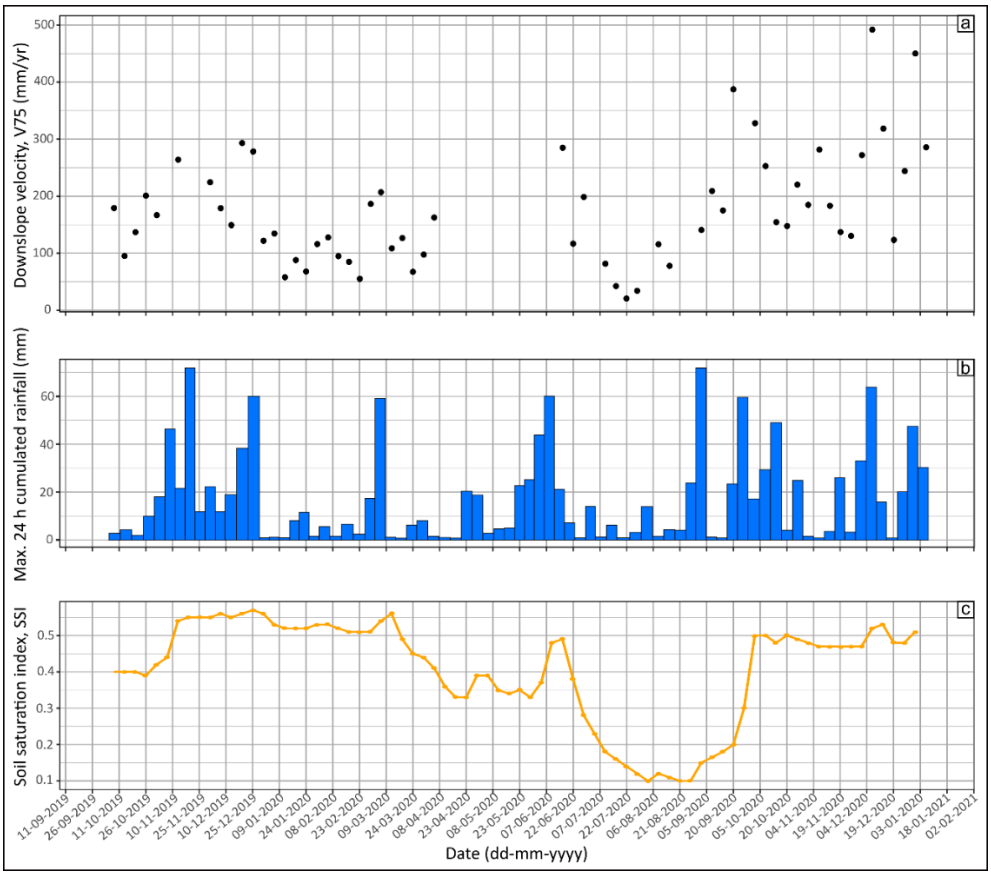


*Figure 12. Comparison between averaged values of IDS velocities, $V_{75}$ (a), 24-hour rainfall (b) and SSI (c).*

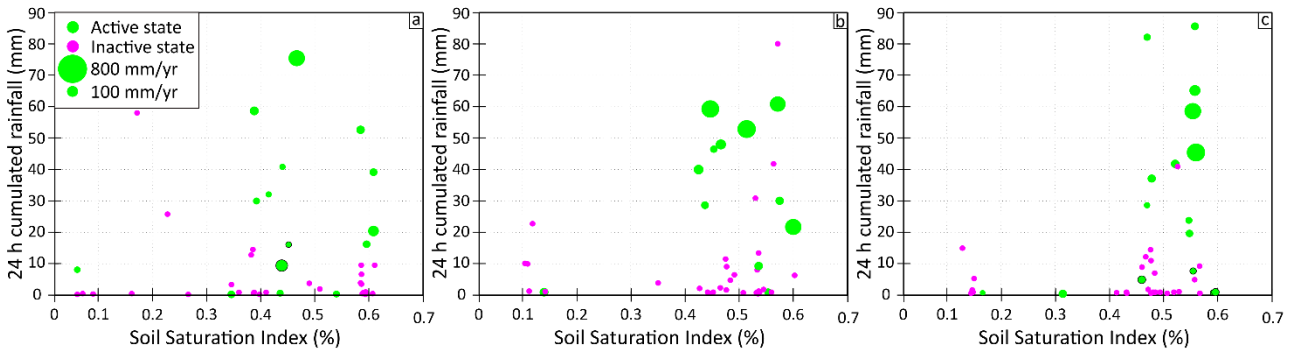


*Figure 13. Distribution of landslide activity states inferred from interferogram analysis in the SSI-max24rain space for the IDS of Case Basse, Coldivecchio e Montanaldo.*

The chart reported in Figure 14 reports available data for the 13 selected IDSs and the alert thresholds for comparison. The first level alert threshold is described by the following polynomial equation:

$$max24rain = 69.16 \cdot SSI^2 - 130.3 \cdot SSI + 78.21 \quad [1]$$

In general, the results confirms the good relationship between the InSAR-based landslide activity classification and the climatic parameters (*SSI-max24rain*) used in the Umbria LEWS (Figure 14a). The area of the chart pertaining to low values of soil saturation (SSI < 0.35 approx.) represents the late spring and summer seasons. Despite being scarcely populated due to frequent highly decorrelated interferograms, the majority of available

info indicate inactive states. The opposite is observed in the wet area of the chart where rainfalls operate some discrimination in relation to the velocity of IDSs.

The tools of binary classification metrics can be used to analyse the results of the comparison. Climatic parameters associated to active IDSs describe a true positive (tp) or a false negative (fn) case when above or below the *SSI-max24rain* threshold. In the case of inactive IDSs, they correspond to false positive (fp) cases when above the threshold and true negative (tn) cases, conversely. In the upper, above-threshold portion of the chart, the separation between inactive and active states is clear: only 14 interferograms document inactive states (fp) compared to 90 indicating activity (tp). Below the alert threshold, the data describing active state of movement (i.e., the interferogram shows high displacement rates despite the climatic condition didn't exceed the alert threshold). Here, we find 112 interferograms that document active state (fn) compared to 255 inactive (tn). As aggregate measures of performance, here we use the accuracy (acc) which considers both positive and negative true predictions in relation to the total number of cases; the Jouden's J score or bookmaker informedness (bm) which uses true positive and true negative rates and the treat score (CSI) which favours true predictions (Table 3).

The 1$^{st}$ level landslide alert threshold is intended to predict the possibility of landslide occurrence/reactivation over a given territory. The occurrence of a landslide causes significant surface deformation, likely associated to visible damages. Our analysis implicitly assumes that landslide accelerations are triggered by climatic factors (Lacroix et al., 2020; Matsuura et al., 2008) and that increasing displacement rates may precede failure episodes (Carlà et al., 2017; Squarzoni et al., 2020; Scoppettuolo et al., 2020; Zhu et al., 2021). This way, interferometric results describing relatively low displacement rates (30 to 1000 mm/yr approx.) can be used as a proxy of increasing failure probability. In this framework, the choice of the $V_{75}$ limit value for landslide activity classification (see section 3.3) is crucial. In order to explore its role, we analyse the scenarios generated by using an increasing multiplier for the $V_{75}$ limits. Results are reported in Figure 14, in the SSI-max24rain space, and in Table 4 in terms of the corresponding binary metrics. The number of active cases reduces in favour of inactive ones, which translate in a decrease of tp and fn in favour of fp and tn. In terms of threshold performance, the sensitivity of the model [tp/(tp+fn)] increases while its precision [tp/(tp+fp)] decreases with aggregate measures describing such complex outcome. When both positive and negative predictions are considered, the performance increase (acc) or maintain stable (bm) while it decreases if only positive predictions are considered (CSI), due to drop in precision that is not balanced by the improved negative prediction (higher tn and lower fn).

The receiving operating characteristics (ROC) method (Swets, 1988) can be used to describe the performance of the SSI-max24rain threshold. For this purpose, we computed ROC curves and optimal skill scores by varying the c parameter (intercept) of equation [1] while keeping the other two parameters constant (a = 69.16, b = -130.3). ROC curves, optimal skill scores (Table 3) and associated intercept values were calculated for increasing multiplier of the $V_{75}$ classification limits (0.75 to 2). Results are reported in Figure 15 where it can be seen that higher multipliers improve accuracy (acc) and diminish the critical success index (CSI) indicating

that the prediction of true positive cases tends to worsen while true negative predictions improve. DIS and bm show little variations for the above reason. The single ROC curves are very similar each other as testified by AUC values (Area under the curve, aggregate measure of performance across all possible thresholds described by equation [1]) varying between 0.74 and 0.79. Based on our results, the selection of the optimal threshold (Guzzetti et al., 2020) separating climatic conditions that have and have not resulted in landslide activity is not straightforward. Different performance metrics can give different indication and any choice has to take into account the objectives of the threshold. In the following section, we are discussing this topic in more detail.

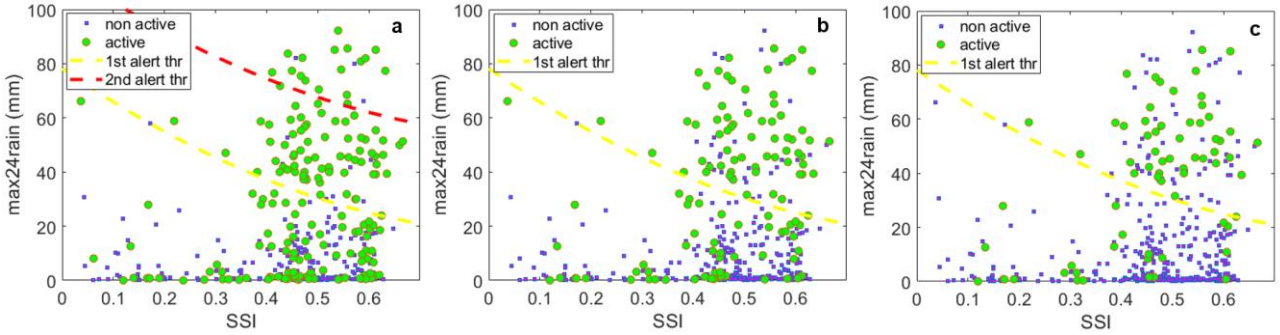


*Figure 14. Comparison between IDS state of activity and 1st level alert threshold (yellow) of the Umbria region. (a) state of activity derived from interpreted $V_{75}$ limit value. (b) 1.5x limit value (c) and 2x limit value.*

| Skill score | formula | range | optimal value |
|---|---|---|---|
| critical success index (threat score) | $CSI = \frac{tp}{tp + fn + fp}$ | 0-1 | 1 |
| Jouden's J (bookmaker informedness) | $bm = \frac{tp}{tp + fn} + \frac{tn}{tn + fp} - 1$ | -1-1 | 1 |
| accuracy | $acc = \frac{tp + tn}{tp + tn + fp + fn}$ | 0-1 | 1 |
| distance from the upper left corner of the ROC space | $DIS = \sqrt{\left(1 - \frac{tp}{tp + fn}\right)^2 + \left(\frac{fp}{fp + tn}\right)^2}$ | 0-1 | 0 |

*Table 3. Skill scores based on contingencies used to describe the performance of the 1st level alert threshold (tp, true positives; tn, true negative; fp, false positives; fn, false negatives).*

| $V_{75}$ limit value multiplier | tp | fp | tn | fn | threat score CSI | Jouden's J bm | accuracy acc |
|---|---|---|---|---|---|---|---|
| 1 | 98 | 14 | 249 | 90 | 0.485 | 0.468 | 0.769 |
| 1.5 | 72 | 40 | 286 | 53 | 0.4364 | 0.4533 | 0.7938 |
| 2 | 47 | 65 | 315 | 24 | 0.3456 | 0.491 | 0.803 |

*Table 4. Contingencies (tp, fp, tn, fn) and skill scores (CSI, bm, acc) for increasing V75 limit values used to classify active and inactive IDSs.*

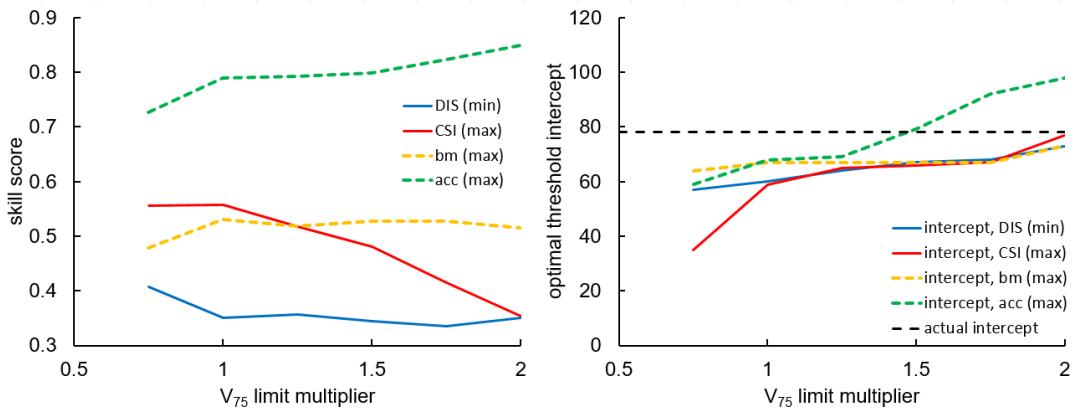


*Figure 15. Optimal skill scores as a function of the multiplier of the V75 classification limit (a) and associated intercepts of the 1st level alert threshold (b).*

The evolution of IDS deformation can be visualized by representing the state of activity and $V_{75}$ values for all selected IDSs through time (Figure 16). Here, we positioned the main 1st level (yellow) and 2nd level (orange) alerts occurred during the period of investigation. Both levels of alert are part of the same regional LEWS and describe a predictive scenario associated to an increasing number of landslides affecting the territory. Figure 16 allows appreciating when non-active landslides reactivate and when active landslides increase their displacement rate (or the opposite). From our point of view, the evolutionary trend of the unstable slopes is more important than the absolute value of the displacement rate. This latter varies depending on a variety of factors (e.g., type of movement and involved material, style of activity). Furthermore, it is estimated by differential interferometry that is one-dimensional by its own nature and gives results that are influenced by the relative orientation of the movement and the LOS.

During the first yellow alert event of November 2019, the scarcity of interferometric information due to widespread decorrelation (see section 3.1) partially hampers the comparison. However, three out of four available IDS are active. In the following, the number of reactivations/accelerations detected through InSAR during or shortly after the most severe yellow alerts and orange alerts declared by the Functional Centre can be considered as a useful experimental evidence validating the 2 alert thresholds used in the Umbria LEWS.

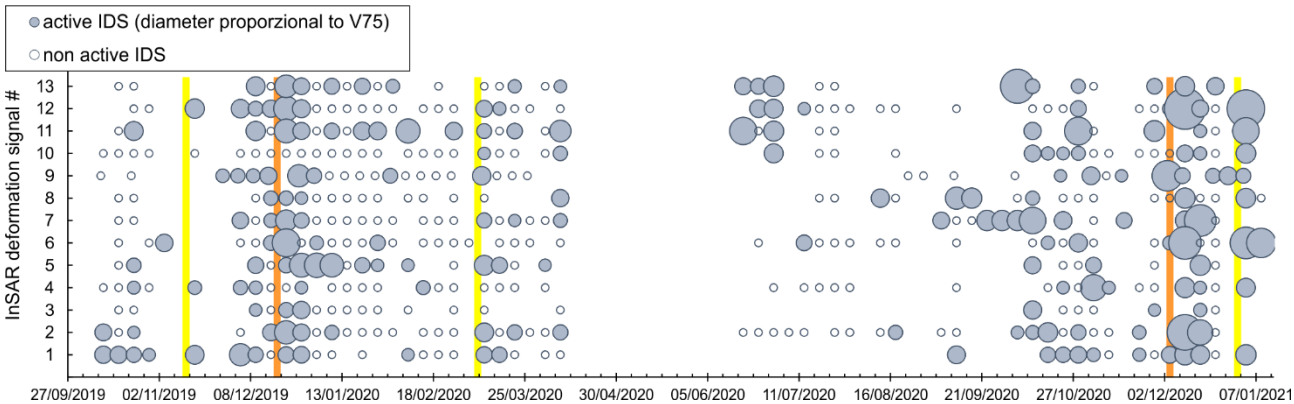


*Figure 16. Overall distribution over time of active (filled circles) and non active (empty circles) IDS compared to 1st and 2nd level landslide alerts (yellow and orange, respectively) issued by the Umbria region during the study period.*

## 5. Discussion and Conclusions

By using the conventional two-pass differential InSAR technique on the territory of the Umbria region, we detected 252 active landslides during the period between October 2019 and January 2021.

Our results show that interferometric stacking represents the most suitable tool for landslide detection and mapping in rural areas. As previously reported by other authors (Handwerger et al., 2015; Dini et al., 2019), it increases the signal-to-noise ratio and highlights features that are persistent in time and space. In the mountain territory of our study area (2480 $km^2$), dominated by low-gradient slopes, it produces quasi-continuous displacement maps which allow the detection of sustained slow movements over the territory. C-band interferometry, however, may result in poorer coverage of the territory where the terrain is steeper and/or heavily vegetated. We mostly used short temporal baseline IFs (6 to 24 days) to take full advantage of the short revisit time of the Sentinel 1 satellites. The use of short IFs substantially reduce decorrelation and help to get information not only for stable scatterers (i.e., buildings, unvegetated soil and rock outcrops) but also along moderately vegetated and cultivated slopes, that are most represented in the Umbria region. Short IFs also raise the range of measurable displacement rates in the order of tens to hundreds mm/yr which far exceed the velocities typically measured by multi-temporal InSAR (Solari et al., 2020). We cannot verify the completeness of our IDS inventory, given there is no comparable ground data, and it is possible that some slope movements went undetected. Similarly, we cannot exclude that a careful ground investigations may reveal that some IDS correspond to ground displacements not associated to landsliding. Unfavourable conditions are represented by movements of small extension (< 0.2 $km^2$ approx.), particularly steep slopes, slopes facing north or south and areas covered by dense vegetation.

By analysing our InSAR deformation signals (IDS) we find that they are numerically scarce when compared to mapped landslides (about 2%). Also, a significant number (86/252) is positioned along slopes where no landslide is mapped, indicating the potential of InSAR to identify slope deformations which may correspond to undetected landslides or incipient slope failures, thus complementing geomorphological observation for the compilation of landslide inventories. East and West slope exposures favour the detection of IDSs, due to the geometry of satellite observation. The majority of our IDSs are positioned along slopes made of fine-grained weak lithologies where slope gradients range between 7 and 17°, reflecting the landslide susceptibility of the territory. Field surveys confirmed that all the IDS identified are associated to ongoing slope movements. Agricultural practices often hide the evidence of deformation, but irregular morphologies including counter slopes, cracks and damages to the surrounding roads and local water ponding all confirm the remotely sensed information.

The analysis of stacked interferograms to detect and map active slope movements proved well suited for territorial management purposes. It shows good price – quality ratio, performs well in defining the geometry of landslides even in absence of PS, looks like an efficient way to update existing landslide inventories, and to obtain a valuable database, given the costs of field-based monitoring networks. However, unlike multi-temporal InSAR, the accuracy of displacement rates revealed by stacked interferograms is not comparable to

ground-based monitoring and the results should be given a qualitative meaning. Only the comparison with proper measurements can determine the level of accuracy which may vary depending on a number of factors (ground reflectivity, DEM precision, slope geometry, ...).

The visual inspection of single differential interferograms allow appreciating variable IDS displacement rates that can be used to monitor the state of activity of unstable slopes. We analyzed 6-days IFs, pertaining to 13 selected cases, to extract information about the temporal evolution of ongoing slope deformation. Not all IFs can be used due to decorrelation, and interpretation is required for appropriate selection. This need has obvious consequences on the possibility to apply automatic procedures but research efforts are starting to address similar problems (Fu et al., 2022). However, results are encouraging and selected IFs capture the main seasonal variation and the response to major rainfall episodes. The numerical description is entrusted to the 75$^{th}$ percentile of the downlope-projected InSAR-derived velocity within the IDS ($V_{75}$). Given we use C-band (5.6 cm wavelength) SAR images and 6-days IFs, we theoretically expect to measure displacements rates in the range 15 to 1500 mm/yr. Our $V_{75}$ vary between 30 mm/yr and 1000 mm/yr approximately. Signals below the lower limit cannot be clearly distinguished from stable slopes on 6-days IFs, therefore they are of no practical use.

We compared our results to the landslide early warning system (LEWS) operational in the Umbria region. The system relies upon 1$^{st}$ and 2$^{nd}$ level alert thresholds based on climatic parameters and describing the increasing possibility of having landslide phenomena in a given area of alert. In the case of geographical LEWS, the lack of accurate and reasonably complete information on where and when landslides occur limits greatly the ability to verify the forecasts quantitatively (Guzzetti et al., 2020). Remotely sensed data can help to address such issue (Mondini et al., 2021) and our comparison of two-pass differential interferometry results and alert thresholds aims to explore such possibility.

Our data indicate that the 1$^{st}$ level operational threshold of the Umbria geographical LEWS is capable of identifying the climatic conditions associated to landslide activity detected through InSAR. We do not expect that the comparison exhibit a perfect match because: i) the threshold aims at areal landslide prediction and ii) binary classification of active and non-active landslides through InSAR implies certain simplifications (see section 4). However, conventional binary classification metrics yield accuracy values (*acc*) of 0.77÷0.8 and Youden's indexes (*bm*) of 0.46÷0.49 (Table 4) that indicate the goodness of the threshold predictive performance.

The results indicate that conventional two-pass differential interferometry can provide useful information for geographical LEWS validation. They can effectively contribute to quantify the uncertainties associated to threshold models used for geographical LEWS that, otherwise, are rarely defined (Brunetti et al., 2010).

In the case of the Umbria region, the encouraging results obtained with a limited InSAR dataset indicate that, by increasing the number of InSAR deformation signals and the extension of the analysis period, the analysis is capable to detect and monitor the evolution of active gravitational slope movements over the regional territory.

Finally, thanks to the short revisit time of Sentinel 1 satellites, that we hope will soon be restored to its full 6-days potential, it is possible to imagine a joint use of differential interferogram analysis and geographical LEWS where cross-comparison may improve predictive capabilities.

**Acknowledgements:** Authors would like to thank 'Fondazione CIMA' for supplying climate parameters used in this work and for the scientific support. Authors would like to thank also Prof. Matteo Berti for the friendly and fruitful discussion on the results of the analysis and for the suggestions regarding the spatial statistics.

**Funding:** The InSAR analysis was commissioned by Regione Umbria to Fragile srl; the following research, including the analysis of InSAR results, did not receive any specific grant from funding agencies in the public, commercial, or not-for-profit sectors.

## References


Albano, M., Saroli, M., Montuori, A., Bignami, C.,Tolomei, C., Polcari, M., Pezzo, G., Moro, M., Atzori, S., Stramondo, S., Salvi, S., 2018. The Relationship between InSAR Coseismic Deformation and Earthquake-Induced Landslides Associated with the 2017 Mw 3.9 Ischia (Italy) Earthquake. Geosciences 2018, 8, 303. https://doi.org/10.3390/geosciences8080303

Apicella, L., Puca, S., Lagasio, M. et al., 2021. The predictive capacity of the high resolution weather research and forecasting model: a year-long verification over Italy. Bull. of Atmos. Sci.& Technol. 2, 3. https://doi.org/10.1007/s42865-021-00032-x

Batjes, N.H., Ribeiro, E., van Oostrum, A., 2020. Standardised soil profile data to support global mapping and modelling (WoSIS snapshot 2019), Earth Syst. Sci. Data, 12, 299–320. https://doi.org/10.5194/essd-12-299-2020

Bekaert, D.P.S., Handwerger, A.L., Agram, P., Kirschbaum, D.B., 2020. InSAR-based detection method for mapping and monitoring slow-moving landslides in remote regions with steep and mountainous terrain: An application to Nepal, Remote Sensing of Environment, Volume 249, 2020, 111983, ISSN 0034-4257, https://doi.org/10.1016/j.rse.2020.111983.

Berti, M., Martina, M.L.V., Franceschini, S., Pignone, S., Simoni, A., Pizziolo, M., 2012. Probabilistic rainfall thresholds for landslide occurrence using a Bayesian approach. J. Geophys. Res. 117, F04006. https://doi.org/10.1029/2012JF002367.

Bezak, N., Jemec Auflič, M., Mikoš, M., 2021. Reanalysis of Soil Moisture Used for Rainfall Thresholds for Rainfall-Induced Landslides: The Italian Case Study. Water 13, 1977. https://doi.org/10.3390/w13141977

Bonham-Carter, G.F., 1994. Geographic Information Systems for Geoscientists: Modeling with GIS. Pergamon Press, Canada.

Brocca, L., Barbetta, S., Melone, F., Moramarco, T., 2010a. A continuous rainfall–runoff model derived from investigations on a small experimental basin. IAHS Publ 336: 179–185.

Brocca, L., Melone, F., Moramarco, T., Wagner, W., Hasenauer, S. 2010b. ASCAT Soil Wetness Index validation through in-situ and modeled soil moisture data in central Italy. Remote Sens Environ 114, 11, 2745–2755.

Brunetti, M.T., Peruccacci, S., Rossi, M., Luciani, S., Valigi, D., Guzzetti, F., 2010. Rainfall thresholds for the possible occurrence of landslides in Italy. Nat. Hazards Earth Syst. Sci., 10, 447–458. www.nat-hazards-earth-syst-sci.net/10/447/2010/

Bruno, G., Pignone, F., Silvestro, F., Gabellani, S., Schiavi, F., Rebora, N., Giordano, P., Falzacappa, M., 2021. Performing Hydrological Monitoring at a National Scale by Exploiting Rain-Gauge and Radar Networks: The Italian Case. Atmosphere 12, 771. https:// doi.org/10.3390/atmos12060771

Bürgmann, R., Rosen, P.A., Fielding, E.J., 2000. Synthetic aperture radar interferometry to measure Earth's surface topography and its deformation. Annu. Rev. Earth Planet. Sci. 28, 169–209.

Carlà, T., Intrieri, E., Di Traglia, F., Nolesini, T., Gigli, G., Casagli, N., 2017. Guidelines on the use of inverse velocity method as a tool for setting alarm thresholds and forecasting landslides and structure collapses. Landslides, 14, 2, 517–534. https://doi.org/10.1007/s10346-016-0731-5

Cascini, L., Calvello, M., Grimaldi G.M., 2014. Displacement Trends of Slow-moving Landslides: Classification and Forecasting. J. Mt. Sci., 11, 3, 592-606. DOI: 10.1007/s11629-013-2961-5

Chae, B-J., Park, H-J., Catani, F., Simoni, A., Berti, M. (2017). Landslide prediction, monitoring and early warning: a concise review of state-of-the-art. Geosciences Journal 21, 6, 1033−1070. DOI: 10.1007/s12303-017-0034-4

Chen, C.W., Zebker, H.A., 2001. Two-dimensional phase unwrapping with use of statistical models for cost functions in nonlinear optimization. JOSA A 18, 338–351.

670 Ciuffi, P., Bayer, B., Berti, M., Franceschini, S., Simoni, A., 2021. Deformation Detection in Cyclic Landslides
671 Prior to Their Reactivation Using Two-Pass Satellite Interferometry. Applied Sciences 11, 3156.
672 https://doi.org/10.3390/app11073156

673 Cohen-Waeber, J., Bürgmann, R., Chaussard, E., Giannico, C., Ferretti A., 2018. Spatiotemporal patterns of
674 precipitation-modulated landslide deformation from independent component analysis of InSAR time series.
675 Geophys. Res. Lett. 45, 4, 1878–1887. doi: 10.1002/2017GL075950.

676 Dini, B., Manconi, A., Loew, S., 2019. Investigation of slope instabilities in NW Bhutan as derived from
677 systematic DInSAR analyses. Engineering Geology 259, 105111.

678 Dong, J., Zhang, L., Li, M., Yu, Y., Liao, M., Gong, J., Luo, H., 2018. Measuring precursory movements of
679 the recent Xinmo landslide in Mao County, China with Sentinel-1 and ALOS-2 PALSAR-2 datasets.
680 Landslides 15, 135-144. doi: 10.1007/s10346-017-0914-8.

681 Froude, M.J., Petley, D., 2018. Global fatal landslide occurrence from 2004 to 2016. Nat. Hazards Earth Syst.
682 Sci. 18, 8, 2161–2181. doi: 10.5194/nhess-18-2161-2018.

683 Fu L., Zhang Q., Wang T., Li W., Xu Q., Ge D., 2022. Detecting slow-moving landslides using InSAR phase-
684 gradient stacking and deep-learning network. Front. Environ. Sci. 10, 963322. doi: 10.3389/fenvs.2022.963322

685 Gariano, S.L., Guzzetti F., 2016. Landslides in a changing climate. Earth-Science Reviews. 162, 227-252.
686 http://dx.doi.org/10.1016/j.earscirev.2016.08.011

687 Glade, T., Crozier, M. J., 2005. The Nature of Landslide Hazard Impact. In: *Landslide Hazard and Risk*, John
688 Wiley & Sons Ltd, Chichester, England, 41–74, 2005.

689 Goldstein, R.M.,Werner, C.L., 1998. Radar interferogram filtering for geophysical applications. Geophys. Res.
690 Lett. 25, 4035–4038.

691 Guzzetti, F., 2000. Landslide fatalities and the evaluation of landslide risk in Italy, Engineering Geology 58,
692 2, 89-107. https://doi.org/10.1016/S0013-7952(00)00047-8.

693 Guzzetti, F., Gariano, S.L., Peruccacci, S., Brunetti, M.T., Marchesini, I., Rossi, M., Melillo, M. (2020)
694 Geographical landslide early warning systems. Earth-Sci Rev., 102973.

695 Guzzetti, F., Mondini, A.C., Cardinali, M., Fiorucci, F., Santangelo, M., Chang, K.T., 2012. Landslide
696 inventory maps: New tools for an old problem. Earth-Science Reviews, 112, 1-2, 42-66.

697 Guzzetti, F., Reichenbach, P., Cardinali, M., Ardizzone, F., Galli M., 2003. The impact of landslides in the
698 Umbria region, central Italy. Nat. Hazards Earth Syst. Sci., 3, 469–486. https://doi.org/10.5194/nhess-3-469-
699 2003, 2003

700 Hilley, G.E., Bürgmann, R., Ferretti, A., Novali, F., Rocca, F., 2004. Dynamics of slow-moving landslides
701 from permanent scatterer analysis. Science 304, 5679, 1952–1955.

702 Handwerger, A.L., Roering, J.J., Schmidt, D.A., 2013. Controls on the seasonal deformation of slow-moving
703 landslides. Earth Planet. Sci. Lett. 377, 239–247.

704 Handwerger, A.L., Roering, J.J., Schmidt, D.A., Rempel, A.W., 2015. Kinematics of earthflows in the northern
705 California coast ranges using satellite interferometry. Geomorphology 246, 321–333.

706 Hu, X., Bürgmann, R., Lu, Z., Handwerger, A.L., Wang, T., Miao, R., 2019. Mobility, Thickness, and
707 Hydraulic Diffusivity of the Slow- Moving Monroe Landslide in California Revealed by L- Band Satellite
708 Radar Interferometry. Journal of Geophysical Research: Solid Earth, 124, 7504–7518.

709 Hungr, O., Leroueil, S., Picarelli L., 2014. The Varnes classification of landslide types, an update. Landslides,
710 11, 167–194. doi: 10.1007/s10346-013-0436-y

711 Italian Civil Protection Department, CIMA Research Foundation., 2014. The Dewetra platform: a multi-
712 perspective architecture for risk management during emergencies. In: Hanachi, C. , Bénaben, F. and Charoy,
713 F. (Eds.) ISCRAM-med 2014, Toulouse. Lecture Notes in Business Information Processing, vol 196.

714 Information Systems for Crisis Response and Management in Mediterranean Countries. Cham: Springer.
715 https://doi.org/10.1007/978-3-319-11818-5_15.

716 Kishore, N., Marqués, D., Mahmud, A., Kiang, M., Rodriguez, I. et al., 2018. Mortality in Puerto Rico after
717 Hurricane Maria. New England Journal of Medicine 379, 2, 162-170. https://doi.org/10.1056/NEJMsa1803972

718 Lacroix, P., Handwerger, A.L., Bièvre, G., 2020. Life and death of slow-moving landslides. Nat. Rev. Earth
719 Environ.. 1, 404–419. https://doi.org/10.1038/s43017-020-0072-8

720 Lazzari, M., Piccarreta, M., Manfreda, S., 2018. The role of antecedent soil moisture conditions on rainfall-
721 triggered shallow landslides, Nat. Hazards Earth Syst. Sci. Discuss. [preprint], https://doi.org/10.5194/nhess-
722 2018-371, 2018.

723 Leroueil, S., Locat, J., Vaunat, J., Picarelli, L., Lee, H., Faure, R., 1996. Geotechnical characterization of slope
724 movements. In: Senneset K (ed), Landslides, Proceedings 7th International Symposium Landslides, Trondheim,
725 Norway, 17–21 June, 1, 53-74. Balkema, Rotterdam, The Netherlands.

726 Liang, C., Liu, Z., Fielding, E.J., Bürgmann, R., 2018. InSAR Time Series Analysis of L-Band Wide-Swath
727 SAR Data Acquired by ALOS-2. IEEE Trans. on Geosc. and Remote Sens. 56, 8, 4492-4506. AUGUST 2018

728 Manconi A., 2021. How phase aliasing limits systematic space-borne DInSAR monitoring and failure forecast
729 of alpine landslides. Engineering Geology, 287, 106094. https://doi.org/10.1016/j.enggeo.2021.106094

730 Mantovani, F., Soeters, R., Van Westen, C.J., 1996. Remote sensing techniques for landslide studies and
731 hazard zonation in Europe. Geomorphology 15, 213–225. https://doi.org/10.1016/0169-555X(95)00071-C

732 Massonnet, D., Feigl, K.L., 1998. Radar interferometry and its application to changes in the Earth's surface.
733 Rev. Geophys. 36, 441–500.

734 Matsuura, S., Asano, S., Okamoto, T., 2008. Relationship between rain and/or meltwater, pore-water pressure
735 and displacement of a reactivated landslide. Engineering Geology, 101, 49–59.

736 Meyer, N.K., Schwanghart, W., Korup, O., Romstad, B., Etzelmüller B., 2014. Estimating the topographic
737 predictability of debris flows, Geomorphology 207, 114-125. https://doi.org/10.1016/j.geomorph.2013.10.030

738 Mondini, A.C., Guzzetti, F., Chang, K-T., Monserrat, O., Martha, T.R., Manconi, A., 2021. Landslide failures
739 detection and mapping using Synthetic Aperture Radar: Past, present and future, Earth-Science Reviews, 216,
740 103574. https://doi.org/10.1016/j.earscirev.2021.103574.

741 Murray, K.D., Bekaert, D.P.S., Lohman, R.B., 2019. Tropospheric corrections for InSAR: Statistical
742 assessments and applications to the Central United States and Mexico. Remote Sensing of Environment 232,
743 111326.

744 Pagliara, P., Corina, A., Burastero, A., Campanella, P., Ferraris, L., Morando, M., Rebora, N., Versace, C.,
745 2011. Dewetra, coping with emergencies. Proc of the 8th Int. ISCRAM Conference – Lisbon, Portugal, May
746 2011, 5pp.

747 Peruccacci, S., Brunetti, M.T., Gariano, S.L., Melillo, M., Rossi, M., Guzzetti, F., 2017. Rainfall thresholds
748 for possible landslide occurrence in Italy. Geomorphology, 290, 39-57.
749 http://dx.doi.org/10.1016/j.geomorph.2017.03.031

750 Pialli, G., Plesi, G., Damiani, A. V., Brozzetti F., 2009. Note illustrative della Carta Geologica d'Italia alla
751 scala 1:50.000, Foglio N. 289 Città di Castello, Selca, Firenze.

752 Ponziani, F.; Pandolfo, C., Stelluti, M., Berni, N., Brocca, L., Moramarco, T. 2012. Assessment of rainfall
753 thresholds and soil moisture modeling for operational hydrogeological risk prevention in the Umbria region
754 (central Italy). Landslides, 9, 229–237.

755 Raspini, F., Bianchini, S., Ciampalini, A., Del Soldato, M., Montalti, R., Solari, L., Tofani, V., Casagli, N.,
756 2019. Persistent Scatterers continuous streaming for landslide monitoring and mapping: the case of the
757 Tuscany region (Italy). Landslides 16, 2033–2044.

Regmi, N.R., Giardino, J.R., Vitek J.D., 2010. Modeling susceptibility to landslides using the weight of evidence approach: Western Colorado, USA. Geomorphology 115, 1–2, 172-187. https://doi.org/10.1016/j.geomorph.2009.10.002.

Risse, L.M., Liu, B.Y., Nearing, M.A., 1995. Using Curve Numbers to determine baseline values of Green-Ampt effective hydraulic conductivities. J. of the American Water Res. Ass. 31, 147-159. https://doi.org/10.1111/j.1752-1688.1995.tb03371.x

Sandwell, D., Mellors, R., Tong, X., Wei, M., Wessel, P., 2011. Open radar interferometry software for mapping surface deformation. Eos, Transactions American Geophysical Union 92, 234.

Saulnier, G. M., Beven, K., and Obled, C., 1997. Including spatially variable effective soil depths in TOPMODEL, J. Hydrol. 202, 158–172.

Scoppettuolo, M. R., Cascini, L., Babilio, E. 2020. Typical displacement behaviours of slope movements. Landslides, 17, 1105–1116. DOI 10.1007/s10346-019-01327-z

Shi, X., Zhang, L., Zhong, Y., Zhang, L., Liao, M., 2020. Detection and Characterization of Active Slope Deformations with Sentinel-1 InSAR Analyses in the Southwest Area of Shanxi, China. Remote Sens. 12, 392. doi:10.3390/rs12030392

Silvestro, F., Gabellani, S., Delogu, F., Rudari, R., and Boni, G., 2013. Exploiting remote sensing land surface temperature in distributed hydrological modelling: the example of the Continuum model, Hydrol. Earth Syst. Sci., 17, 39–62. https://doi.org/10.5194/hess-17-39-2013, 2013

Silvestro, F., Gabellani, S., Rudari, R., Delogu, F., Laiolo, P., and Boni, G., 2015. Uncertainty reduction and parameter estimation of a distributed hydrological model with ground and remote-sensing data, Hydrol. Earth Syst. Sci. 19, 1727–1751. https://doi.org/10.5194/hess-19-1727-2015, 2015

Silvestro, F., Ercolani, G., Gabellani, S., Giordano, P., Falzacappa, M., 2021. Improving real-time operational streamflow simulations using discharge data to update state variables of a distributed hydrological model. Hydrology Research nh2021162. https://doi.org/10.2166/nh.2021.162

Solari, L. Del Soldato, R. Montalti, S. Bianchini, F. Raspini, P. Thuegaz, D. Bertolo, V. Tofani e N. Casagli, 2019. A Sentinel-1 based hot-spot analysis: landslide mapping in north-western Italy. Int. J. of Remote Sensing 40, 20, 7898-7921.

Solari, L., Bianchini, S., Franceschini, R., Barra, A., Monserrat O., Thuegaz, P., Bertolo, D., Crosetto, M., Catani F., 2020. Satellite interferometric data for landslide intensity evaluation in mountainous regions. Int J Appl Earth Obs Geoinformation 87, 102028.

Spiegelhalter, D.J., 1986. A statistical view of uncertainty in expert systems. In: Gale, W. (Ed.), Artificial Intelligence and Statistics. Addison-Wesley, Reading, MA, 17–55.

Tong, X., Schmidt, D., 2016. Active movement of the Cascade landslide complex in Washington from a coherence-based InSAR time series method. Remote Sensing of Environment 186, 405–415.

Trigila, A., Iadanza, C., Spizzichino, D., 2010. Quality assessment of the Italian Landslide Inventory using GIS processing. Landslides 7, 455–470. https://doi.org/10.1007/s10346-010-0213-0.

Wasowski J., Bovenga F., 2014. Investigating landslides and unstable slopes with satellite Multi Temporal Interferometry: Current issues and future perspectives. Eng. Geology 174, 103–138. https://doi.org/10.1016/j.enggeo.2014.03.003

Wicki, A., Lehmann, P., Hauck, C., Seneviratne, S. I., Waldner, P., Stähli, M., 2020. Assessing the potential of soil moisture measurements for regional landslide early warning. Landslides 17, 1881-1896. https://doi.org/10.1007/s10346-020-01400-y

Xie. M., Zhao, W., Ju, N., He, C., Huang, H., Cui, Q., 2020. Landslide evolution assessment based on InSAR and real-time monitoring of a large reactivated landslide, Wenchuan, China. Engineering Geology, 277, 105781. https://doi.org/10.1016/j.enggeo.2020.105781.

803 Xu, Y., Lu, Z., Schulz, W.H., Kim, J., 2020. Twelve- Year Dynamics and Rainfall Thresholds for Alternating
804 Creep and Rapid Movement of the Hooskanaden Landslide From Integrating InSAR, Pixel Offset Tracking,
805 and Borehole and Hydrological Measurements. Journal of Geophysical Research: Earth Surface, 125,
806 e2020JF005640. https://doi.org/10.1029/2020JF005640

807 Yunjun, Z., Fattahi, H., Amelung, F., 2019. Small baseline InSAR time series analysis: Unwrapping error
808 correction and noise reduction. Computers & Geosciences, 133, 104331.
809 https://doi.org/10.1016/j.cageo.2019.104331.

810 Zebker, H.A., Villasenor, J., 1992. Decorrelation in interferometric radar echoes. IEEE Trans. Geosci. Remote
811 Sens. 30, 950–959.

812 Zhang, YA., Meng, X., Jordan, C., Novellino, A., Dijkstra, T., Chen, G., 2018. Investigating slow-moving
813 landslides in the Zhouqu region of China using InSAR time series. Landslides 15, 1299–1315.

814 Zhang, Y., Meng, X.M., Dijkstrac, T.A., Jordan, C.G., Chen, G., Zeng, R.Q., Novellino, A., 2020. Forecasting
815 the magnitude of potential landslides based on InSAR techniques. Remote Sensing of Environment 241,
816 111738.

817 Zhao, C., Lu, Z., Zhang, Q., de La Fuente, J., 2012. Large-area landslide detection and monitoring with
818 ALOS/PALSAR imagery data over northern California and southern Oregon, USA. Remote Sensing of
819 Environment, 124, 348–359.

820 Zhu, Y., Qiu, H., Yang, D. et al., 2021. Pre- and post-failure spatiotemporal evolution of loess landslides: a
821 case study of the Jiangou landslide in Ledu, China. Landslides 18, 3475–3484. https://doi.org/10.1007/s10346-
822 021-01714-5

## 5. Paper 3

**Landslide deformation signals detected by InSAR at multiple temporal scales in a large basin of the Apennines***

Pierpaolo Ciuffi, Benedikt Bayer, Matteo Berti, Silvia Franceschini and Alessandro Simoni

* Submitted to **Geomorphology**

# InSAR stacking to detect active landslides and investigate their relation to rainfalls in the Northern Apennines of Italy.

Pierpaolo Ciuffi [(1)], Benedikt Bayer [(2)], Matteo Berti [(1)], Silvia Franceschini [(2)], Alessandro Simoni [(1)]*

(1) Department of Biological, Geological and Environmental Sciences (BiGeA), University of Bologna, Via Zamboni 67, 40126, Bologna, Italy;

(2) Fragile s.r.l., Viale Fanin 48, 40127 Bologna, Italy;

* Corresponding author: alessandro.simoni@unibo.it

**Abstract:**

Interferometric stacking is a useful technique to detect active slope deformation also over vast mountainous area. Compared to the analysis of single interferograms, the stacking approach improves the signal to noise ratio and deformation signals become clearer. In this work, we used stacked interferograms to detect active slow-moving landslides during the years 2015 to 2019 over a 1200 $km^2$ portion of the Northern Apennines of Italy. C-band Sentinel 1 SAR images were used to create short temporal baseline (6 to 24 days) interferograms which limit decorrelation and maximize the range of measurable displacement rates. Then we operated a further selection of interferograms based on coherence and visual inspection, before stacking over multiple time scales (1 month to years). The products of the analysis are ground displacement maps where the presence of residual noise is inversely proportional to the duration of the stack and the deformation signal is clearly recognized. Results show that only a small fraction of the mapped landslide deposits are experiencing deformation that can be detected by differential interferometry. In particular, we identified 118 InSAR deformation signals corresponding to ongoing gravitational slope deformations over the 9916 landslides mapped in the area. Active movements are mostly located on landslides that have undergone catastrophic reactivation in relatively recent times. Annual interferometric stacks proved better suited to detect active slope movements, while less than 15% of our deformation signals can be only be detected by inspecting monthly stacks. Active slow-moving landslides show variable displacement rates in monthly stacks. Periods of dormancy alternate to accelerations that may lead to actual catastrophic failures or, more often, determine finite periods of sustained slow movement before the displacement rates drop below the detection limit. We compared the evolutionary trends of the phenomena to the probability of landslide occurrence over the territory.

Results show that, at increasing landslide occurrence probabilities, an increasing fraction of actively deforming landslides can be detected by InSAR.

Keywords: InSAR, landslide recognition, landslide monitoring, rainfall threshold.

## *1. Introduction*

Landslides are common morphological features throughout the whole Northern Apennines chain. Following the classification of Cruden and Varnes (1996), most of the landslides mapped within the study area can be described as complex landslides, which combine roto-transitional landslides with earth flows (Simoni et al., 2013). Velocities can vary from millimeters to centimeters per year during the dormant phase (which can last from years to hundreds of years) to meters per hour during the failure (e.g., Bertello et al., 2018). Catastrophic failures typically occur after periods of high rainfall (Martelloni et al., 2012).

While antecedent rainfall appeared not important for landslide triggering itself (Berti et al., 2012), the relationship between displacement rate and rainfall seems to be affected by longer periods of preceding rainfall (Borgatti et al., 2006; Ronchetti et al., 2007). Moreover, surface deformation varies often for different areas of the landslide (Berti and Simoni, 2012) and the hydrological, hydrogeological conditions on a slope can be complex (Cervi et al., 2012). Anisotropy in primary conductivity, but also the presence and the formation of fissures and macropores on a landslide are difficult to assess on a slope scale, but may significantly influence infiltration, water flux, drainage and hence the build-up of pore pressure in the landslide body (Berti and Simoni, 2012). Therefore, a simple relationship between deformation and rainfall might not be apparent and the detection of this relationship requires displacement and rainfall measurements with high temporal acquisition frequency.

Most slope deformations occur on old landslide materials that failed in the past (Bertolini et al., 2004). In many cases, the reactivation of old deposits causes the regression of the main scarp and the physical degradation of the material which may move downwards as an earthflow. In other cases, the reactivation is more complex and different types of landslides can occur (Bertolini and Pellegrini, 2001). Monitoring landslide movements helps us better understand how the landslide mass propagates in space, how their motion evolves in time, and how external forcings, such as rainwater, control their behavior (Handwerger et al., 2019).

Conventional methods used for mapping and monitoring slope instabilities could benefit from remote sensing systems, which allow rapid and easily updatable acquisitions of data over wide areas, reducing fieldwork and costs (Ciuffi et al., 2021). A powerful technique for monitoring the displacements of large areas is the synthetic aperture radar interferometry (InSAR) that provides the possibility to measure the deformations of the landslide

deposits during the slow-motion stage (i.e., before the rapid acceleration). InSAR was applied in a landslide-prone area in the mid-1990s (Fruneau et al., 1996), but only in the 2000s it became a well-known technique for landslide monitoring.

InSAR techniques can be grouped in two main families: (i) standard InSAR methods that include classic two-pass interferometry and interferometric stacking (Dini et al., 2019; Handwerger et al., 2013; 2015) and (ii) multi-temporal methods that include the so-called Persistent Scatterer Interferometry (PSI) and Small Baseline Subsets (SBAS) methods (Raspini et al., 2019; Zhang et al., 2020). In general, multi-temporal methods allow obtaining better accuracy and precision for good quality reflectors (houses, infrastructures, rock outcrops) but standard InSAR yields a more continuous coverage of the territory also when sparse to medium vegetation cover is present. Archived and newly acquired SAR images can be interferometrically processed to extract displacement time series. These data can be used to determine the sensitivity of landslide motion to external factors such as seasonal precipitation and seismic shaking (Cohen-Waeber et al., 2018; Handwerger et al., 2015; Albano al., 2018) and may have a significant potential in detecting precursory deformation preceding catastrophic failures (Dong et al., 2018; Ciuffi et al., 2021).

This paper presents the results of a regional InSAR analysis performed by standard two-pass interferometry and C-band Sentinel 1 SAR images. The study area is represented by a 1200 $km^2$ portion of the Northern Apennines of Italy, and the analysis covers a period between April 2014 and December 2019. The main goal is to detect active slope movements and to investigate their evolution through time. In order to obtain a satisfactory territorial coverage also in rural areas, we use interferometric stacking. Different time scales (multi-year, annual, and monthly) are considered to gauge their effect on the detection of InSAR deformation signals (IDS). We use visual interpretation together with geological judgement to detect and map InSAR deformation signals that are likely expression of gravitational slope movements. Their spatial distribution is compared to local morphology, geology of the substratum, landslide inventory and historical information. We investigate the state of activity of the detected landslides in relation to rainfall parameters used to predict landslide occurrence on a territorial basis.

## ***2. Study Area***

The study area is located in the central sector of the Northern Apennines of Italy (Fig. 1), to the west of the city of Bologna (Emilia-Romagna region). Whitin the study area, a total of 9916 landslide deposits have been mapped by the local Geological Survey (R.E.R., 2022). Most of these landslides may periodically experience catastrophic failures (or reactivations) when displacement rates can climb up to m/day. Otherwise, they typically move at a rate of few centimeters to few tens of centimeters per year.

Chaotic clay-shales with block in matrix fabric (Pini, 1999; Vannucchi et al., 2003) and flysch deposits (Ricci Lucchi, 1986) are the most common lithologies in the study area (Fig. 1). Where clay shales outcrop, earthflows with distinct source, transport and deposition zones are the dominant type of slope failure (Simoni et al., 2013). Where the relief is made of pelitic flysch, a broader spectrum of landslide types can be observed, but often the failures have characteristics of translational or rotational earth- or rockslides in the upper portions of the landslide and may propagate as earthflow further down-slope (Borgatti et al., 2006; Corsini et al., 2006; Berti et al., 2017). Bertolini et al. (2004) conducted radiocarbon dating on tree logs, stumps and deposits of peat bogs that were buried inside landslide deposits of the Northern Apennines during catastrophic failures. They found ages ranging from the transition between Pleistocene and Holocene (ca. 13.759 years B.P.) and Medieval times (ca. 500 years B.P.), demonstrating the long-life cycle of these large landslides, subject to periodic reactivations and long periods of dormancy.

The Northern Apennines have a Mediterranean climate and total annual precipitation reaches on average 1300 to 1400 mm (Berti et al., 2012). The temporal pattern is characterized by intense rainfall in spring and autumn, separated by dry summers and winter months with moderate precipitation that in part occurs as snowfall (Tomozeiu et al., 2000; Pavan et al., 2008).

## ***3. Materials and Methods***

### ***3.1 InSAR analysis and detection of slope deformation signals***

Space-borne synthetic aperture radar interferometry (InSAR) is a remote sensing technique which exploits the phase difference between two radar images that were acquired over a given track of the earth surface by a satellite. Part of the phase difference is caused by the deformation of the targets inside a pixel with respect to the sensor (Massonnet and Feigl, 1998; Rosen et al., 2000; Bürgmann et al., 2000). The technique has been

111 widely used in different fields of geoscience to assess deformation processes. It provides a straightforward
112 way to measure deformation events that occurred in the past, which is why it has been successfully applied to
113 landsliding (Bianchini et al., 2013; Handwerger et al., 2013; Raspini et al., 2019, other citations).

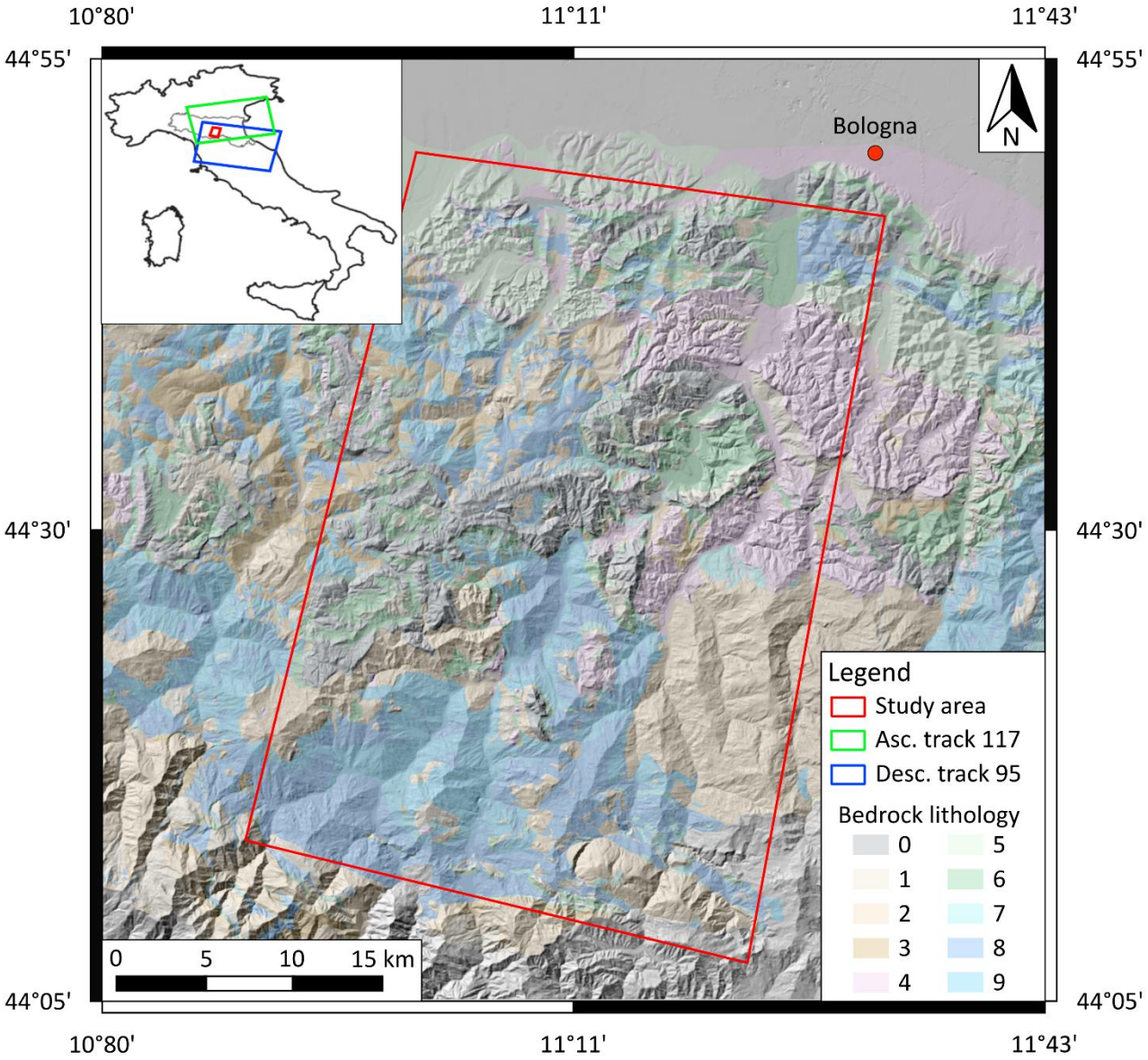


114

115 Figure 1 – Hillshade map of the study area and its location in the Italian peninsula (upper left inset). The bedrock lithologies
116 correspond to: 0: Stone rocks, 1: Stone/Pelitic alternation with S/P>3, 2: Stone/pelitic alternation with 0.3<S/P<3, 3: Lapid/pelitic
117 alternation with S/P<0.3, 4: Weakly cemented sands, 5: Consolidated clays, 6: Marls, 7: Olistostromic clays, 8: Tectonised clays and
118 argillites, 9: Palombini clays.

119 InSAR, however, presents three major limitations which are related to each other.

120 1. Phase ambiguity: The differential phase of an interferogram is measured as a fraction of the
121 wavelength, and a deformation field is mapped in the range between -π and π radians. At this point,

the phase is generally named wrapped phase, and in deforming areas, a spatial pattern called interferometric fringes can often be observed (e.g., Rosen et al., 2000). Switching from one end of the spectrum to the other is also commonly called phase-jump. Resolving this phase-ambiguity to obtain absolute values requires a process that is called phase unwrapping and can be solved numerically by different approaches (Chen et al., 2001; Hooper et al., 2007).

2. Decorrelation: Especially in rural or densely vegetated areas, decorrelation of the interferogram can happen (Zebker et al., 1992). It is mainly due to surface changes between two acquisitions (temporal decorrelation), which can result from high deformation rates, rapid vegetation growth, but also snow cover. Temporal decorrelation is more likely to occur in interferograms that span long periods. Decorrelation may also occur if the distance of the sensors between two acquisitions (known as perpendicular baseline) is large, which is called baseline decorrelation. If coherence is low, unwrapping will also be more problematic (Tarayre et al., 1996).
3. Phase noise: Even if the interferometric phase is coherent, it could contain unwanted residual noise due to the differential phase generated by DEM errors, atmospheric phase delay, and orbital inaccuracies (Tarayre et al., 1996; Zebker et al. 1997; Fattahi and Amelung, 2015, Xiao et al., 2022).

Several multi-temporal techniques, such as persistent scatterers interferometry (Hooper et al., 2004; Ferretti et al., 2001; Ferretti et al., 2011), small baseline techniques (Schmidt et al., 2003; Berardino et al., 2002), or mixed approaches (Hooper et al., 2008), were developed to address the problems of decorrelation and estimate different error terms of the phase. More recently, various authors (Squarzoni et al., 2020; Handwerger et al., 2015, 2019; Ciuffi et al., 2021) have shown that traditional two-pass interferometry can be successfully used to investigate gravitational slope movements thanks to shorter satellite revisit intervals and/or improved radar image quality.

In this work, we use standard two-pass interferometry to process SAR images acquired by Sentinel-1 A/B satellites. The Sentinel images are in C-band (5.6 cm radar wavelength), and they were acquired every twelve days between October 2014 and August 2016. Acquisition frequency increased to six days after the launch of Sentinel 1B Our analysis spans between April 2015 and December 2019 and considers one descending and one ascending orbit (Figure 1).

Interferogram processing was carried out by using GMTSAR software (Sandwell et al., 2011) while the interferograms were unwrapped with SNAPHU (Chen et al., 2001). We calculated and subtracted the topographic phase (e.g., Massonnet and Feigl, 1998; Bürgmann et al., 2000) by using an external digital elevation model (10 x 10 m cell size) and reduced large-scale atmospheric effects by filtering each interferogram with a high-pass filter. As stable references, we chose geomorphological features that are not affected by deformation processes, such as ridges.

Stacking interferograms improves the signal-to-noise ratio and highlights the deformation features of processes that move fast enough to observe deformation in a short period of time, but slow enough to avoid unresolvable phase jumps or decorrelation. In order to evaluate the efficiency of interferometric stacks for the mapping of active landslides for different timespans, we use three types of interferometric stacks: multi-years (covering the entire analysis period), annual and monthly. The temporal baselines of the interferograms included in the interferometric stacks vary from a minimum of 6 days to a maximum of 30 days.

The interpretation of interferometric stacks led to the identification and mapping of InSAR deformation signals that are caused by active landslides. Other authors have used similar approaches to recognize active deformation processes on a regional scale (Handwerger et al., 2015; Tong and Schmidt, 2016; Ciuffi et al., 2021). Our interpretation is mostly based on the local morphology described by the Digital Elevation Model (shaded relief map, slope map) and visible in aerial photographs. All IDSs are located along slopes where landslide morphology is clearly recognizable or, at least, where slope movements are coherent with the geomorphological context. An InSAR deformation signal was such when: 1) the signal does not cross a valley floor or a ridge; 2) the signal is clearly visible within the multi-year stack (in at least one orbit); 3) the signal is detectable within one (or more) annual stacks in at least one of the two orbits; 4) the signal is detectable within several monthly stacks (in at least one of the two orbits). These InSAR Deformation Signals will hereafter be referred to as IDS.

The IDSs that we associate with active slope movements are typically patches exhibiting relatively high LOS velocities and high standard deviation of LOS velocity. In addition, comparative analysis of the interferometric stacks derived from the two orbits reveals that IDSs very often show inversion of the sign of the LOS displacement. For instance, if a slope faces towards west, the deformation signal is registered as range decrease

in the ascending viewing geometry, while the descending orbit measures a range increase. The inversion is compatible with displacements whose horizontal component prevails over the vertical one, such as sliding down a moderately inclined slope. Figure 2 shows a conceptual slope in which a typical IDS is shown together with InSAR signals that cannot be interpreted as slope deformations, likely topographic artifacts (Massonet and Feigl, 1998) or the effect of changes occurred at the surface (Liu and Mason, 2017).

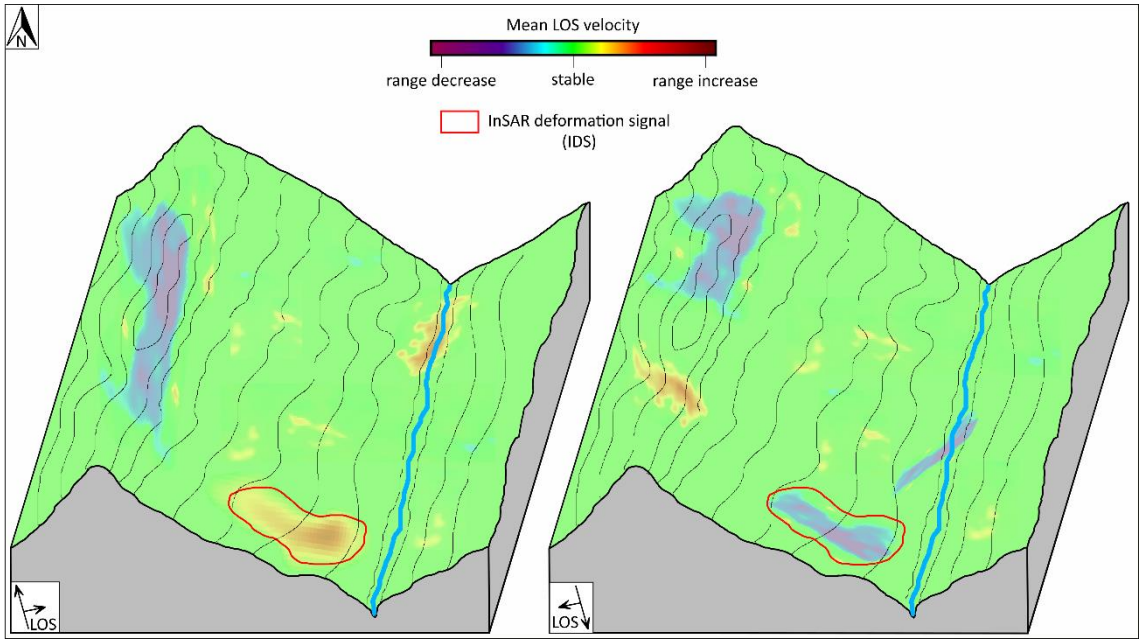


Figure 2 – Conceptual representation of a slope where an InSAR deformation signal (red polygon) is identified together with other signals likely attributable artifacts and/or noise of the interferometric data.

We classified the slope deformation signals depending on the interferometric stacks which led to their detection. The category "multi-years, annual and monthly" includes IDSs detected in multi-years, annual and one or more monthly stacks. The category "annual and monthly" includes signals recognized as active in at least one annual and one monthly stacks which are not visible in multi-year stack. Finally, the category 'monthly' includes IDSs with deformation signals visible only in one (or more) monthly stacks, but go undetected in annual and multi-year stacks. The choice of the above categories derives from the fact that all signals which recognized in multi-year stacks are visible also in one or more annual stacks. The same applies to annual signals which can be always recognized in one or more monthly stacks.

### *3.2 Spatial distribution of slope deformation signals*

The spatial distribution of IDSs was compared with the geological and geomorphological features of the territory in order to verify the mutual spatial relationship. In the following, such features are named control elements and include bedrock lithology, land use, slope gradient, slope exposure, quaternary deposit and time from last known landslide reactivation. The latter is based on the information reported by the regional inventory and historical archive of landslides that is regularly updated by the authority (R.E.R., 2022).

For this analysis we adopted a well-established technique (Meyer et al., 2014, Regmi et al., 2010) based on the theory of evidence weights (WOE) (Bonham-Carter, 1994). The WOE is a data-driven method (Bonham-Carter, 1994), which is basically the Bayesian approach in log-linear form (Spiegelhalter, 1986). The WOE uses the concept of prior (unconditional) and posterior (conditional) probability for assessing the relation between a target factor (in our case the IDSs) and several control elements spatially distributed in the area.

The control elements and the classes used for the analysis are reported in Table 1. Aspect and slope are derived from the 10 m cell-size Digital Elevation Model. The classes of bedrock lithology are obtained by grouping the geological formations (Panini et al., 2002) based on their age and expected geomechanical behavior. The Quaternary deposits include active landslides, dormant landslides and slope deposits. Active landslides are landslides that, at the time of the survey, showed evidence of movements on a geomorphological basis. Active landslides also include landslide deposits that at the time of the survey did not show definite signs of movement, but which nevertheless denoted recent activity signaled by evident clues (lesions to artefacts, absent or scarce vegetation, remobilized soil). Dormant landslides are gravitational deposits with no evidence of current or recent movements. They generally show a regular profile, a vegetation cover with a degree of development similar to that of the surrounding areas, and absence of recent damage to artefacts such as buildings or roads. Dormant landslides can be reactivated, since the preparatory and triggering causes that led to the failure are still present. Slope deposits are defined as deposits resulting from slope processes whose genetic attribution there remains a degree of uncertainty due to the lack of convincing evidence. Genesis may be gravitational, by surface runoff or by solifluction. Information on the timing and location of catastrophic failures of landslides (R.E.R., 2022) were used to derive the ‘time from last reactivation’ control element.

| Control elements | Classes |
|---|---|
| Aspect | *8 classes of 45° width* |
| Slope gradient | *5 classes of 5° width (0° to 25°)*<br>*+ 6th class for higher values* |
| Quaternary deposit | *1) No data*<br>*2) Slope deposits*<br>*3) Active landslides*<br>*4) Dormant landslides* |
| Time from last known landslide Reactivation | *0) No historical reactivation reported*<br>*1) Last reactivation: 1 to 30 years*<br>*2) Last reactivation: 31 to 60 years*<br>*3) Last reactivation: 61 to 90 years*<br>*4) Last reactivation: 91 to 120 years*<br>*5) Last reactivation: over 121 years*<br>*6) No data* |
| Land use | *0) Urbanized areas*<br>*1) Mining areas, quarries, landfills, artifact soils*<br>*2) Artificial green areas, parks*<br>*3) Agricultural land: arable land*<br>*4) Agricultural land: vineyards and orchards*<br>*5) Agricultural land: permanent meadows*<br>*6) Heterogeneous agricultural soils*<br>*7) Wooded areas*<br>*8) Shrub and/or herbaceous areas*<br>*9) Area with sparse or absent vegetation*<br>*10) Water environment: rivers, lakes* |
| Bedrock lithology | *0) Stone rocks*<br>*1) Stone/Pelitic alternation with S/P>3*<br>*2) Stone/Pelitic alternation with 0.3<S/P<3*<br>*3) Stone/Pelitic alternation with S/P<0.3*<br>*4) Weakly cemented sands*<br>*5) Consolidated clays*<br>*6) Marls*<br>*7) Olistostromic clays*<br>*8) Tectonized clays and argillites*<br>*9) Palombini clays* |

Table 1 - Control elements and classes used for the analysis.

The control element rasters were cross-referenced with the IDS inventory. For each class *j* of the control elements $V_i$ (with $j = 1...n$), we evaluated the number of cells corresponding to the four possible combinations of the confusion matrix (Table 2). The data are used as basic information for the determination Contrast (*C*). C is a statistical parameter that expresses the degree of correlation between a given factor (the class of a control element, $V_{i,j}$) and the dependent variable (in our case the IDSs).

The Contrast is obtained from the difference of the weights $W^+_{i,j}$ e $W^-_{i,j}$:

$$C_{i,j} = W^+_{i,j} + W^-_{i,j} \quad [1]$$

where:

$$W^+_{i,j} = \log \{[N\ pix1 / (N\ pix1 + N\ pix2)] / [N\ pix3 / (N\ pix3 + N\ pix4)]\}$$

$$W^{-}_{i,j} = \log \{[N\ pix2 / (N\ pix1 + N\ pix2)] / [N\ pix4 / (N\ pix3 + N\ pix4)]\} \quad [2]$$

$W^{+}_{i,j}$ expresses the probability of finding a specific class ($V_{i,j}$) in an IDS. In the other hand, $W^{-}_{i,j}$ expresses the degree of anticorrelation of that class with the dependent variable. If the value of C is positive (C > 0), the class of the control element is favorable to the development of an IDS; if, on the other hand, the value of C is negative (C < 0), it is unfavorable. When C is small, there is no statistical correlation between IDSs and the considered factor-class.

| | **Control element ($V_{i,j}$)** | |
|---|---|---|
| | Present (1) | Absent (0) |
| **IDS Present (1)** | $N_{pix1}$ | $N_{pix2}$ |
| **IDS Absent (0)** | $N_{pix3}$ | $N_{pix4}$ |

Table 2 - Intersections between InSAR deformation signals and classes of control elements.

Uncertainty has to be considered when interpreting C values. In general, we can say that the uncertainty increases when a certain factor-class occupies a small portion of the area. With the aim of estimating the uncertainty associated with C, we used a bootstrapping technique. This approach involves the generation of N synthetic rasters of random polygons whose size and total area are comparable to those of IDSs. Each synthetic raster is then intersected with control elements (Table 1) and the C values (N contrast values for each class of control element, $V_{i,j}$) are computed. The mean value and standard deviation of C is then calculated for each $V_{i,j}$. We adopt the standard deviation to describe the statistical variability and evaluate the uncertainty associated with C, calculated for mapped IDS. When C, considering the associated uncertainty, is greater (or less) than zero, the control element is positively (or negatively) correlated with the presence of IDS.

### ***3.3 Velocity time series of IDS***

To derive velocity information of all mapped IDSs we use monthly interferometric stacks. In general, when a landslide moves along the downslope direction and the horizontal component is larger than the vertical, the radar signal will show a range increase in one viewing geometry and, range decrease in the other. Theoretically, if the vertical component is relevant, the range may increase in both geometries, due to the lowering of the ground surface. This is rarely observed along the relatively gentle slopes of our study area. To limit complexity, we use the viewing geometry registering a range increase to extract the IDS velocities.

The LOS displacement rate of an IDS, in each monthly interferometric stack, is described by the pixel values in the IDS polygon. Their number is several hundred and their distribution typically shows a positive skewness, particularly when the signal is active (Figure 3). We use the 75$^{th}$ percentile of the LOS velocity values ($V_{75}$) as a descriptor of the landslide velocity because we are interested in the high values of the distribution describing the most active portions of the landslide. In fact, it can happen that only portions of the mapped signal move and that the rest are still, slower or affected by residual noise. When the decorrelation compromises our ability to recognize the signal, we assign 'no value' to $V_{75}$.

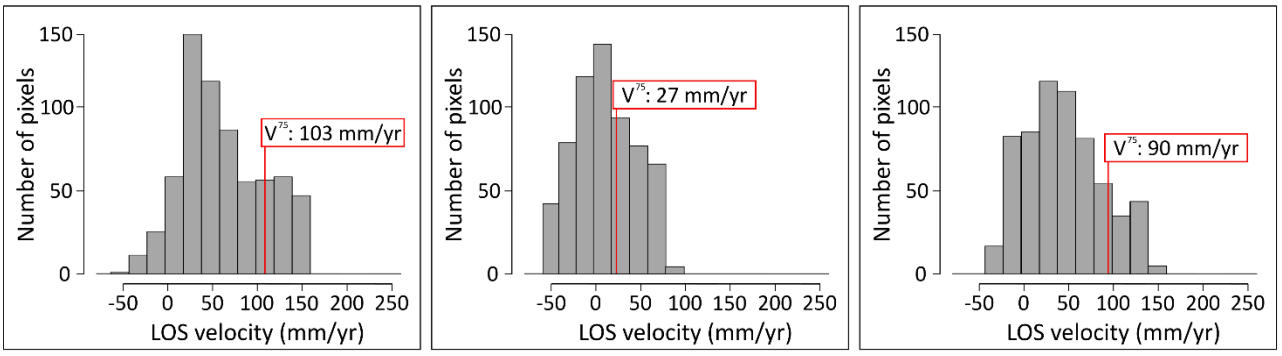


Figure 3 - Frequency histograms of LOS velocities from monthly stacks for IDS #6 (see Figure 13). In April 2018 (left) and February 2019 (right) the distributions and their $V_{75}$ values indicate that the landslide is actively moving. In January 2019 (middle), the landslide is dormant.

## ***3.4 Comparison between IDS velocities and rainfalls***

The comparison between InSAR-derived displacement rates and rainfall parameters necessarily requires some adjustments. We face problems that pertain to the low temporal of InSAR data, to the spatial variability of rainfalls and to the objective definition of rainfall event. Therefore, we use an approach based on the binary classification of both deformation signal velocities and rainfalls.

The binary classification of landslide activity is based on a limit value of $V_{75}$. Such value is derived from the visual interpretation of monthly interferometric stacks: it distinguishes the 'active state' (i.e. a clearly recognisable deformation signal) from the 'inactive state' (i.e. a weak or absent deformation signal).

Figure 4 shows a conceptual slope in which an IDS was recognized and illustrates how we classify its state of activity. Based on the interpretation of interferometric monthly stacks for each IDS, the $V_{75}$ limit value is set

at 55 mm/yr for all mapped IDSs. Given displacement velocity information obtained from stacked interferograms includes missing values, the binary time series of activity is not complete.

Figure 4 on the right shows the distribution of the velocity values of stable areas outside the IDSs and IDSs during inactive states. They also show the distribution of IDS velocities during active states. This difference in the distributions shows how the IDSs have a distinct 'footprint' with respect to the study area and justifies the identification of the activity threshold.

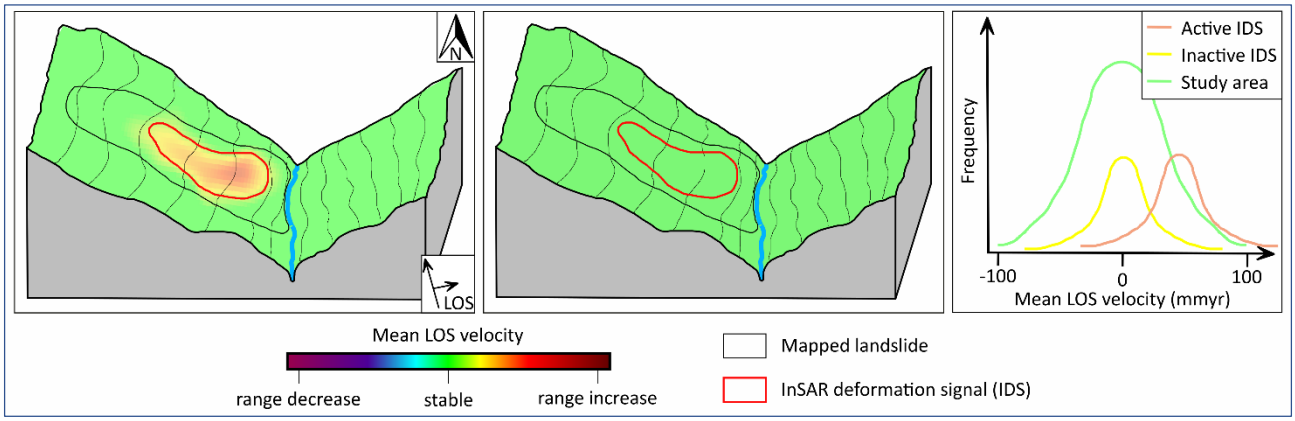


Figure 4 – Conceptual representation illustrating the binary classification of the IDS activity. The two sketches illustrate an active deformation stage (left) and a dormant stage (center). The graph on the right illustrate ideal distributions of LOS velocities derived from a monthly interferometric stack during the different stages.

Although there is general agreement on the importance of precipitations as landslide triggering factor (Guzzetti et al., 2020), the evaluation of the triggering rainfalls over a large territory can be very complicated, also given the possible role of antecedent rainfalls. For our analysis, we rely on the aggregated rainfall data that are used by the Emilia Romagna Region Civil Protection for their landslide early warning system. They are based on the measurements taken by tens of rain gauges within the so-called Alert Zones (Figure 5). In our case, the Alert Zones are two: area C1 covers the upper part of the area up to the main divide, area C2 covers the lower part and extends to the plain.

Since rainfall measurements are available at much higher resolution than InSAR-derived landslide activity information, it is necessary to downsample the data to allow comparison. To this purpose we used the rainfall thresholds defined by Berti et al. (2012) to predict the occurrence of landslides in the Emilia-Romagna region. The authors took advantage of the historical landslide archive, which includes more than 4000 events whose

296 date of occurrence is known, to investigate the relationship between landslides and rainfall parameters. They
297 showed that landslide probability increased with higher rainfall duration and intensity, and proposed rainfall
298 thresholds associated to increasing probability of landslide occurrence over a reference territorial unit (Alert
299 Zone). Hence, thresholds are lines of equal landslide probability in the rainfall duration-intensity chart.
300 Probability values refer to the entire Alert Zone, such as C1 and C2 (Figure 5).

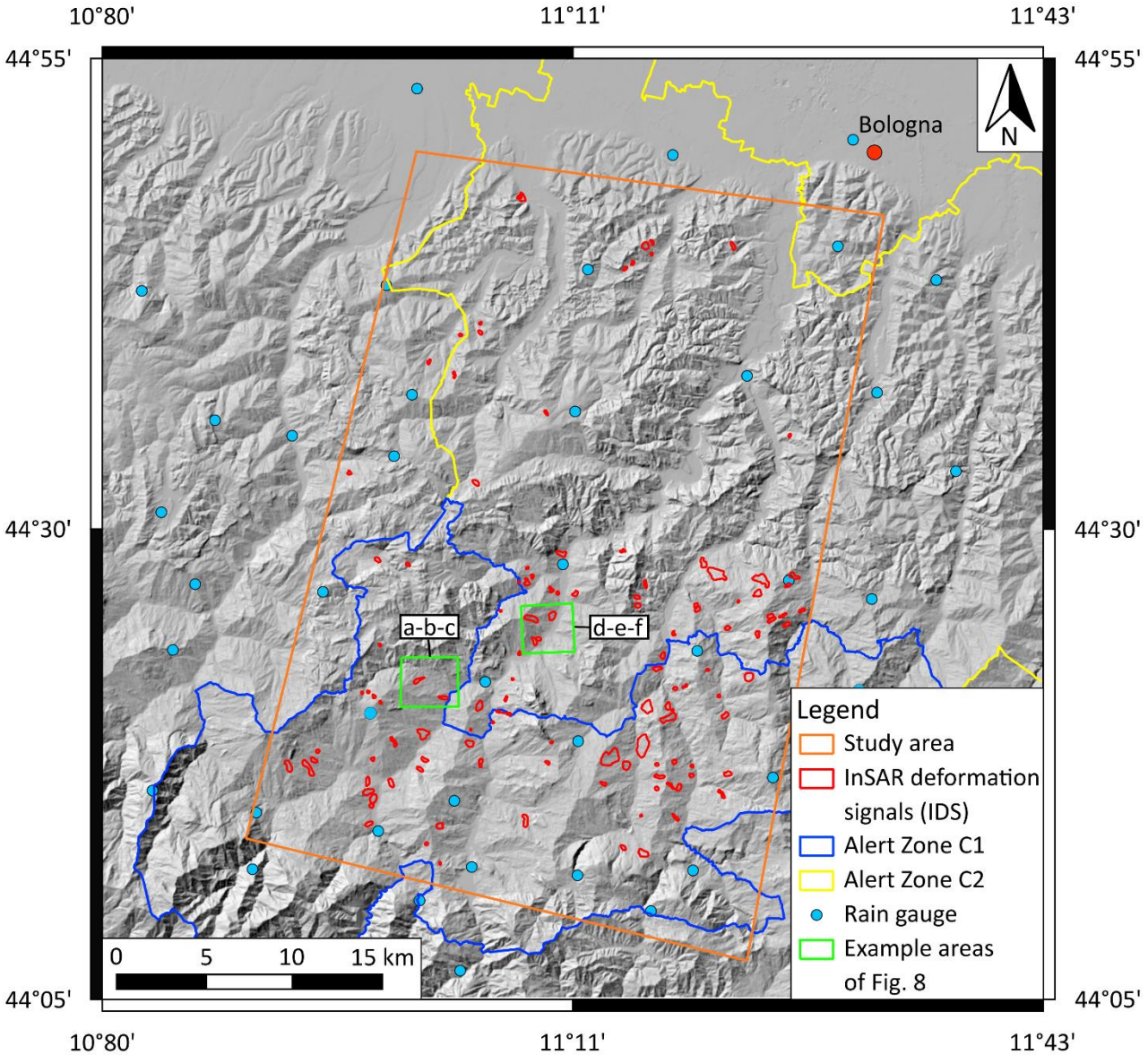

301

302 Figure 5 – Shaded relief map of the study area and spatial distribution of InSAR deformation signals (IDS). The map reports also the
303 two Alert Zones for which aggregate rainfall values were used.

304 Based on these thresholds, we classified solar months depending on the rainfalls occurred. Each month, we
305 check for the exceedance of the rainfall threshold associated to a given landslide probability. The months

306 during which the threshold was exceeded by one or more rainfall events are classified as 'wet'. Otherwise,
307 they are classified as 'dry'. The wet/dry month classification is done separately for the two areas for increasing
308 probabilities of landslide occurrence. We selected this method (see section 3.4) rather than taking into
309 consideration monthly rainfalls or other precipitation parameters because landslide triggering is related to
310 intense rainfall episodes rather than total rainfalls (Squarzoni et al., 2020).

311 ## ***4. Results***

312 ### ***4.1 Regional and multiple temporal scales InSAR analysis***

313 We identified and mapped active landslides by stacking interferograms on different time scales. As explained
314 in section 3.1, regardless of the stack duration, we use only 6 to 24 days interferograms to minimize
315 decorrelation. Therefore, we do not expect to measure displacement rates in different ranges, depending on the
316 stack duration. Rather, we expect to characterize the style of activity of our landslides by distinguishing, for
317 example, sustained slope movements from shorter impulsive deformation that may occasionally involve
318 landslide deposits.

319 In total, through our InSAR analysis, we detected 118 active slope movements in the predominantly hilly and
320 mountainous terrain of the study area (Figure 5). The deformation signals have a plan area ranging from about
321 0.006 to 0.661 $km^2$, with an average of 0.81 $km^2$.

322 Figure 6 shows the LOS velocity distribution for the study area and the 118 mapped IDSs. The velocity values
323 shown are extracted from annual stacks, which represent the data on which most of the recognition and
324 mapping process was carried out. The IDS distributions show notably higher velocities when compared to
325 those pertaining to the whole study area, which appear normal and centered on null values. Also, deformation
326 signals typically show positive skewness confirming their peculiarity and different footprint.

327 Many IDSs (67) are recognized in landslide deposits mapped by the landslide inventory (Trigila et al., 2010).
328 They show that part of the mapped landslide deposit or the whole of it are experiencing measurable surface
329 displacement. We classified the relative position of the IDS and the landslide. Figure 7 shows the frequencies
330 of the five categories that we used.

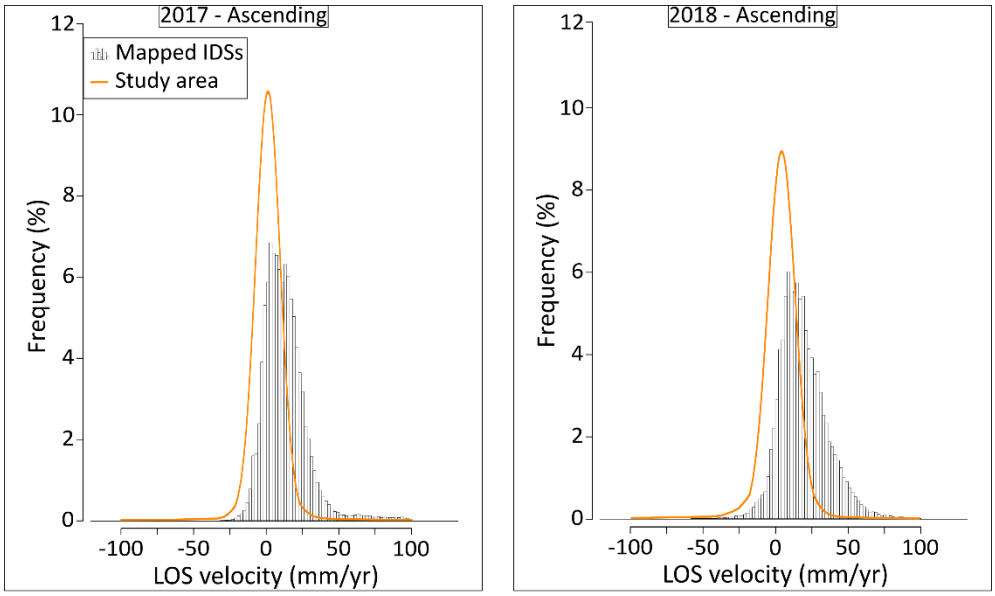


331

332 Figure 6 - Comparison of velocity distribution for the study area and the 118 mapped IDSs. Velocity values are extracted from annual
333 stacks and are for the years 2017 and 2018.

334 The majority of IDSs indicate that only a portion of the landslide (about 90%) is actively deforming. Only in
335 ten cases, we observe surface displacements across the whole mapped deposit. Active movements tend to
336 localize in the medium and upper part of the landslide while, further downslope, the accumulation area is more
337 often dormant. Such result is consistent with the observation that the source area is typically the most active
338 part of the landslide and that most landslide reactivations begin with failures involving the upper/lateral scarp
339 of the landslide and propagate downslope (Bertolini et al., 2004; Simoni et al., 2013).

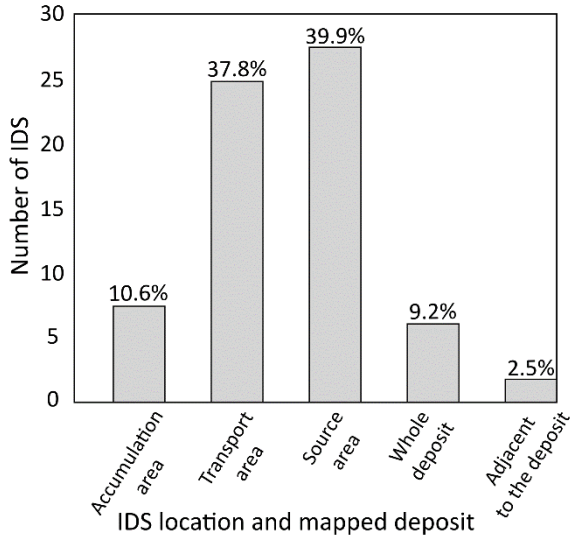


340

341 Figure 7 - Location of slope deformation signals in relation to the landslides mapped by the inventory (R.E.R., 2022).

Figure 8 shows two sample portions of the study area, whose location is reported in Fig. 5, where deformation signals are mapped and appear differently depending on the stack duration: multi-year (a-d), annual (2018) (b-e) and monthly (December 2019) (c-f).

All interferometric stacks show a continuous coverage of the territory with residual noise (i.e., the random blue and red "spots") that is more abundant in monthly stacks and is almost absent in the annual and multi-year stacks. Signals interpreted as the effect of residual noise are preferentially located along steep, vegetated slopes and were observed throughout the entire study area.

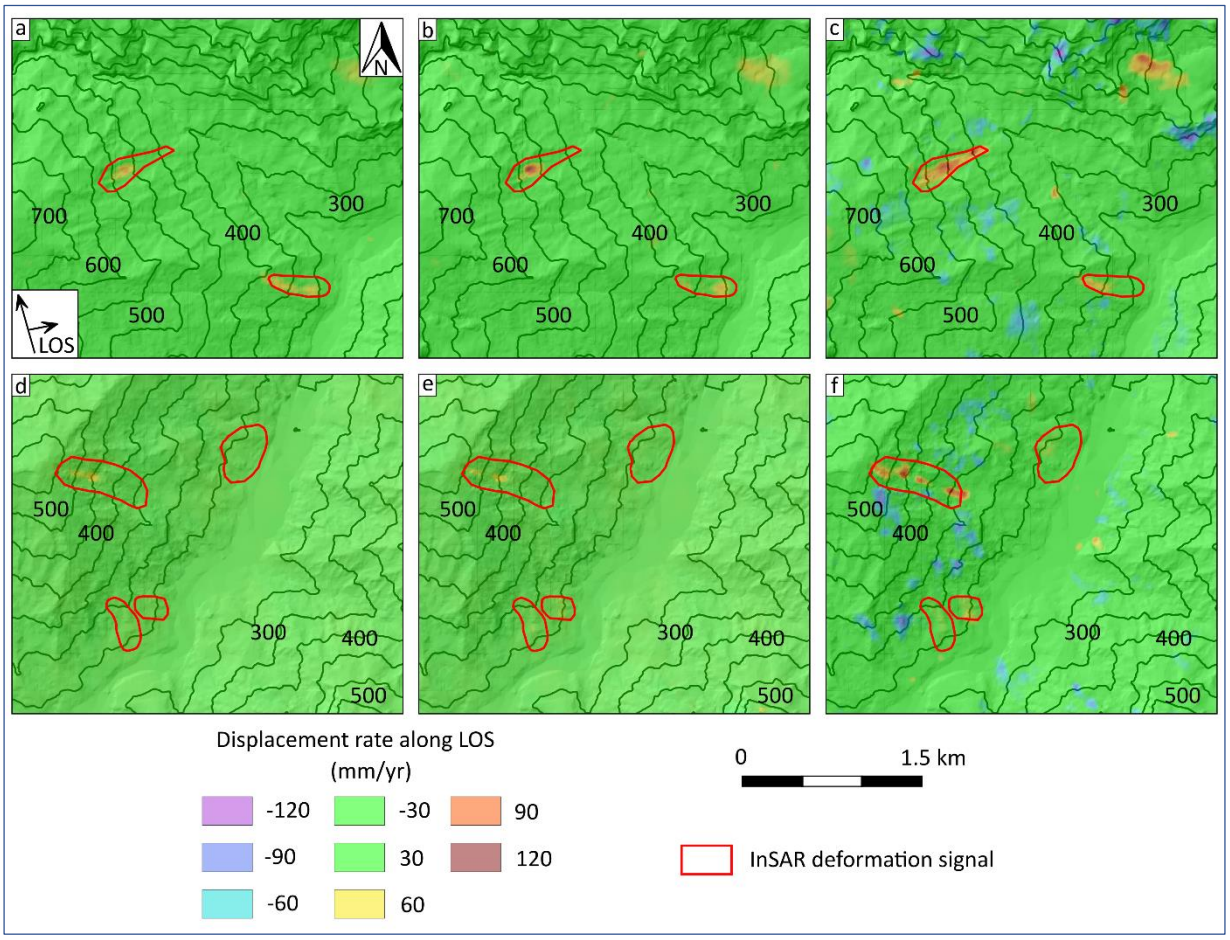


Figure 8. Stacked interferograms of two sample areas and different duration: entire analysis period (a, d), the year 2018 (b-e) and December 2019 (c-f). The location and extent of the sample areas are reported in Figure 6.

Figure 9 illustrates the result showing that about 40% of the IDSs can be detected in interferometric stacks of all durations. Nearly 50% of the IDSs are clearly detectable only in the annual and monthly stacks, while only 10% of the signals are visible only in the monthly stacks. This result clearly indicates that the vast majority of slope deformation signals (i.e., 90%) are clearly detectable in the annual stacks while a smaller fraction (i.e.,

10%) requires the analysis of monthly stacks for detection. Of course, visually inspecting and interpreting monthly stacks is much more time-consuming than annual stacks. Furthermore, monthly stacks contain some decorrelation due to residual noise that may complicate the interpretation and often disappears in annual stacks. On the other end of the spectrum, multi-year stacks do not offer any advantage over annual, based on our results. Annual stacks proved the most suitable for the detection of slope movements and offer the best signal-to-noise ratio, although some occasional and short duration phenomena can be detected only in monthly stacks. These results cannot be generalized because of the diverse types of landslides, rates of movement and style of activity that can be found in other geological context (Cruden and Varnes, 1996).

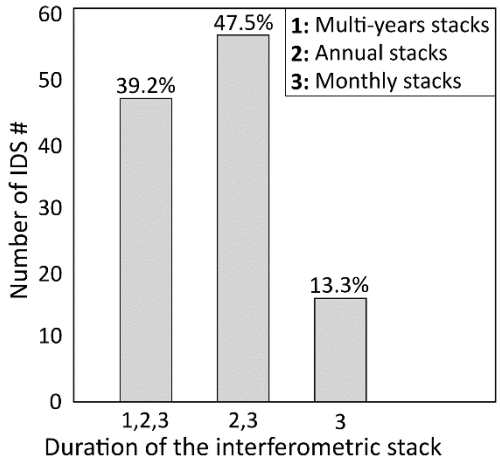


Figure 9 - Frequency of detected IDSs in stacked interferograms of different duration.

## ***4.2 Spatial distribution of InSAR deformation signals***

By comparing the distribution of IDSs over the territory with six control elements (Table 1), we obtain an objective measure of their mutual spatial correlation. The values of the Contrast index, which is a measure of such correlation, are shown in Figure 10 together with associated uncertainties (see Section 3.2). Results are consistent with the geological and geomorphological characteristics and strongly indicate that the distribution of IDS within the study area is not random.

Slope aspect (Figure 10a) has a positive correlation for predominantly East and Southeast-facing slopes, while it is negative for slopes facing North, South and Southwest. For the remaining orientations, the value of the index is too low to give any meaningful indication. Overall, the correlation with the slope aspect appears to be conditioned by the orientation of the satellite's line of sight (LOS), which is oriented E-NE in the ascending

orbit and W-NW in the descending orbit. In fact, North and South-facing slopes, whose movements are hardly visible in both orbits because approximately orthogonal to the LOS, show strong negative correlation. However, when interpreting the results, it must be considered that slopes have preferential orientation towards E and W in the study area (Figure 5).

Spatial correlation with slope gradients (Figure 10b) indicates that signals are most abundant along moderately steep slopes (7.5° to 17.5°), while the negative correlation becomes progressively stronger for higher gradients. The result is a logical consequence of weak fine-grained rocks producing gentle relief and being the most susceptible to landslides, in the Emilia Romagna region (Bertolini et al., 2002). They include pelitic flysch, clay shales and argillites. Our analysis, demonstrate that the bedrock lithology has a strong influence also on the distribution of active slope movements identified by IDSs. In fact, all the landslide-susceptible lithologies (classes 2, 7, 8 and 9) are associate to significant positive values of the Contrast index while all the remaining lithologies have negative correlation with active slope deformations (Figure 10d).

Comparing IDS with quaternary slope deposits, we found that mapped landslide deposits, both active and quiescent, show a significant positive correlation (Figure 10c). On the contrary, the correlation of generic slope deposits (i.e., genesis uncertain/not recognizable) is not significant. The 35 IDS located along slopes where no deposit is mapped indicate either pre-failure deformation of incipient landslides or undetected active landslides. This information has an obvious relevance for land-use planning and civil protection purposes.

The time interval since the last episode of recorded landslide reactivation can be determined thanks to the landslide archive of the Emilia-Romagna region (R.E.R., 2022). Such information is crucial to make any reasoning about event frequency and understand the cyclic behavior of landslides. The degree of spatial correlation of IDSs and recent landslides (Figure 10e), shows significant positive C values, up to 60 years. It should be noted, however, that the completeness of the archive decreases for older episodes and that there is no information regarding about 2/3 of our signals.

Finally, comparing IDS with land use (Figure 10f), significant positive correlations (C>>0) is found for classes 3 and 7, defined by arable land and wooded areas, respectively. The result is important in that indicates that our standard InSAR analysis is capable of a territorial coverage good enough to investigate vegetated areas, at least in our study area, where slopes are gentle. Significant negative correlations are found for classes 2

(artificial green areas and parks), class 4 (vineyards and orchards) and class 10 (water environment). For the remaining classes, the correlation is non-significant.

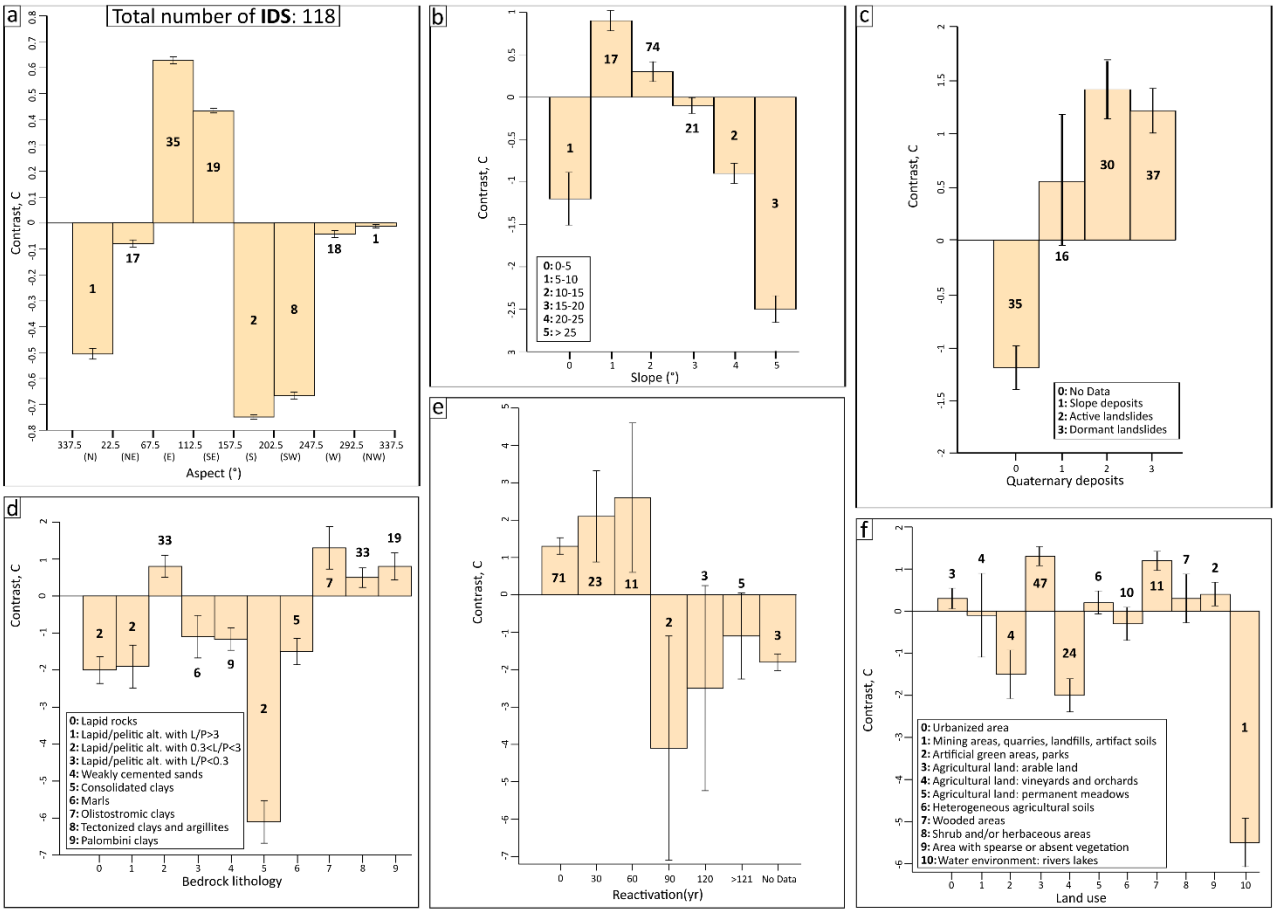


Figure 10 – Contrast index (C) values obtained for the control elements (Table 1). Positive values indicate the existence of a spatial correlation between the specific class of the control element and IDSs. Error bars describe the uncertainty associated to the correlation measure, numbers in the histograms indicate the number of IDS belonging to each class.

## ***4.3 Comparison of IDS state of activity and rainfall forcing***

The intensity of the interferometric signal describes the state of activity of the slope movement and shows either no deformations (Figure 11a, g) or ground displacement with variable degrees of activity (Figures 11b, c, d, e, f, h).

The results of the comparison between our InSAR results and rainfall forcing can be visually inspected in Figures 12 and 13. The graphs illustrate the behavior of IDS through time, for the two areas C1 and C2, in comparison with the distribution of wet/dry months which, in this case, are classified based on the rainfall threshold associated to a landslide probability of 60% (see Section 3.4). The two figures show how many IDSs

417 are in active state during a given month and allow to appreciate the evolution of all 118 slope deformation
418 signals through time as revealed by monthly stacked interferograms. Although appreciable, the relationship
419 between the exceedance of the rainfall threshold (blue bands) and the deformation signal
420 reactivation/acceleration is far from mechanistic. For example, May 2017 is classified as a dry month but many
421 active IDS (65/118) are identified in both C1 and C2 areas. The opposite is found in November of the same
422 year when few active IDS (6/118) are observed despite the wet month classification. Different factors may
423 explain these findings. First, one should consider that landslide rainfall thresholds describe the probability of
424 having at least one landslide over a large mountain territory (about 2600 $km^2$ on average) where thousands of
425 landslide deposits are recognized along the slopes. The presence of many inactive landslides during a rainy
426 month can therefore be seen as perfectly normal. Second, our monthly temporal resolution could cause the loss
427 of some rainfall-acceleration matches (i.e., a rainfall event occurring late in the month may lead to an
428 acceleration that is revealed only in next-month interferograms). Once a landslide is accelerated due to
429 abundant rainfalls, its motion can persist for some time before it gets back to inactive (Leroueil et al., 1996)
430 and this may explain many active signals in dry months. Third, our InSAR analysis may miss failure episodes
431 associated to displacement rates too high to be measured (i.e., > 120 mm/yr approx.) or occurring during spring
432 months when the rapid growth of the vegetation typically causes decorrelation.

433 In order to explore the correlation of our slope deformation signals with rainfall, we analyze the scenarios
434 generated by using a range of landslide probabilities. In general, higher landslide probabilities are associated
435 to higher rainfall thresholds in the duration-intensity space which operate the selection of more 'extreme'
436 rainfall events. The binary classification tools are used to measure objectively the results of the comparison
437 (Figure 14a). Each wet month, active deformation signals are counted as 'true positive' cases (tp) and inactive
438 signals as 'false positive' (fp). Each dry month, active deformation signals are counted as 'false negative' (fn)
439 and inactive ones as 'true negative' cases (tn). Here, we are not evaluating the goodness of the forecasting
440 model (i.e., rainfall threshold) but rather trying to verify whether more deformation signals activate or
441 accelerate following intense rainfall events. Therefore, we use two common binary statistics indexes which
442 measure the rate of IDSs showing an activity status compatible with the climatic conditions of the
443 corresponding month. The positive predictive value, or precision (ppv) measures the rate of active deformation

signals during wet months. The accuracy (acc) measures the overall rate of 'true positive' and 'true negative' cases.

- ppv: (tp)/(tp+fp) [3]

- acc: (tp+tn)/(tp+tn+fp+fn) [4]

Indexes are calculated for Alert Zone landslide probabilities in the range 10 to 90% and results are reported in Figure 14b. It shows that both ppv and acc increase with the severity of climatic conditions (i.e., higher landslide probability). In other words, the precision index (ppv) describes the percentage of active IDSs during wet months classified based on a given rainfall threshold. By using all the rainfall thresholds associated to the range of landslide probabilities, we describe the variation of incidence of actively deforming slope movements. Similar results are obtained for the accuracy index (acc).

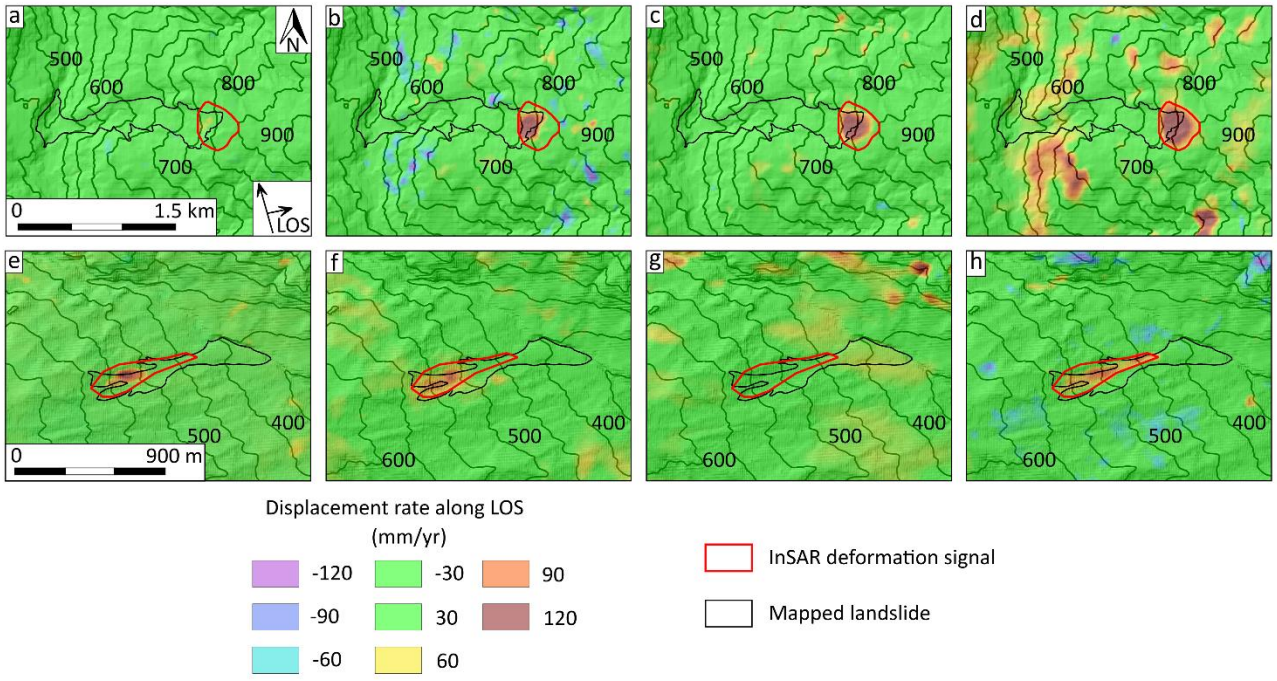


Figure 11. Examples of monthly interferometric stacks for two example deformation signals. The sequence a-d shows the March to June 2017 period and sequence e-h shows April to July 2017 (red and black rectangles in Figure 13, respectively).

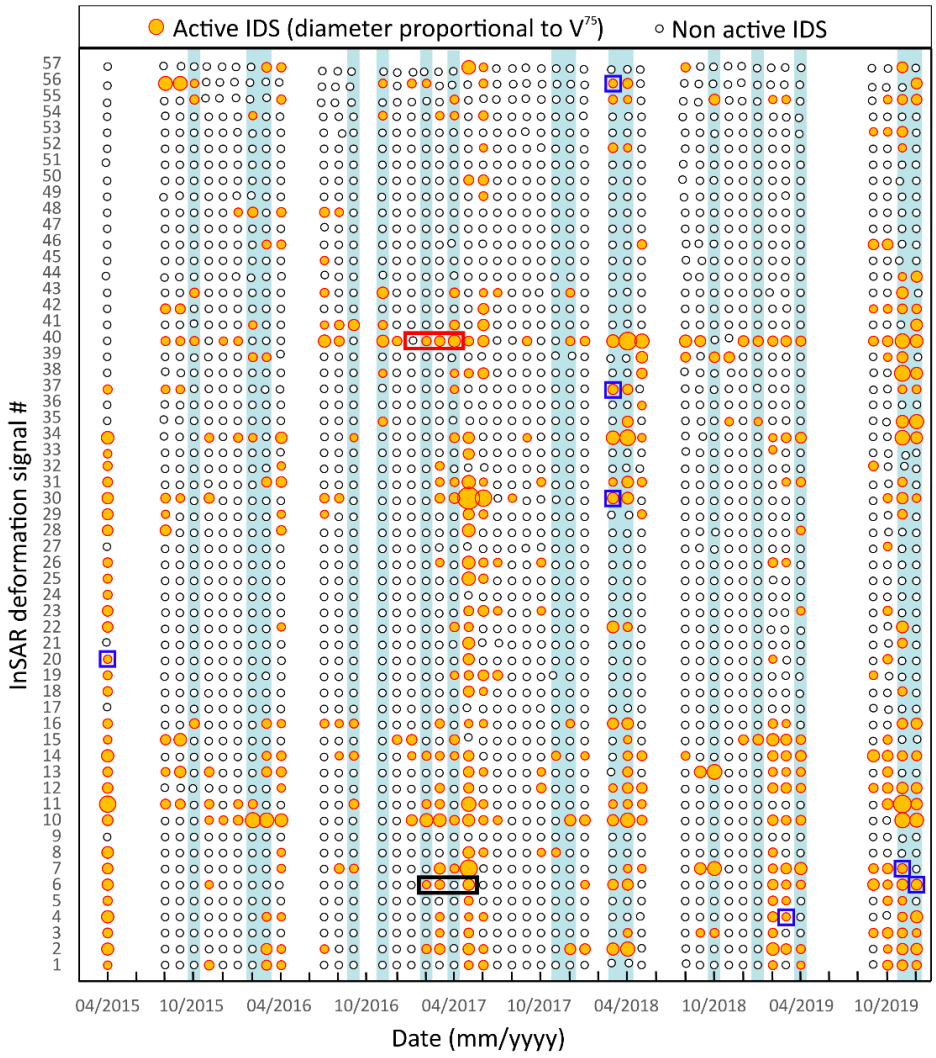


Figure 12 – Summary chart representing the state of activity and displacement rates ($V_{75}$) of all slope deformation signals (IDS) detected over area C1. Blue bands identify 'wet' month during which the rainfall threshold for landslide occurrence (60%) was exceeded. Red and black rectangles identify the stacked interferograms of Figure 11, blue rectangles identify landslide catastrophic reactivations documented in the regional landslide archive (R.E.R., 2022).

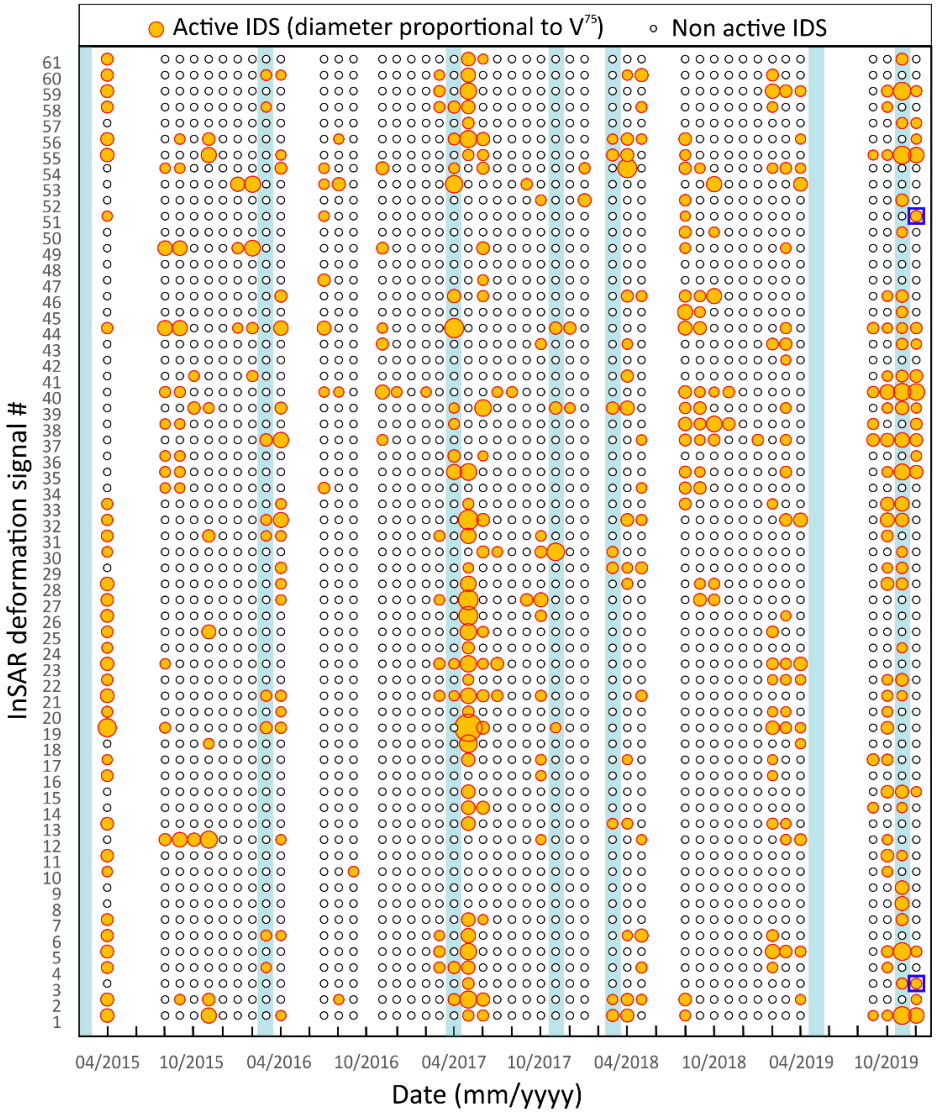


Figure 13 – Summary chart representing the state of activity and displacement rates (V75) of all slope deformation signals (IDS) detected over area C2. Blue bands identify 'wet' month during which the rainfall threshold for landslide occurrence (60%) was exceeded. Blue rectangles identify landslide catastrophic reactivations documented in the regional landslide archive (R.E.R., 2022).

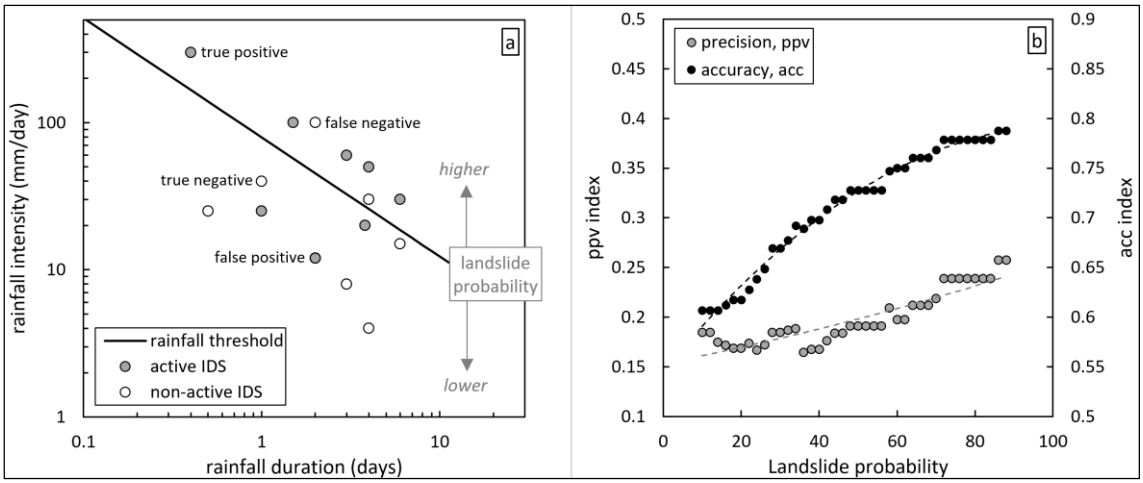


Figure 14. a) Conceptual representation of the binary classification used to compare the state of activity of IDSs to the rainfall conditions described by the exceeding, or not, of the rainfall threshold. b) Rate of active deformation signals during 'wet' months (ppv) and overall rate of IDS activity coherent with rainfall conditions (pnv) for increasing landslide probabilities predicted by rainfall thresholds for the Alert Zone.

## ***Conclusive remarks***

We used standard 2-pass interferometry to investigate slope deformations in a 1200 km$^2$ portion of the Northern Apennines of Italy where landsliding is widespread. Our investigation runs from April 2015 to December 2019 and makes use of short duration (6-24 gg) C-band interferograms to detect active slope movements and monitor their evolution.

Results show that stacking interferograms allows to increase the signal-to-noise ratio and derive quasi-continuous deformation maps (Handwerger et al., 2015; Dini et al., 2019, Ciuffi et al., 2020). In our study area, these results are favored by the gentle morphology where steep slopes (>30°) are relatively rare.

Based on visual inspection and interpretation of stacked interferograms, we detected 118 active slope deformation signals (IDS) that are most likely associated to landslides. The majority of them is better recognized in annual interferometric stacks which show very little residual noise and allow clear detection of slow sustained movements. 13% of our IDS can be detected only in monthly stacks, most likely because their activity is discontinuous in time. Taking longer duration multi-year interferometric stacks into consideration has proved ineffective as it does not allow to identify further phenomena. When compared to the number of landslides mapped by the regional inventory, our active slope deformation signals account for only 1.2%

indicating that a large number of landslide deposits did not experience detectable displacement rates (>30 mm/year approx.) during the study period.

Our inventory of active slope movements may be incomplete because of some deformations could go undetected due to their small extension (< 0.2 $km^2$ approx.), fast pace (>120 mm/yr approx.) or location along steep, unfavorably oriented slopes. On the other hand, the slope movements detected by our interferogram stacking analysis, show remarkable correlation with the geological and geomorphological parameters usually associated to landsliding, indicating that their distribution on the territory is actually linked to the action of slope gravitational phenomena. Most of the IDSs are located along slopes consisting of weak, fine-grained lithologies with slope gradients between 5 and 15°, reflecting the landslide susceptibility of the study area (Simoni et al., 2013). Positive spatial correlation is found with landslide deposits mapped in the regional inventory and, among them, phenomena that experienced catastrophic failures in the last decades have higher chances of being subject to active deformation.

The use of interferometric stacks for the detection and mapping of active deformation signals shows its usefulness as a tool for landslide hazard recognition. It allows to identify the active portions of landslides even in areas where stable reflectors are scarce or absent. By using short duration interferograms, it pushes the upper limit of the measurable displacement rates to over 100 mm/yr, which exceed the rates measurable by multi-temporal InSAR techniques (Raspini et al., 2019). Although the accuracy of our displacement measurements is not comparable to these latter (Cohen-Waeber, 2018), nor to ground-based monitoring, interferogram stacking appears a viable method to detect active slope movements in rural mountain areas where good quality scatterers are scarce or absent.

We pushed our analysis further by analyzing a large number of stacked interferograms pertaining to short monthly intervals and found satisfactory results in capturing the variable degree of activity (i.e., displacement rate) exhibited by our slope deformation signals over time. Not all monthly stacks can be used for this purpose: about 30% of the total are discarded due to decorrelation which is more common in the spring months when the vegetation grows rapidly (Squarzoni et al., 2020) or in the winter months when some snow cover is present (Manconi, 2021). The resulting displacement rate time series were compared to rainfall forcing making use of the rainfall thresholds associated to territorial landslide probabilities (Berti et al., 2012). In general, we observe

514 a good correspondence between rainfalls and IDS activation. Considering increasing landslide probabilities
515 (i.e., heavier rainfalls), the percentage of actively moving landslides increases. During dry months, a relevant
516 fraction (about 15%) of our slow-moving landslides still exhibit appreciable deformation indicating that, its
517 motion can persist for some time.

518 Our work contributes to expand the possible applications of standard InSAR in the broad field of landslide risk
519 management. Standard InSAR acquired significance in such context thanks to the decrease of the revisit times
520 of the satellites (Torres et al., 2012), which determines a substantial decrease of decorrelation. Longer
521 wavelength sensors (Filippazzo and Dinand, 2017) might further contribute in the near future to increase the
522 performance of satellite radar interferometry in rural areas. Interferogram stacking appears as an efficient tool
523 to update existing landslide inventories and/or create inventories of active slope movements. Our analysis
524 indicate that it can also be used as an instrument of territorial surveillance and monitoring over large mountain
525 areas.

526

527 **Acknowledgements and funding**: the research, including the analysis of InSAR results, did not receive any
528 specific grant from funding agencies in the public, commercial, or not-for-profit sectors.

529

## ***References***


Albano, M., Saroli, M., Montuori, A., Bignami, C.,Tolomei, C., Polcari, M., Pezzo, G., Moro, M., Atzori, S., Stramondo, S., Salvi, S., 2018. The Relationship between InSAR Coseismic Deformation and Earthquake-Induced Landslides Associated with the 2017 Mw 3.9 Ischia (Italy) Earthquake. Geosciences 2018, 8, 303. https://doi.org/10.3390/geosciences8080303

Berardino, P.; Fornaro, G.; Lanari, R.; Sansosti, E., 2002 A new algorithm for surface deformation monitoring based on small baseline differential sar interferograms. IEEE Trans. Geosci. Remote Sens. 2002, 40, 2375–2383.

Berti, M., Bertello, L., Bernardi, A.R., Caputo, G., 2017. Back analysis of a large landslide in a flysch rock mass. Landslides https://doi.org/10.1007/s10346-017-0852-5.

Berti, M., Martina, M.L.V., Franceschini, S., Pignone, S., Simoni, A., Pizziolo, M., 2012. Probabilistic rainfall thresholds for landslide occurrence using a Bayesian approach. J. Geophys. Res. Earth Surf. 117, F04006.

Berti, M., Simoni, A. 2012. Observation and analysis of near-surface pore-pressure measurements in clay-shales slopes. Hydrological Processes. 26: 2187-2205. https://doi.org/10.1002/hyp.7981

Bertolini, G., Canuti, P., Casagli, N., De Nardo, M., Egidi, M., Mainetti, M., Pingone, R, Pizziolo, M., 2002. Carta della Pericolosità Relativa da Frana della Regione Emilia-Romagna. SystemCart, Rome, Italy.

Bertolini, G., Casagli, N., Ermini, L., Malaguti, C., 2004. Radiocarbon data on late glacial and holocene landslides in the Northern Apennines. Nat. Hazards 31, 645–662.

Bertolini, G., Pellegrini, M., 2001. The landslides of the Emilia Apennines (northern Italy) with reference to those which resumed activity in the 1994–1999 period and required civil protection interventions. Quad Geol Appl 8, 27–74.

Bianchini, S., Herrera, G.,Mateos, R.M., Notti, D., Garcia, I.,Mora, O.,Moretti, S., 2013. Landslide activity maps generation by means of persistent scatterer interferometry. Remote Sens. 5, 6198–6222. https://doi.org/10.3390/rs5126198.

554 Boccaletti, M., Elter, P., Guazzone, G., 1971. Plate tectonic models for the development of the western alps
555 and Northern Apennines. Nature 234 (49), 108–111.

556 Bogaard, T.A., Greco, R., 2016. Landslide hydrology: from hydrology to pore pressure. Wiley Interdiscip.
557 Rev. Water 3 (3), 439–459.

558 Bonham-Carter, G.F., 1994. Geographic Information Systems for Geoscientists: Modeling with GIS.
559 Pergamon Press, Canada.

560 Borgatti, L., Corsini, A., Barbieri, M., Sartini, G., Truffelli, G., Caputo, G., Puglisi, C., 2006. Large reactivated
561 landslides in weak rock masses; a case study from the Northern Apennines (Italy). Landslides 3 (2), 115–124.

562 Bürgmann, R., Rosen, P.A., Fielding, E.J., 2000. Synthetic aperture radar interferometry to measure Earth's
563 surface topography and its deformation. Annu. Rev. Earth Planet. Sci. 28, 169–209.

564 Cervi, F., Ronchetti, F., Martinelli, G., Bogaard, T.A., Corsini, A., 2012. Origin and assessment of deep
565 groundwater inflow in the Ca' Lita landslide using hydrochemistry and in situ monitoring. Hydrol. Earth Syst.
566 Sci. 16 (11), 4205–4221.

567 Chen, C.W., Zebker, H.A., 2001. Two-dimensional phase unwrapping with use of statistical models for cost
568 functions in nonlinear optimization. JOSA A 18, 338–351.

569 Ciuffi, P., Bayer, B., Berti, M., Franceschini, S., Simoni, A., 2021. Deformation Detection in Cyclic Landslides
570 Prior to Their Reactivation Using Two-Pass Satellite Interferometry. Applied Sciences 11, 3156.
571 https://doi.org/10.3390/app11073156

572 Cohen-Waeber, J., Bürgmann, R., Chaussard, E., Giannico, C., Ferretti A., 2018. Spatiotemporal patterns of
573 precipitation-modulated landslide deformation from independent component analysis of InSAR time series.
574 Geophys. Res. Lett. 45, 4, 1878–1887. doi: 10.1002/2017GL075950

575 Corsini, A., Farina, P., Antonello, G., Barbieri, M., Casagli, N., Coren, F., Guerri, L., Ronchetti, F., Sterzai,
576 P., Tarchi, D., 2006. Space-borne and ground-based SAR interferometry as tools for landslide hazard
577 management in civil protection. Int. J. Remote Sens. 27 (12), 2351–2369.

578 Cruden, D.M., Varnes, D.J., 1996. Landslides: investigation and mitigation. Chapter 3-landslide types and
579 processes. Transportation Research Board Special Report.

580 Dini, B., Manconi, A., Loew, S., 2019. Investigation of slope instabilities in NW Bhutan as derived from
581 systematic DInSAR analyses. Engineering Geology 259, 105111.

582 Dong, J., Zhang, L., Li, M., Yu, Y., Liao, M., Gong, J., Luo, H., 2018. Measuring precursory movements of
583 the recent Xinmo landslide in Mao County, China with Sentinel-1 and ALOS-2 PALSAR-2 datasets.
584 Landslides 15, 135-144. doi:10.1007/s10346-017-0914-8.

585 Fattahi, H., Amelung, F., 2015. InSAR bias and uncertainty due to the systematic and stochastic tropospheric
586 delay. Journal of Geophysical Research: Solid Earth 120, 8758–8773.

587 Ferretti, A.; Fumagalli, A.; Novali, F.; Prati, C.; Rocca, F.; Rucci, A., 2011. A new algorithm for processing
588 interferometric data-stacks: Squeesar. IEEE Trans. Geosci. Remote Sens. 2011, 49, 3460–3470.

589 Ferretti, A.; Prati, C.; Rocca, F., 2001. Permanent scatterers insar interferometry. IEEE Trans. Geosci. Remote
590 Sens. 2001, 39, 8–20.

591 Filippazzo, G., Dinand, S., 2017. The Potential Impact of Small Satellite Radar Constellations On Traditional
592 Space Systems, In Proceedings of the 5th Federated and Fractionated Satellite Systems Workshop, Ithaca, NY,
593 USA, 2–3 November 2017. p. 12.

594 Fruneau, B., Achache, J., Delacourt, C., 1996. Observation and modelling of the saintetienne-de-tinée landslide
595 using SAR interferometry. Tectonophysics 265, 181–190.

596 Handwerger, A.L., Huang, M.-H., Fielding, E.J., Booth, A.M., Bürgmann, R., 2019. A shift from drought to
597 extreme rainfall drives a stable landslide to catastrophic failure. Sci. Rep. 9, 1569.

598 Handwerger, A.L., Roering, J.J., Schmidt, D.A., 2013. Controls on the seasonal deformation of slow-moving
599 landslides. Earth Planet. Sci. Lett. 377, 239–247.

600 Handwerger, A.L., Roering, J.J., Schmidt, D.A., Rempel, A.W., 2015. Kinematics of earthflows in the northern
601 California coast ranges using satellite interferometry. Geomorphology 246, 321–333.

Hooper, A. A multi-temporal InSAR method incorporating both persistent scatterer and small baseline approaches. Geophys. Res. Lett. 2008, 35, L16302.

Hooper, A., Segall, P., Zebker, H., 2007. Persistent scatterer interferometric synthetic aperture radar for crustal deformation analysis, with application to volcán alcedo, galápagos. Journal of Geophysical Research: Solid Earth 112.

Hooper, A., Zebker, H., Segall, P., Kampes, B., 2004. A new method for measuring deformation on volcanoes and other natural terrains using InSAR persistent scatterers. Geophys. Res. Lett. 31.

Iverson, R.M., Major, M.M., 1987. Rainfall, groundwater-flow, and seasonal movement at minor creek landslide, north-western California - physical interpretation of empirical relations. Geol. Soc. Am. Bull. 99 (4), 579–594.

Krzeminska, D.M., Bogaard, T.A., van Asch, T.W.J., van Beek, L.P.H., 2012. A conceptual model of the hydrological influence of fissures on landslide activity. Hydrol. Earth Syst. Sci. 16 (6), 1561–1576.

Leroueil, S., Locat, J., Vaunat, J., Picarelli, L., Lee, H., Faure, R., 1996. Geotechnical characterization of slope movements. In: Senneset K (ed), Landslides, Proceedings 7th International Symposium Landslides, Trondheim, Norway, 17–21 June, 1, 53-74. Balkema, Rotterdam, The Netherlands.

Liu, J.G., Mason P.J., 2017. Image processing and GIS for remote sensing. Wiley Blackwell, Oxford, UK, 457 pp. ISBN: 9781118724200

Manconi, A., 2021. How phase aliasing limits systematic space-borne DInSAR monitoring and failure forecast of alpine landslides. Engineering Geology 287 (2021) 106094, 1-7.

Massonnet, D., Feigl, K.L., 1998. Radar interferometry and its application to changes in the Earth's surface. Rev. Geophys. 36, 441–500.

Meyer, N.K., Schwanghart, W., Korup, O., Romstad, B., Etzelmüller B., 2014. Estimating the topographic predictability of debris flows, Geomorphology 207, 114-125. https://doi.org/10.1016/j.geomorph.2013.10.030

Panini, F., Bettelli, G., Bonazzi, U., Gasperi, G., Fioroni, F., Fregni, P., 2002. Note illustrative alla Carta Geologica d'Italia a scala 1:50.000. Foglio N. 237, Sasso Marconi.

627 Pavan, V., Tomozeiu, R., Cacciamani, C., Di Lorenzo, M., 2008. Daily precipitation observations over Emilia-
628 Romagna: mean values and extremes. Int. J. Climatol. 28 (15), 2065–2079.

629 Petley, D.N., Mantovani, F., Bulmer, M.H., Zannoni, A., 2005. The use of surface monitoring data for the
630 interpretation of landslide movement patterns. Geomorphology 66, 133–147.

631 Picotti, V., Pazzaglia, F.J., 2008. A new active tectonic model for the construction of the Northern Apennines
632 mountain front near Bologna (Italy). J. Geophys. Res. Solid Earth 113 (B8), B08412.

633 Pini, G.A., 1999. Tectonosomes and olistostromes in the argille scagliose of the Northern Apennines, Italy.
634 Spec. Pap. Geol. Soc. Am. 335 (1), 1–70.

635 Raspini, F., Bianchini, S., Ciampalini, A., Del Soldato, M., Montalti, R., Solari, L., Tofani, V., Casagli, N.,
636 2019. Persistent scatterers continuous streaming for landslide monitoring and mapping: the case of the Tuscany
637 region (Italy). Landslides 16, 2033–2044. https://doi.org/10.1007/s10346-019-01249-w.

638 R.E.R., Servizio Geologico, Sismico e dei Suoli, 2022 (regularly updated). Landslide Inventory Map 1:10000
639 scale of the Emilia-Romagna Region, Italy. https://geo.regione.emilia-romagna.it/cartografia_sgss/

640 Regmi, N.R., Giardino, J.R., Vitek J.D., 2010. Modeling susceptibility to landslides using the weight of
641 evidence approach: Western Colorado, USA. Geomorphology 115, 1–2, 172-187.
642 https://doi.org/10.1016/j.geomorph.2009.10.002.

643 Ricci Lucchi, F., 1986. The Oligocene to recent foreland basins of the Northern Apennines. In: A., P.,
644 Homewood, P. (Eds.), Special Publication of the International Association of Sedimentologists. vol. 8.
645 Blackwell, Oxford, pp. 105–139.

646 Ronchetti, F., Borgatti, L., Cervi, F., Lucente, C.C., Veneziano, M., Corsini, A., 2007. The Valoria landslide
647 reactivation in 2005–2006 (Northern Apennines, Italy). Landslides 4 (2), 189–195.

648 Rosen, P.A., Hensley, S., Joughin, I.R., Li, F.K., Madsen, S.N., Rodriguez, E., Goldstein, R.M., 2000.
649 Synthetic aperture radar interferometry. Proc. IEEE 88, 333–382.

650 Sandwell, D., Mellors, R., Tong, X., Wei, M., Wessel, P., 2011. Open radar interferometry software for
651 mapping surface deformation. Eos, Transactions American Geophysical Union 92, 234.

652 Schmidt, D.A., Bürgmann, R., 2003. Time-dependent land uplift and subsidence in the Santa Clara Valley,
653 California, from a large interferometric synthetic aperture radar data set. Journal of Geophysical Research:
654 Solid Earth 108.

655 Simoni, A., Ponza, A., Picotti, V., Berti, M., Dinelli, E., 2013. Earthflow sediment production and holocene
656 sediment record in a large Apennine catchment. Geomorphology 188 (1), 42–53.

657 Spiegelhalter, D.J., 1986. A statistical view of uncertainty in expert systems. In: Gale, W. (Ed.), Artificial
658 Intelligence and Statistics. Addison-Wesley, Reading, MA, 17–55.

659 Squarzoni, G.; Benedikt, B.; Franceschini, S.; Simoni, 2020. A. Pre- and post-failure dynamics of landslides
660 in the Northern Apennines revealed by space-borne synthetic aperture radar interferometry (InSAR).
661 Geomorphology 369, 107353.

662 Stumpf, A., Malet, J.P., Kerle, N., Niethammer, U., Rothmund, S., 2013. Image-based mapping of surface
663 fissures for the investigation of landslide dynamics. Geomorphology 186, 12–27.

664 Tarayre, H., Massonnet, D., 1996. Atmospheric propagation heterogeneities revealed by ERS-1 interferometry.
665 Geophys. Res. Lett. 23, 989–992.

666 Tomozeiu, R., Busuioc, A., Marletto, V., Zinoni, F., Cacciamani, C., 2000. Detection of changes in the summer
667 precipitation time series of the region Emilia-Romagna, Italy. Theor. Appl. Climatol. 67 (3–4), 193–200.

668 Tong, X., Schmidt, D., 2016. Active movement of the Cascade landslide complex in Washington from a
669 coherence-based InSAR time series method. Remote Sensing of Environment 186, 405–415.

670 Torres, R., Snoeij, P., Geudtner, D., Bibby, D., Davidson, M., Attema, E., Potin, P., Rommen, B., Floury, N.,
671 Brown, M., Traver, I.N., Deghaye, P., Duesmann, B., Rosich, B., Miranda, N., Bruno, C., L'Abbate, M., Croci,
672 R., Pietropaolo, A., Huchler, M., Rostan, F., 2012. GMES Sentinel-1 mission. Remote Sens. Environ. 120, 9–
673 24. https://doi.org/10.1016/j.rse.2011.05.028.

674 Trigila, A., Iadanza, C., Spizzichino, D., 2010. Quality assessment of the Italian Landslide Inventory using
675 GIS processing. Landslides 7, 455–470. https://doi.org/10.1007/s10346-010-0213-0.

Vannucchi, P., Maltman, A., Bettelli, G., Clennell, B., 2003. On the nature of scaly fabric and scaly clay. J. Struct. Geol. 25 (5), 673–688.

Xiao, R., Yu, C., Li, Z., Jiang, M., He, X., 2022. InSAR stacking with atmospheric correction for rapid geohazard detection: Applications to ground subsidence and landslides in China. Int. J. of Applied Earth Observations and Geoinformation 115, 103082.

Zebker, H.A., Rosen, P.A., Hensley, S., 1997. Atmospheric effects in interferometric synthetic aperture radar surface deformation and topographic maps. Journal of Geophysical Research: Solid Earth 102, 7547–7563.

Zebker, H.A., Villasenor, J., 1992. Decorrelation in interferometric radar echoes. IEEE Trans. Geosci. Remote Sens. 30, 950–959.

Zhang, Y., Meng, X.M., Dijkstrac, T.A., Jordan, C.G., Chen, G., Zeng, R.Q., Novellino, A., 2020. Forecasting the magnitude of potential landslides based on InSAR techniques. Remote Sensing of Environment 241, 111738.

# 6. Discussion and General conclusions

The general results of the thesis can be grouped in two main categories, one of which deals with technical issues related to the application of radar interferometry for the detection and monitoring of landslides. The second category includes geological and geomorphological issues that were investigated by the different InSAR datasets and that enhance our knowledge of landslide dynamics.

My research aimed to test the potential of different InSAR results, in terms of single interferograms and interferometric stacks of different time scales (monthly, yearly, multi-year), for the recognition and mapping of deformation signals (IDS), as well as for the extraction of displacement time series.

From a technical point of view and as demonstrated within the document, it can be stated that the areal-scale InSAR analysis can successfully identify the boundaries of active deformation processes during the study period, while the site-specific analysis improves the results in terms of spatial pattern and absolute velocity value.

From a theoretical point of view, the technique is able to measure displacements of up to 2.8 cm/6 days along the LOS, when using Sentnel-1 images. This value represents a complete cycle between -π and +π and corresponds to half of the Sentinel-1 satellites' acquisition wavelength value (5.6 cm). However, in the works presented in this document, we were able to derive velocities up to 2.1 cm/6 days and, this value, represents our upper limit of investigable velocity. We have defined a lower limit value of 30 mm/year, below which we are unable to discriminate an active process, while deformations above 2.1 cm/6 days cause phase jumps of more than one cycle, generating decorrelation that we are unable to solve (fast-displacement decorrelation).

The highest velocities along the LOS that have been detected correspond to 2.1 cm/6 days, while the lowest velocities correspond to 30 mm/yr. For the detection of deformation processes with displacement rates below 30 mm/yr, it is possible to increase the temporal baseline, but this would cause an increase in decorrelation, or it would be necessary to apply multi-temporal InSAR techniques (Ferretti et al., 2001). For processes with high displacement rates, however, InSAR techniques are not a valid tool.

With the work described in Chapter 3, it is possible to appreciate how, by setting the InSAR reference area close to the deforming region, the accuracy of the deformation signals improved. This is probably due to the similar atmospheric conditions of the stable reference area and the moving landslide. In this work (Chapter 3), InSAR analysis was applied to three processes that suffered catastrophic failure, with the aim to investigate the deformations prior to failure. We successfully derived information on the deformation patterns in the periods prior to the catastrophic failures with maximum measured velocities along the LOS of 160 mm/month. In addition, stable reflectors within the study area (especially on slopes affected by active deformation) are absent or very scarce, and standard 2-pass InSAR is the only way to identify active processes and detect movement before failure.

The analysis was successfully conducted on several study areas and allowed us to detect signals related to active deformation processes. Interferometric stacks with longer durations, such as multi-year and annual, which are obtained by overlapping interferograms with lengths varying between 6 and 60 days, are the ones that allow the detection of the greatest number of IDSs. In fact, as discussed in Chapter 5, the IDSs detectable only in the monthly stacks, constructed with interferograms with a maximum temporal baseline of 30 days, are few (13%), while a significant fraction (87%) appears more clearly in the annuals.

Useful information on active processes is recorded in the annual stacks, even for IDSs that move very slowly and are invisible in the monthly stacks. Multi-year interferometric stacks can hide processes that are not characterised by temporal continuity, while monthly stacks, on the other hand, present a lot of noise and their inspection requires more time, which, for our study goals, does not justify their use. They can be

particularly useful in the case of landslide phenomena that have a less continuous style of activity over time and are characterised by rapid accelerations of relatively short duration.

Within the study areas, mainly defined by agricultural land, wooded areas, shrub and herbaceous areas, the results presented show that it is possible to obtain quasi-continuous deformation maps of the ground, even in cases where the LOS show relatively high displacement rates. A key role is played by the quality of the raw data, characterised by small spatial and temporal baseline values (6 days for Sentinel-1), which allowed us to perform stacking processing. Our results demonstrate that the interferometric stack is the most suitable tool for landslide detection and mapping.

The operator's expert interpretation is crucial and geological and geomorphological knowledge of the study area is required when inspecting the InSAR data. For the validation of an IDS, as many evaluation criteria as possible must be satisfied, e.g. the deformation signal shows a clear velocity inversion when using data sets acquired with different flight geometries (ascending and descending), it is recognisable within different datasets acquired with the same flight geometry, the deformation is present within different monthly stacks or it is clearly recognisable within annual or multi-year stacks, and finally, it is necessary that the deformation signal has geological and geomorphological significance. For example, if a signal crosses a ridge or valley, it is much more possible that it is due to an artefact in the InSAR data, rather than a deformation process. This inspection and interpretation step is absolutely essential to discriminate the interferometric signal associated with active deformation processes from those associated with artefacts and errors in the InSAR data.

The paper presented different methodologies and different data used for the extraction of the displacement time series derived from InSAR. The results show that traditional two-pass interferometry can provide useful information for investigating the temporal evolution of active deformation processes. Depending on the goals of the work, we can choose between different categories of InSAR results. The extraction of displacement time series from monthly interferometric stacks provides datasets with one value per month. This dataset can be useful when we want to make comparisons with data with a similar temporal resolution, or when we want to study the behaviour of active processes on a monthly and seasonal scale. The construction of displacement time series by using 6-day interferograms, on the other hand, allows for denser density displacement series. They are useful when we want to investigate the behaviour of a landslide, for example, linked to a single rainfall event, or when, as shown in Chapter 4, we want to analyse relationships with climatic parameters characterised by high temporal resolution.

From a technical point of view, using single 6-day interferograms is more laborious. A greater amount of time may be required for data validation and interpretation, which is why this approach has been adopted for only a few IDSs in this paper. The extraction of displacement time series from monthly interferometric stacks is a simpler process and probably more suitable for the analysis of a large number of deformation processes. From a practical point of view, after validation of the interferometric stacks, it is possible to extract time series for all IDSs of interest.

The possibility of being able to compare displacement time series and deformation maps derived from InSAR (represented by single interferograms, or interferometric stacks) defines interesting opportunities. This, as shown, allows the definition of activity thresholds for the studied landslides. Deriving binary “active/inactive” information on the analysed processes allows the construction of useful datasets that find applications in risk mitigation and warning system validation contexts. However, the expert analysis of the operator during the threshold definition, is a crucial step in the work.

Regarding the comparison of displacement time series derived from 6-day interferometry, climate parameters and geographic alert thresholds, described in the work in Chapter 4, the results showed that traditional two-pass interferometry can provide useful information for the validation of geographic alert systems. As mentioned, the promising results of the work indicate that by increasing the duration of the analysis period, by using the proposed approach, it is possible to detect and monitor the evolution of active

gravitational slope movements over the regional territory. Moreover, thanks to the short revisit time of the Sentinel-1 satellites, it is possible to think about the implementation of near real-time warning systems in which climate parameters are compared weekly with the results of the 6-day interferogram analysis.

From a geological point of view, IDSs are commonly placed on landslide deposits and, when they are outside, they are placed on slopes that appear potentially unstable based on simple morphological observation. These signs could correspond to deformation processes not recognised by the inventory or neo-activation landslides. A difference between the results described in the work in Chapter 4 and Chapter 5 is the percentage of IDSs located on slopes without mapped landslides. For the work carried out on the Umbria region (chapter 4), this percentage is much higher (35%), compared to the analysis carried out for the work described in chapter 5, which concerns a large basin in the Emilia-Romagna region (only 3%). This difference, rather than from a different efficiency of the mapping operation, from a geological and geomorphological point of view, can be explained by the way that the landslides characterising the area analysed in Emilia-Romagna present more visible geomorphological evidence. Landslides are often represented by large earth flows, characterised by typical morphologies and more marked boundaries, as well as larger extensions, unlike the landslides found in the Umbria region. The latter, in fact, are often represented by translational landslides of smaller extension and, therefore, present less visible evidence if they do not involve infrastructures or human buildings.

The deposits on which the IDS are located have similar features. They are defined by low slope gradients resulting from the weak mechanical characteristics of the lithologies typically involved (e.g. fine-grained sedimentary rocks). Slopes with these characteristics often host slow-moving landslides, which are the categories of landslides that can be studied with InSAR.

A further result of geological interest derived from the analysis and discussed in Chapter 5, is the information describing the processes activated in the last 30 years as the most active and detectable by the InSAR analysis. As mentioned, this result can be explained by the idea that recently activated processes have not yet reached their equilibrium condition and are more prone to show catastrophic activations and/or small deformations over time. From the perspective of risk assessment, this information can be particularly useful, as it identifies phenomena that are more prone to deformation. This information also underlines the importance of having a deformation inventory that is as reliable and accurate as possible.

A reassuring result of the work described in this paper is the percentage of active landslides in relation to mapped landslides. Although the time intervals analysed span, in all cases, dry periods and periods characterised by precipitation events, this value is always very low. For the study area related to the work in chapter 3, only 4 landslides out of 182 (2.2%) were active during the study period (4 years); about 2% in the Umbria region (chapter 4) and only 1.2% in the wide basin of Emilia-Romagna (chapter 5). It is possible that, due to the limitations of the technique, particularly fast phenomena (such as rock falls or debris flows) were not detected, although they did occur. The same may be true for extremely slow processes, such that they cannot be measured with InSAR.

Anyway, it is possible to state that the slopes characterised by slow and continuous deformation, or which suffer catastrophic failure, are few in number compared to the landslides mapped. This may be related to a different climatic regime that characterised the time intervals studied, to the stabilisation of many previously unstable slopes, or to the extremely low displacement velocity that can characterise processes such as the great earth flows of the Northern Apennines.

InSAR-derived displacement time series allow the analysis of relationships between ground deformations and climate forcings.

In a case study (Chapter 3) we observed a decrease in velocity is observed in late summer, although the general trend cannot be described as seasonal, but rather dependent on the rainfall regime. Repeated

accelerations are generally observed during the wettest periods with a delayed peak compared to the 30-day cumulative rainfall, although the reactivation in late 2019 occurred at the peak of a rainy period without any appreciable delay. As mentioned, our analysis shows that major precipitation events on a weekly or monthly scale are the main drivers of accelerations and reactivations in the study area. Rather than seasonal variation, in this work we observed a general tendency for the lowest annual velocities to occur during the late summer.

By comparing the displacement time series extracted from the monthly stacks with the landslide activation probability thresholds (Chapter 5), also based on climatic parameters, we show that there is generally a good correspondence between the rainfall event and the activation of IDSs. The percentage of active IDSs in rainy months increases as the probability of activation increases, while the percentage of active landslides in dry months is moderate and remains fairly constant as the probability thresholds change.

In conclusion, it can be said that InSAR is a useful technique that has contributed to integrating our knowledge of slow landslides in the Northern Apennines and beyond. However, care must be taken during InSAR processing and interpretation of the results. In particular, when setting the different parameters for unwrapping and selecting the interferograms, in order to obtain reliable data sets.

Traditional two-pass interferometry is useful for studying landslide dynamics. From a spatial point of view, it provided good land coverage and proved capable of detecting active slope movements from a few centimetres to a few tens of centimetres per year.

The results obtained by the Sentinel-1 satellites, which has been acquiring images at a temporal frequency of less than 12 days (6 days if both satellites are in operation) since the end of 2014, have been promising and suggest that InSAR will increasingly become a powerful tool for landslide monitoring.

*6.1 References*

Ferretti, A., Prati, C., Rocca, F., 2001. Permanent scatterers in SAR interferometry. IEEE Trans. Geosci. Remote Sens. 39, 8–20.

## ACKNOWLEDGEMENTS

At the end of this work, I want to take the opportunity to thank the people who made it all possible.

First of all, I want to thank my supervisor Alessandro Simoni who allowed me to enter the world of scientific research. He triggered his passion and dedication to this work in me. I want to thank all my friends at Fragile, especially Benedikt Bayer and Silvia Franceschini for their constant and indispensable support. They have enriched me professionally, but also from a human point of view.

I would like to say thank you to the entire Applied Geology group and Prof. Matteo Berti, for the valuable exchanges and constructive conversations.

I would also like to thank Francesco Ponziani, for sharing with me the opportunity to do some very interesting work.

I thank Andrea Manconi and all the staff of the Alpine Remote Sensing research group at the SLF institute in Davos, for their hospitality and helpful discussions.

I thank all the students and researchers I have met over these three years, each of you has left something useful and interesting in me.

I thank all my friends for supporting and encouraging me in this troubled journey.

I thank my family, present and not, for always being on my side and giving me the push at every moment when I needed it.

I thank my girlfriend, Caterina, for listening to my many complaints, for giving me the push at every difficult moment, and for celebrating the happy moments with me.

Finally, I thank Geology, which allowed me to turn a passion into a job.